FUNDAMENTAL UNDERSTANDING OF NO_X SEQUESTRATION CAPACITY AND PATHWAYS IN NANO-TIO_2 ENGINEERED CEMENTITIOUS MATERIALS

A Dissertation
Presented to
The Academic Faculty

by

Qingxu Jin

In Partial Fulfillment
of the Requirements for the Degree
Doctor of Philosophy in the
School of Civil and Environmental Engineering

Georgia Institute of Technology
December 2019

COPYRIGHT © 2019 BY QINGXU JIN

FUNDAMENTAL UNDERSTANDING OF NO_X SEQUESTRATION CAPACITY AND PATHWAYS IN NANO-TIO_2 ENGINEERED CEMENTITIOUS MATERIALS

Approved by:

Dr. Kimberly E. Kurtis, Advisor
School of Civil and Environmental Engineering
Georgia Institute of Technology

Dr. Emily Grubert
School of Civil and Environmental Engineering
Georgia Institute of Technology

Dr. Lawrence F. Kahn
School of Civil and Environmental Engineering
Georgia Institute of Technology

Dr. Jeffrey W. Bullard
Zachry Department of Civil and Environmental Engineering
Texas A&M University

Dr. Yuanzhi Tang
School of Earth and Atmospheric Sciences
Georgia Institute of Technology

Date Approved: November 1st, 2019

ACKNOWLEDGEMENTS

I would like to express my utmost gratitude to my advisor Dr. Kimberly Kurtis for her insightful and priceless guidance and tutelage throughout my Ph.D. studies at Georgia Tech. I would not be able to finish my Ph.D. and become the researcher I am today without her continuous support and confidence in me all these years. I am very fortunate to have her as my advisor. I am also grateful for my thesis committee members, Dr. Lawrence Kahn, Dr. Yuanzhi Tang, and Dr. Emily Grubert, for their support and advice on both of my experimental work and dissertation writing. I want to give special thanks to an additional thesis committee member and former supervisor at National Institute of Standards and Technology (NIST), Dr. Jeffrey Bullard, whose advice and support were immensely valuable. I also want to thank my previous advisors throughout my academic development, Dr. Victor Li and Dr. Ming Xu from the University of Michigan, and Dr. Christopher Leung, Dr. Moe Cheung, and Dr. Chun-Man Chan from the Hong Kong University of Science and Technology.

I would like to thank all my current and previous lab members and friends at Georgia Tech, Prasanth Alapati, Mehdi Rashidi, Natalia Cardelino, Lisa Burris, Xenia Wirth, Emily Saad, Wenlong Zhang, Francesca Lolli, Daniel Benkeser, Cole Spenser, Scotty Smith, and LaSasha Walker, who have always been available to help my research, give me constructive advice, and review my papers and presentations. I am also deeply grateful for the precious support and help on my research from Paul Stutzman, LaKesha Perry, Kenneth Snyder, Scott Jones, Max Peltz, and Laura Mundy during my internship at NIST.

I also owe my sincere gratitude to my undergraduate assistants, Michael VanderZwaag, Luke Reeve, Evie Tripolitis, Sarah Hordern, and Sam Lucas, for helping me with experimental work and paper reviews. Beyond Ph.D. work, I am much indebted to my friends for their selfless support and friendship throughout the years of my Ph.D. study, especially to Jimmy Yonts, Hengqian Li, Anne Magnus, Qian Zhang, Leonard Cheung, Nicole Lee, Anne Menefee, Wai kit Chan, Brandon Byers, Faith Su, Zhongyu Yang, Jiwon Jeon, Hongyan Ma, and Kak Wong.

Most importantly, I would like to express my deepest gratitude towards my parents for their unconditional love and endless support. They have supported all the big decisions I made throughout my life. I still remember how happy and supportive they were when I decided to quit my structural engineering job in Hong Kong and go to the graduate school in the U.S. Without them, I could not have done my Ph.D. and would not have become the person I am today. At last, I understand it is not possible to name everyone who has helped and contributed to my Ph.D. study, but my indebtedness to them is deep in my heart.

TABLE OF CONTENTS

LIST OF TABLES

LIST OF FIGURES

LIST OF SYMBOLS AND ABBREVIATIONS

ASTM	American Society for Testing and Materials
CAC	Calcium Aluminate Cement
EDS	Energy-dispersive X-ray Spectroscopy
DOT	Department of Transportation
DTG	Thermogravimetric Derivative
EPA	Environmental Protection Agency
GHG	Greenhouse Gas
OPC	Ordinary Portland Cement
ISO	International Organization for Standardization
IC	Ion Chromatography
JIS	Japanese Industrial Standards
SEM	Scanning electron microscope
SSA	Specific surface area
TGA	Thermogravimetric analysis
XRD	X-ray diffraction

Cement Chemistry Abbreviations

A	Al_2O_3
AH_3	Gibbsite
AFm-SO_4	Alumina-ferrite-monosulfate
AFm-CO3	Alumina-ferrite-monocarbonate

C	CaO
CA	Monocalcium sluminate ($CaO \cdot Al_2O_3$)
CA_2	Grossite, calcium dialuminate
CAH_{10}	Calcium aluminate decahydrate
C_2AS	Gehlenite
C_2AH_8	Dicalcium aluminate octahydrate
C_3A	Aluminate, tricalcium aluminate ($3CaO \cdot Al_2O_3$)
C_4AF	Ferrite, tetracalcium aluminoferrite
C_3AH_6	Katoite
$C_{12}A_7$	Dodecacalcium hepta-aluminate
CC	Calcite, ($CaCO_3$)
C_2S	Belite, dicalcium silicate ($2CaO \cdot SiO_2$)
CH	Portlandite, calcium hydroxide ($Ca(OH)_2$)
C_3S	Alite, tricalcium silicate ($3CaO \cdot SiO_2$)
C-S-H	Calcium-silicate-hydrate
HNO_2	Nitric acid
HNO_3	Nitrous acid
MB	Methylene blue
N	Nitrogen
NO_x	Nitrogen oxides
NO	Nitric oxide
NO_2	Nitrogen dioxides
NO_2^-	Nitrite
NO_3^-	Nitrate

$O_2^{\bullet-}$	Superoxide radical
$OH^{\bullet}$	Hydroxyl radical
S	Silica, SiO_2
TiO_2	Titanium dioxides
UV	Ultraviolet

List of Symbols

d_{50}	50^{th} percentile particle diameter
w/c	Water-to-cement ratio
η_{NO_x}	NO_x photodegradation efficiency
Q_{NO_x}	NO_x uptake
$C_{[NO_x]_{uptake}}$	Concentration of NO_x uptake
$C_{[NO_x]_{in}}$	Inlet concentration of NO_x
$C_{[NO_x]_{out}}$	Outlet concentration of NO_x
S_{NO_x}	NO_x photodegradation capacity
m_N	N mass of NO_x uptake
m'_N	N mass of nitrite
m''_N	N mass of nitrate
M_N	Molar mass of N
$M_{NO_2^-}$	Molar mass of nitrite
$M_{NO_3^-}$	Molar mass of nitrate

SUMMARY

The ubiquity of concrete in the urban environment and the upscaling of nanomaterial production have prompted interest in the incorporation of titania (TiO_2) nanoparticles into cementitious materials. Air purification by TiO_2-based cementitious materials occurs by photocatalysts that capture nitrogen oxide species (NO_x) from the atmosphere, then oxidizing them into nitrite and nitrate species. Because nitrite- and nitrate-based corrosion inhibitors are effective in improving corrosion resistance in reinforced concrete, there is potential to develop nano-TiO_2 engineered cementitious materials that transform atmospheric NO_x into corrosion inhibitors. To provide guidelines for engineers and scientists to design such materials, a fundamental understanding of the NO_x sequestration capacity and pathways in cementitious materials is needed.

This dissertation first examines the effects of TiO_2 nanoparticles on cement hydration. The inclusion of TiO_2 nanoparticles accelerates the early age hydration of TiO_2-modified OPC pastes due to nucleation and growth effects induced by the addition of TiO_2. However, TiO_2 retards the early age hydration of CAC samples possibly due to the presence of sulfate ions on the surface of the TiO_2 nanoparticles. TGA and XRD results reveals that the early age hydration, which is affected by TiO_2 inclusion, does not affect the hydrated cementitious phase composition or proportionality after 28 days of curing. The SEM/EDS analyses show that the TiO_2 nanoparticles are uniformly distributed in the cementitious hydrates and exhibit no preference to binding with any particular hydrated phases, ensuring a consistent photocatalytic performance of the TiO_2-modified cementitious materials.

The photocatalytic performances of both TiO_2-doped and TiO_2-coated cementitious materials are examined in this research. Ordinary portland cement (OPC) samples exhibit higher NO_x and methylene blue photodegradation efficiencies than calcium aluminate cement (CAC) samples. The difference indicates that different NO_x sequestration pathways occurred in these cements and are likely due to differences in chemical composition and hydrated cementitious phases.

For TiO_2-coated cementitious materials, the inclusion of a hydrophobic SiO_2 layer improves the bonding between the TiO_2 coating and the cementitious substrates but compromises the photocatalytic efficiency. Therefore, it is important to consider the bond strength, the desired interactions between the coated surface and water, and the photocatalytic performance when selecting and designing TiO_2-coated cementitious materials.

This research also develops a novel experimental approach that combines water-based wet chemical extraction, UV-visible spectrophotometry, and ion chromatography to quantify the NO_x sequestration capacity in both plain and TiO_2-modified cementitious pastes. Compared to plain cement pastes, TiO_2-modified cement pastes exhibit higher NO_x uptake (in terms of nitrite and nitrate detected in the material) due to the activation of photocatalytic reactions, a greater surface area, and an increased amount of micropores from the addition of TiO_2. The detection of nitrite and nitrate ions in unmodified cement paste demonstrate these cementitious materials' intrinsic NO_x sequestration capacities, which are related to the surface-related catalyzed heterogeneous reactions and the alkaline environment.

To understand NO_x sequestration pathways in cementitious materials, various pure hydrated cementitious phases were synthesized, and each are exposed to NO_x gas in an instrumented and closed plug-flow reactor to evaluate their NO_x uptake capacities. Among non-carbonated phases, the highest NO_x uptake was measured in calcium silicate hydrate (C-S-H). The NO_x-converted nitrite and nitrate could either adsorb to the surface of C-S-H or dissolve in the material's pore solution. It was observed that NO_x conversion might not occur in synthetic portlandite ($Ca(OH)_2$) due to the low temperature and relative humidity used in this study. For monosulfoaluminate (AFm-SO_4), nitrite and nitrate ions were found to substitute for the sulfate ions and form new AFm-NO_2/NO_3 phases. Such anion substitution process could potentially be used to enhance chloride-induced corrosion resistance in steel-reinforced cementitious materials. To examine the effects of carbonation on NO_x sequestration, a synthetic calcite ($CaCO_3$) was examined and found that the NO_x uptake capacity was significantly improved compared to non-carbonated cementitious phases. Monocarboaluminate (AFm-CO_3) was also examined and the result indicates that the aforementioned anion substitution process could be affected.

In summary, the findings found in this research expand the knowledge of the fundamental understanding of NO_x sequestration capacity and pathways, which are essential to design cementitious materials with optimized chemical composition and microstructural properties for enhanced NO_x sequestration, thus potentially providing inhibition of corrosion.

CHAPTER 1. INTRODUCTION

1.1 Background

With increasing worldwide urbanization, the urban population has increased from 751 million in 1950 to 4.2 billion in 2018 [1]. The urban population comprises 55% of the world's population and will comprise 68% of it by 2050 [1]. Figure 1.1 shows the worldwide urban growth rate in major cities [2]. According to the United Nations, the population in the world's largest cities exceeds 20 million: Tokyo, being the world's largest city with 37 million inhabitants; Delhi, with 29 million; Shanghai, with 26 million; Mexico City and São Paulo, each with around 22 million inhabitants; and Cairo, Mumbai, Beijing and Dhaka, each with close to 20 million inhabitants [1]. To support the constantly growing worldwide urbanization, the world's concrete infrastructure systems have also experienced a rapid growth, which is reflected in the increased concrete and cement production. The global cement production has increased from 3.1 megatons in 2010 to 4.1 megatons in 2017 [3], making concrete the second most widely consumed material by mass in the world, second only to water [4].

The rapid growth of urbanization has also negatively affected air quality, generating industrial and traffic-related nitrogen oxides (NO_x), which affects the atmospheric nitrogen cycles [5]. As urban and residential areas become clustered through urbanization, this air pollution poses immediate threats to human health and environment. Therefore, it is of great interest to find a solution that can support the expanding concrete infrastructure and simultaneously improve air quality.

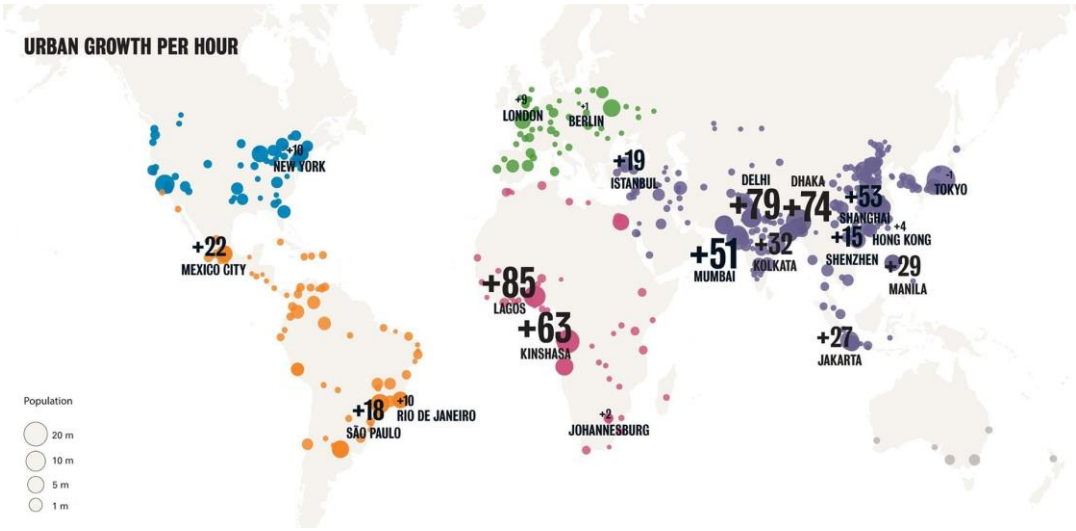

Figure 1-1: Worldwide urban growth rate (capital per hour) [2]

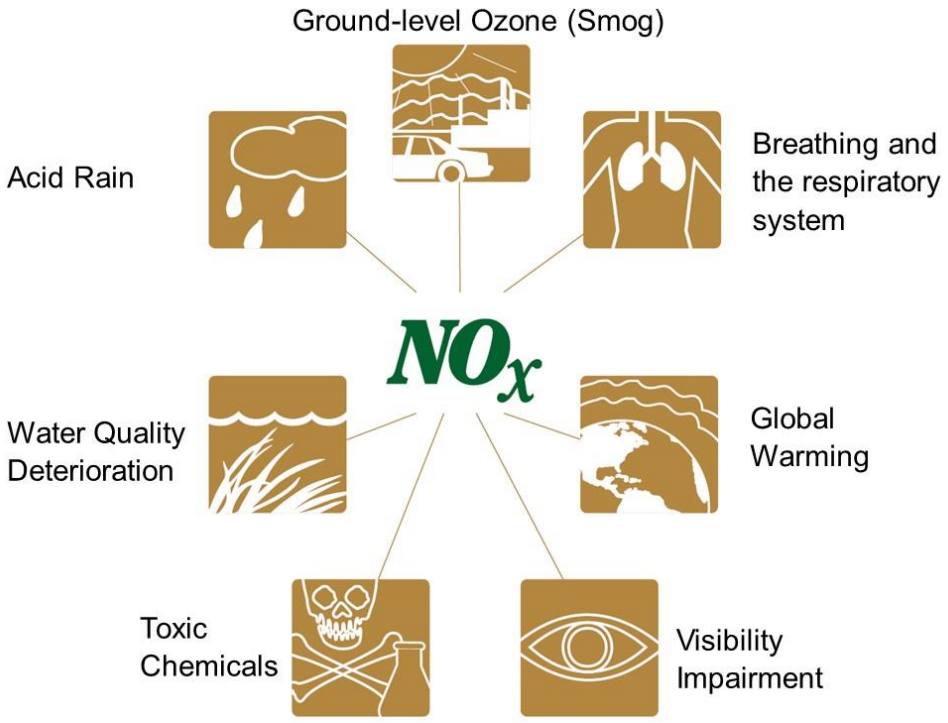

Figure 1-2: Environmental and health impacts of NO_x [6]

NO_x emissions are considered one of the most hazardous industrial and traffic-related air pollutants [6], causing a variety of environmental and health problems (Figure 1-2). NO_x is the byproduct of high-temperature combustion processes. The two most common forms of NO_x are nitric oxide (NO) and nitrogen dioxide (NO_2), and both coexist in equilibrium in the troposphere [7]. NO is directly emitted from the combustion process in fuel burning motor vehicles and electricity generation. NO_2 is produced from the interaction of NO with ozone (O_3) or molecular oxygen [8]. It can also be photolyzed by sunlight and transformed back to NO [9]. The reactions between NO and NO_2 are summarized below:

$$N_2 + O_2 \xrightarrow{heat\ of\ combustion} 2NO \qquad (1.1)$$

$$NO_2 \xrightarrow{UV\ light} NO + O \qquad (1.2)$$

$$NO + O_3 \rightarrow NO_2 + O_2 \qquad (1.3)$$

$$2NO + O_2 \rightarrow 2NO_2 \qquad (1.4)$$

Being one of the most notorious air pollutants, NO_x has numerous adverse effects on the natural environment. For example, NO_2 and sulfur dioxide (SO_2) are major contributors to acid rain [10]. Through the reactions in Equation 1.5 and 1.6, NO_2 and SO_2 form nitric acid (HNO_3) and sulfuric acid (H_2SO_4) in the atmosphere, which fall to the earth's surface in rain [10]. Acid rain damages the natural and built environments, including forests, lakes, streams, buildings, and historical monuments [11,12]. NO_x also contributes to nitrogen pollution in bodies of water by increasing the nitrogen loading in the chemical balance of nutrients in the water [13]. That additional nitrogen accelerates

eutrophication, which leads to oxygen depletion and harms the populations of fish and shellfish [13].

$$4NO_2 + O_2 + 2H_2O \rightarrow 4HNO_3 \qquad (1.5)$$

$$2SO_2 + O_2 + 2H_2O \rightarrow 2H_2SO_4 \qquad (1.6)$$

When NO_x and volatile organic compounds (VOCs) react with heat and sunlight, their chemical byproducts contribute to the formation of ground-level smog, such as peroxyacetyl nitrate (PAN, Equation 1.7) and ozone. Additionally, ozone can also be produced through the reaction between the oxygen atom that is released from the photocatalyzed NO_2 reaction (Equation 1.2) and atmospheric oxygen (Equation 1.8). Ozone can damage vegetation, forests, and agricultural crops, and also serves as a greenhouse gas that contributes to global warming [14]. When accumulated in the atmosphere, ozone and other greenhouse gases cause a gradual rise in earth's temperature and sea levels, ultimately posing risks to human and other animal habitats [15].

$$NO_2 + O_2 + \text{hydrocarbons} \xrightarrow{sunlight} CH_3COOONO_2 \qquad (1.7)$$

$$O + O_2 \rightarrow O_3 \qquad (1.8)$$

Besides environmental problems, NO_x also causes health problems. NO_x impairs the human respiratory system by forming acid vapor (Equation 1.5) and harmful particles (Equation 1.7), which penetrate deep into sensitive parts of the lungs and cause respiratory diseases such as pulmonary emphysema, diffuse lung injury, and chronic bronchitis [16]. The nitrate particles and nitrogen dioxide also cause impaired visibility by blocking the transmission of light and absorbing visible solar radiation [17].

Due to the increasing threats of NO_x on the natural environment and human health, NO_x emissions have been closely monitored and reported globally. According to Miyazaki, et al. [18], the regions with high NO_x emission are eastern Asia (mainly China), Europe, and the U.S. (Figure 1-3 [18]). Their high NO_x emissions are due to the rapid growth in population and businesses in cities, which must respond to constantly growing demands for mobile resources and energy support, in particular fuel-burning plants. In China, the annual NO_x emission has increased from 10 Mt in 1995 to 25 Mt in 2010, and the major contributors are the transportation (25.4%) and powerplant sectors (34.5%) [19]. In Europe, total NO_x emissions have decreased by 44% between 1990 and 2011 due to increased use of public transportation and a more restricted policy of direct air pollution emissions. However, the annual NO_x emissions of countries such as Germany, Italy, and the United Kingdom, still exceed 1 Mt in each country [20]. Additionally, the ambient urban concentrations of NO_x in major European cities (e.g. Athens, Berlin, Madrid, Paris, and Rome) are still increasing [21]. The most significant sectors of NO_x emissions are road transportation (41%) and energy production and distribution (23%) [20]. In the United States, total NO_x emissions have decreased from 25 Mt of emission in 1990 to 14 Mt in 2011. The major contributors are transportation (41%) and fuel combustion (27%) [22]. However, the trend of NO_x emissions and concentration in large cities is still increasing [23]. Therefore, the worldwide mission of controlling the atmospheric NO_x level remains critical.

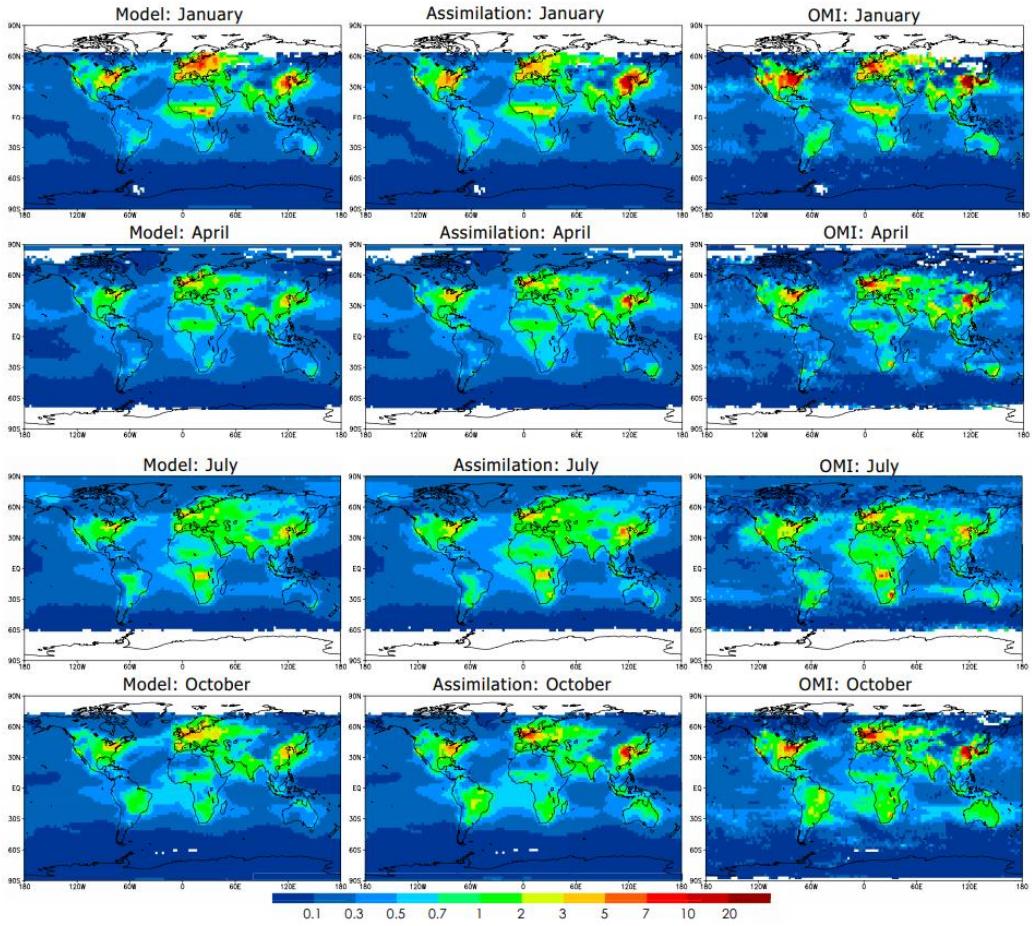

Figure 1-3. Global distribution of the tropospheric NO_x emission [18]**.**

In recognition of the adverse effects of NO_x and its continuous global emission, decades-long efforts have been made to reduce NO_x levels globally. The efforts have been mainly focused on environmental legislation [24], improvements in combustion efficiency and technologies to reduce post-combustion NO_x [25], employment of alternative fuels [26], development of clean energy resources [27], and NO_x sequestration [28].

Among these strategies and technologies for NO_x abatement, titanium dioxide (TiO_2) photocatalysts have gained great interest for sequestering atmospheric NO_x in recent decades [29], especially when it is applied in the concrete industry [29]. TiO_2 is a well-known photocatalyst that can effectively remove NO_x from the atmosphere in the presence

of water, oxygen, and UV or near UV-light. The detailed mechanism of the photocatalytic reactions will be discussed in Chapter 2 Literature Review. Due to the ubiquity of concrete infrastructure, the application of TiO_2 in cement-based concrete infrastructure could potentially be the most effective way to improve the air quality through NO_x removal while maintaining the needs for expanding infrastructure. For example, concrete paving blocks containing, or being coated with, TiO_2 photocatalysts [30,31] have been shown to reduce the motor vehicle emission-derived NO_x in Europe [32,33]. Moreover, there are growing interests in expanding the applications of TiO_2-modified cement-based materials in the structures such as concrete bridges and buildings [32,33]. Therefore, this research is motivated using TiO_2-modified cementitious materials to mitigate the harmful impacts of NO_x emission.

1.2 Research Motivation

The introduction of TiO_2 in portland cement-based concrete has been extensively studied during the past decades and the previous research includes: photocatalytic oxidation reactions in TiO_2-doped cementitious materials [34]; the manner of photocatalyst addition (for example, interblended vs. coatings) [35,36]; the effects of cementitious material nanostructure, microstructure, and surface features on photocatalytic performance in the presence of TiO_2 nanoparticles [31,37]; the effects of mixing and operation conditions on photocatalytic efficiency [33,38]; and, the feasibility of using alternative cementitious materials in combination with TiO_2 nanoparticles [39]. The majority of these studies have been focused on characterizing and enhancing the photocatalytic performance.

Recently, Lee [40] has made some efforts on investigating the effects of TiO_2 nanoparticles on early age hydration, mechanical properties, and durability of TiO_2-modified cementitious materials. However, despite the considerable efforts in the above areas, a fundamental understanding of the NO_x sequestration pathway in cementitious materials remains elusive.

Such information can only be obtained by examining the interaction between cementitious materials and N species that are produced during NO_x degradation. Because different N species have chemical differences, each species can interact differently with cementitious materials. For example, a given species has the potential to dissolve in the alkaline pore solution [41], to adsorb to the surfaces of hydrated phases [41], or to chemically interact with hydrated phases by substituting for sulfate ions within the structures of aluminum-bearing hydrated phases (AFm and AFt) [42]. Therefore, in addition to the early age hydration and mechanical properties, the relationship between the NO_x uptake and the microstructural properties of TiO_2-modified cementitious materials is critical for understanding how cementitious materials play a role in NO_x sequestration.

This information can also help improve the durability of cement-based concrete. Previous studies have demonstrated that the nitrite and nitrate could be the major N species that are produced during NO_x degradation [34], and these species can help enhance corrosion inhibition against chloride-induced corrosion when incorporated into steel-reinforced cementitious materials [43]. This type of corrosion inhibition can be achieved by adjusting the nitrite or nitrate ion concentrations to attain a desirable ratio with chloride ion concentrations [44], knowing that nitrates are considered better inhibitors than nitrites [45]. Since studies have also shown that aluminum-bearing phases can help enhance such

corrosion inhibition, aluminate-rich cement is also of interest in this study. Therefore, the information about the pathway and mass distribution of N species and their interactions with complex cementitious materials can help design a novel cementitious material with optimal NO_x sequestration and corrosion resistance in steel-reinforced cementitious materials.

1.3 Objectives

The primary goal of this research is to expand the knowledge of NO_x sequestration in cementitious materials, in terms of its capacity and pathways. With such information, the TiO_2-engineered cementitious material can be designed and optimized for multi-functionalities, including NO_x removal, corrosion inhibition, and self-cleaning. In order to reach this goal, this dissertation aims to meet the following five main objectives:

- To comprehend the effects of TiO_2 nanoparticles on the hydration and hydration products of cement using various techniques, including isothermal calorimetry, thermogravimetric analysis (TGA), X-ray diffraction (XRD). Two types of cement, ordinary portland cement (OPC) and calcium aluminate cement (CAC), are used. TiO_2 from two different manufacturers are used at an added level of 5% and 10%. The results are compared with both plain OPC and CAC materials.
- To evaluate the photocatalytic performance of TiO_2-doped plate samples, including NO_x photodegradation efficiency and capacity. The photodegradation experiments are performed in a customized reaction chamber and the test procedure follows the ISO 22197 [46] and JIS R 1701 standards [47]. The long-term photocatalytic

performance is also examined by carrying out a consecutive multi-cycle test. Both TiO_2-doped OPC and CAC plate samples are tested. In addition, scanning electron microscope (SEM) coupled with an energy-dispersive X-ray spectroscopy (EDS) are also used to examine the dispersion of TiO_2 nanoparticles in hydrated cement, as well as their association with hydrated phases.

- To evaluate the photocatalytic performance and self-cleaning performance of TiO_2-coated plate cementitious samples using NO_x and methylene blue (MB) dye photocatalytic degradation tests. Various coating methods are used to examine the hydrophobicity of coated surfaces and the interactions between photocatalytic coatings and cementitious substrates are examined through wettability and adhesion, respectively. Both TiO_2-coated OPC and CAC plate samples are tested.
- To quantify the total N uptake from NO_x degradation in both plain and TiO_2-doped cementitious materials. The crushed samples are used to increase the NO_x uptake potential for detectability. A novel combination of wet chemical extraction, ultraviolet-visible (UV-vis) spectrophotometry, and ion chromatography (IC) measurements is developed and employed to quantify the concentration and relative percentages of N species for both plain and TiO_2-doped cementitious materials. The total nitrogen uptake from the photocatalytic degradation test is compared with the total nitrogen from N species measurements to validate the test methods. The measured concentrations of N species are used to quantitatively compare the efficiencies of NO_x sequestration among different cementitious materials. Both TiO_2-doped OPC and CAC crushed samples are tested. N_2 adsorption and desorption coupled with the Brunauer, Emmett, Teller (BET) theory are also employed to

examine the specific surface area and pore size distribution of crushed samples. The relationship between NO_x uptake capacity and these microstructural properties are also formulated.

- To fundamentally understand NO_x sequestration pathways in cementitious materials, pure cementitious phases are synthesized and used to quantify the NO_x sequestration uptake and binding mechanisms. Three major hydrated phases are examined: calcium silicate hydrates (C-S-H), monosulfate aluminate (AFm-SO_4), and portlandite (CH). The concentration and relative percentages of N species are determined by the same experimental approach from the previous objective. XRD are also employed to examine the reaction mechanism and identify changes in chemical composition during NO_x sequestration. The effects of carbonation of these phases on NO_x sequestration are also investigated by performing the same tests on calcite (CC) and AFm-CO_3.

1.4 Organization of Dissertation

The overall research approach and the structure of the dissertation, including material design, experimental program, performance evaluation, and research objectives for each chapter are outlined below:

- Chapter 2 presents a thorough literature review on the background of TiO_2 photocatalysts, TiO_2-modified photocatalytic cementitious materials, application of photocatalytic cementitious materials, experimental program of NO_x photodegradation tests, hydration of calcium aluminate cement, durability of

photocatalytic cementitious materials, and the nitrite/nitrate related corrosion inhibition.

- Chapter 3 presents the effects of the incorporation of TiO_2 nanoparticles on the hydration and hydration products of TiO_2-doped OPC and CAC materials. The results include early age hydration obtained from isothermal calorimetry and the hydrated cementitious phases identified by TGA and XRD analyses, which will be used in later chapters for characterizing photocatalytic efficiency with the microstructural property of TiO_2-doped cementitious materials.
- Chapter 4 presents the results of photocatalytic performance of TiO_2-doped OPC and CAC plate samples. TiO_2 dispersion and association with hydrated phases are investigated by coupled SEM and EDS techniques. Both photocatalytic efficiency and capacity are quantified.
- Chapter 5 present the results of NO_x and MB dye photodegradation to evaluate the air-purification and self-cleaning properties of TiO_2-coated OPC and CAC plate samples, respectively. The results of hydrophobicity of coated surfaces and the interactions between photocatalytic coatings and cementitious substrates are also reported.
- Chapter 6 presents the quantification of NO_x sequestration in TiO_2-doped OPC and CAC crushed samples. The total N uptake from the NO_x photodegradation test is compared with the total nitrogen from nitrite and nitrate measurements. The specific surface area and pore size distribution of plain and TiO_2-doped samples are determined by N_2 adsorption and desorption. The detailed development of combined

experimental approach of wet chemical extraction, UV-vis spectrophotometry, and ion chromatography is also included.

- Chapter 7 presents the results of NO_x uptake in single cementitious phases, together with XRD analysis. The pathways of NO_x sequestration, therefore, can be determined in terms of binding mechanisms for each individual pure cementitious phase.
- Chapter 8 provides a summary of the research and key conclusions. Future studies are also recommended based on the outcome of the current research.

CHAPTER 2. LITERATURE REVIEW

2.1 Photocatalytic cementitious materials

Given the ubiquity of concrete infrastructure, the incorporation of titanium oxide (TiO_2) in cementitious materials has attracted growing attention in the construction and building industry [29]. Due to the photocatalytic nature of TiO_2, which will be discussed in detail in the following section, the resultant cementitious materials after the incorporation of TiO_2 are regarded as photocatalytic cementitious materials. This section of the chapter will first review the material properties of TiO_2 photocatalysts, and then it will introduce two major photocatalytic cementitious materials: TiO_2-doped cementitious materials and TiO_2-coated cementitious materials.

2.1.1 TiO_2 photocatalysis

TiO_2 has been used as a white pigment in paints, cosmetics and food coloring since ancient times [48]. The white color is due to TiO_2 having no absorption in the visible region [49]. In 1956, Japanese scholars started using the photochemical power of TiO_2 in various organic solvents such as alcohols and hydrocarbons, using UV irradiation [50]. In the early 1970s, water photoelectrolysis, also known as the "Honda-Fujishima effect", was discovered and reported in the Nature article [29]. In the study, a semiconductor of TiO_2 electrode was used to facilitate hydrogen evolution under UV radiation. Since then, the field of TiO_2 photocatalysis has experienced major developments every ten years for the last several decades. The production of photocatalytic H_2 was reported in the 1980s [49]

and hydrophilic TiO_2 films and coatings were developed in the 1990s [51]. The combination of photocatalytic oxidation reactions of adsorbed substances and the photo-induced hydrophilic conversion of TiO_2 itself has led to a broad range of applications, particularly in building materials and environmental applications [49]. During the 21st century, TiO_2 has become a practical technology for photocatalytic removal of volatile organic compounds (VOCs) [52,53], water treatment of hydroponic systems [49], antibacterial metal applications [54,55], surface self-cleaning [56], and air purification through smog abatement [32,52,57].

There are three crystal structures of TiO_2: anatase, rutile and brookite [58,59] (Figure 2-1), among which the anatase structure is the most widely used due to its higher photoactivity [60]. Since TiO_2 is relatively inexpensive, safe, and chemically stable, and has high compatibility with traditional cementitious materials like concrete, TiO_2 is attractive to use in building materials [52]. When the photocatalytic cementitious material-based structure is exposed to the sun, the high photocatalytic capability of TiO_2 can be activated under solar irradiation from the ambient atmospheric environment. The following sections will introduce the two most studied photocatalytic cementitious materials: TiO_2 nanoparticle-doped and TiO_2-coated cementitious materials.

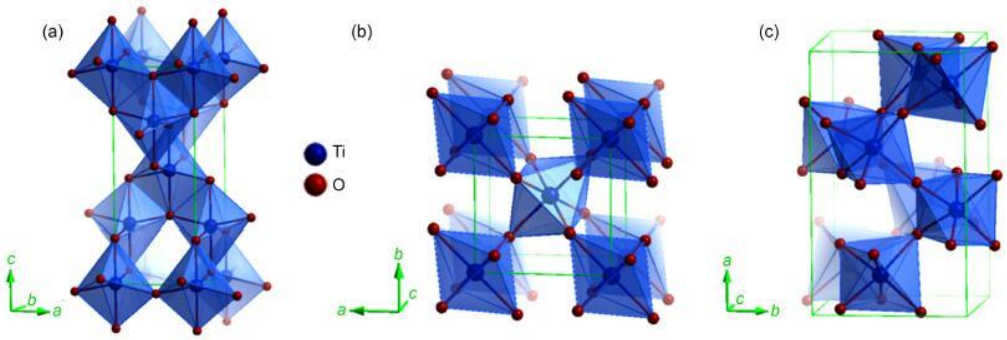

Figure 2-1: Crystal structure of TiO_2 (a) anatese, (b) rutile, and (c) brookite

2.1.2 TiO_2 nanoparticle-blended cementitious materials

The photocatalytic cementitious materials can serve as both photocatalytic materials and structural materials such as exterior tiles, paving blocks, glass mirror, and PVC fabric [52]. In these building and construction applications, TiO_2 nanoparticle-doped photocatalytic cementitious materials are more widely used than TiO_2-coated materials due to the concerns of TiO_2 coating losing in-the-field applications from wear and weathering [33,61]. Research regarding the TiO_2 nanoparticle-blended application has been focused on the following aspects: the effects of cementitious material nanostructure, microstructure, and surface features on photocatalytic performance in the presence of TiO_2 nanoparticles [35,36,61], the effects of mixing procedures and environmental conditions on photocatalytic efficiency [33,38], the effects of TiO_2 nanoparticles on the early hydration and mechanical properties of TiO_2 nanoparticle-doped photocatalytic cementitious materials [40,62], and the feasibility of using alternative cementitious materials in combination with TiO_2 nanoparticles [39]. Despite the considerable efforts in the above areas, a fundamental understanding of the capacity and pathway of sequestered

NO_x in the cementitious materials remains elusive. This dissertation aims to address this issue.

2.1.3 TiO_2-coated cementitious materials

Although there are concerns of TiO_2 coating loss with in-the-field applications, the use of TiO_2 photocatalytic coating on the surface of cementitious material is attracting a growing attention for several reasons. First, because photocatalytic NO_x abatement is a surface phenomenon [34], it would be more efficient to apply the photocatalytic coatings directly to the surface of cementitious material [34]. Second, the TiO_2-coated cementitious materials are considered to have less embodied energy than TiO_2-blended ones [63]. A life cycle analysis carried out by Jayapalan, et al. comparing a TiO_2-based cement paste with plain cement paste showed that TiO_2-based cement nearly doubles the material's embodied energy, even when only 5% by weight TiO_2 is blended in the cement paste [63].

To address the durability concerns of a TiO_2 coating and reduce the production cost, previous studies have proposed using titania-silica (TiO_2-SiO_2) composites as a photocatalytic coating since SiO_2 has higher mechanical and thermal stability than TiO_2 [64–66]. Moreover, the production of SiO_2 is even less expensive than TiO_2 [64]. In addition to lower cost and higher durability, the introduction of SiO_2 also increases the photocatalytic efficiency because its large surface area helps adsorb pollutants and intermediates for longer periods than pure TiO_2 [64]. SiO_2 can also alter the hydrophilicity of TiO_2-SiO_2 coatings [67], which could help address the durability problems of cementitious substrates due to the penetration of water and aggressive chemicals when

exposed to atmospheric conditions of relative humidity greater than 50% [68]. Although the addition of SiO_2 improves the durability of the coating itself, the bond between the coating and the surface of cementitious materials must be carefully examined and the bond's durability must be ensured to avoid compromising the durability performance of the coated photocatalytic cementitious materials. This study also addresses these concerns and the detailed investigation and discussion will be provided in Chapter 5.

2.2 Applications of TiO_2-modified cementitious materials

TiO_2-modified photocatalytic cementitious materials have various applications. This section will first review two most common applications, namely air purification and self-cleaning, in terms of the mechanism and current research. In addition, a relatively novel application of corrosion inhibition from TiO_2-modified cementitious materials will also be reviewed. As discussed in the introduction, this research is primarily motivated by these applications.

2.2.1 Air purification

For air purification, both organic and inorganic air pollutants can be degraded by photocatalytic cementitious materials that contain TiO_2 [52]. The degradation mechanism is summarized below [69,70]. When TiO_2 absorbs a photon containing the energy equal to or larger than the band gap, an electron (e^-) is promoted from the valence band (VB) to the conduction band (CB), which results in an electron vacancy, a "hole", in the VB (h^+). The

band gap energy of TiO_2 corresponds to the irradiation of UV light ranging from 300-400 nm wavelength, which contains the UV light range (360-380 nm). The generation of the electron-hole pair is summarized in the following reaction:

$$TiO_2 \xrightarrow{h\nu} TiO_2 + e^- + h^+ \quad (2.1)$$

The h^+, with its strong oxidation power, reacts with water to form a highly reactive hydroxyl radical ($OH^\bullet$) (Equation 2.2). The e^-, with its reducing power, reacts with molecular oxygen to form a superoxide radical ($O_2^{\bullet-}$) (Equation 2.3).

$$h^+ + H_2O \rightarrow^+ + OH^\bullet \quad (2.2)$$

$$e^- + O_2 \rightarrow O_2^{\bullet-} \quad (2.3)$$

Both superoxide and hydroxyl radicals break down organic and inorganic pollutants in a chain of reactions. For the case of the VOCs, most organic air pollutants can be completely degraded by hydroxyl radicals to innocuous final products such as CO_2 and H_2O. For the case of NO_x, NO and NO_2 are oxidized by superoxide and hydroxyl radicals. The oxidation leads to the formation of nitrite (NO_2^-) and/or nitrate (NO_3^-) ions through a series of photocatalytic oxidation reactions listed below [71,72]:

$$NO + O_2^{\bullet-} \rightarrow NO_3^- \quad (2.4)$$

$$NO + OH^\bullet \rightarrow NO_2^- + H^+ \quad (2.5)$$

$$NO + OH^\bullet \rightarrow HNO_2 + OH^\bullet \rightarrow NO_2 + H_2O \quad (2.6)$$

$$NO_2 + OH^\bullet \rightarrow NO_3^- + H^+ \quad (2.7)$$

Although the exact mechanism of NO_x photocatalytic abatement is not fully established, the above reactions are generally accepted, and the final products of NO_x photocatalytic oxidation are believed to be nitrous acid (HNO_2) and nitric acid (HNO_3) [52], i.e. nitrite and nitrate ions. These products accumulate on the surface of photocatalytic cementitious materials, which may inhibit the photocatalytic reaction [52]. However, the accumulation can easily be washed away by water since nitrous acid and nitric acid are soluble [73]. Researches have shown that once the products are removed by rain or other water sources, the photocatalytic activity is restored [52].

2.2.2 Self-cleaning

Greasy deposits such as fatty acids adhere to building surfaces [74]. The carboxylic groups (-COOH) of fatty acids enable them to stick on the building surface by chemically binding with calcium ions present in concrete [74]. Their long chains link with other hydrophobic molecules and perpendicularly extend from the building surface, trapping more atmospheric particles and dust [52]. The cost of cleaning these stains and deposits is high, especially in high-rise buildings. Therefore, the self-cleaning property of photocatalytic cementitious materials is of great interest as it can help maintain the aesthetic characteristics of concrete in urban environments while minimize the cleaning expenses [28,74,75].

The mechanism of the self-cleaning property is considered a chain reaction. First, the high redox power of photo-induced electron-hole pairs (Equation 2.1) can decompose the organic binders in the following manner (with palmitic acid as an example).

$$n\text{-}C_{15}H_{31} – COOH + h^+ \rightarrow n\text{-}C_{15}H_{31} – COO + H^+ \rightarrow n\text{-}C_{15}H_{31}^{\bullet} + CO_2 + H^+ \quad (2.8)$$

After the release of the first CO_2, the $n\text{-}C_{15}H_{31}^{\bullet}$ are oxidized by hydroxyl radicals to an alcohol, and then further oxidized into acid $n\text{-}C_{14}H_{29} – COOH$ (Equation 2.9), which will undergo similar reactions to release the second CO_2. The chain of reaction continues until the acid is completely decomposed to CO_2 and H_2O.

$$n\text{-}C_{15}H_{31}^{\bullet} + OH^{\bullet} \rightarrow n\text{-}C_{15}H_{31}OH + O_2 \rightarrow n\text{-}C_{14}H_{29} – COOH + H_2O \quad (2.9)$$

2.2.3 Corrosion inhibition

In addition, nitrite and nitrate ions that are produced in photocatalytic reactions can serve as corrosion inhibitors in steel-reinforced cementitious materials. Two mechanisms have been proposed for the enhancement of corrosion inhibition by nitrite and nitrate ions. First, the nitrite and nitrate ions can serve as anodic corrosion inhibitors. The mechanisms of their corrosion inhibition abilities are summarized in the following reactions [45]:

For nitrite:

$$2\ NO_2^- + 3\ H_2O + 4\ e^- \rightarrow N_2O + 6\ OH^- \quad (2.10)$$

$$4\ Fe(OH)_2\ (s) + 4\ OH^- \rightarrow 4\ Fe(OH)_3\ (s) + 4\ e^- \quad (2.11)$$

For nitrate:

$$2\ NO_3^- + 2\ H_2O + 4\ e^- \rightarrow 2\ NO_2^- + 4\ OH^- \quad (2.12)$$

$$2\ Fe(OH)_2\ (s) + NO_3^- + H_2O \rightarrow 2\ Fe(OH)_3\ (s) + 2\ NO_2^- \quad (2.13)$$

Since nitrate can be easily reduced to nitrite by ferrous iron in an alkaline solution (Equation 2.13), the remaining nitrite ions can further react with ferrous iron (Equation 2.11). As a result, three more moles of ferrous iron are oxidized to ferric iron per mole of nitrogen oxide, which indicates that nitrate could be a better inhibitor than nitrite by a magnitude of three. Therefore, determining the amount of nitrite and nitrate formed during NO_x degradation reaction in photocatalytic cementitious materials is important in predicting the efficiency of corrosion inhibition.

The second mechanism of corrosion inhibition by nitrite and nitrate is proposed by Sant, et al. [43]. They have experimentally demonstrated that nitrite and nitrate ions can substitute for sulfates in AFm phases to form AFm-nitrite/nitrate [42]. With that result, Sant at al. [76] have proposed that an AFm-nitrite/nitrate rich concrete can be used to sequestrate chlorides through an anion capture and exchange process while simultaneously releasing nitrite and nitrate species, resulting in the delay of the initiation and progress of chloride induced corrosion and thereby prolong the service life.

This idea of using AFm-nitrite/nitrate corrosion inhibition has already been applied to concrete overlays, and the detailed analysis and quantification of how this AFm-nitrite/nitrate rich concrete overlay can prolong the service life can be found in Sant, et al. [44]. The fundamental understanding of the sequestration pathway of nitrite and nitrate species in cementitious materials can further facilitate the optimal design this corrosion inhibition by using the photocatalytic cementitious materials developed in this study, which help transform the smog-producing NO_x into corrosion inhibitors.

2.3 Experimental program

Different standardized tests have been developed for examining the photocatalytic properties of TiO_2-modified cementitious materials. The air-purification property is commonly examined by the NO_x photocatalytic degradation test [52] and the self-cleaning property is examined by MB dye photocatalytic degradation test [77]. The experimental programs of both tests are reviewed in this section.

2.3.1 NO_x photodegradation

Three major testing standards are commonly used to examine NO_x degradation and to characterize the air purification performance of photocatalytic cementitious materials: the Japanese standard (JIS R 1701-1) [47], the ISO standard (ISO 22197-1) [46] and the Italian standard (UNI 11247) [78]. The testing parameters and sample preparations for each standard are reviewed here.

The standard was first developed by the Japanese Standards Association in 2004 and is the JIS R 1701-1 standard entitled "Fine ceramics (advanced ceramics, advanced technical ceramics) – Test method for air purification performance of photocatalytic materials – Part 1: Removal of nitric oxide [47]." JIS R 1701-1 has been widely used for photocatalytic properties of construction materials. In this method, a continuous flow of testing gas passes over the surface of testing samples through a photo-reactor, and the concentration of testing gas is continuously measured by a chemiluminescent NO_x analyzer. The standard suggests using a flat plate testing sample with surface dimensions of 50 mm wide by 100 mm long. In other words, a total surface area of at least 5000 mm^2

is recommended in this test standard. The distance between the sample surface and the window plate should be 5 mm for the testing gas passing through. An ultraviolet (UV) light source with wavelengths of 300-400 nm is placed on top of the reactor, producing an irradiance of 10 W/m^2. The standard specifies using NO gas at 1.0 ppm with 50% relative humidity at 25 ± 2.5°C and a flow rate of 3.0 L/min. It should be noted that the NO_x gas used in this test is prepared by mixing the nitric oxide (NO) gas in ultrapure dry air. The NO_x gas needs to be stabilized before turning on UV illumination. After the level of NO_x gas is stabilized, the samples then are exposed to UV light for a continuous 5 hours. The whole test should be conducted in a light-blocking environment to prevent ambient light from affecting the reaction. The photocatalytic conversion is measured by integrating the difference between the input and output concentration of the gas. After the experiment, elution tests are performed on the cementitious samples to measure nitrate and nitrite ions produced during the reaction and, in turn, to confirm the NO_x conversion efficiency.

The ISO 22197-1 standard, entitled "Fine ceramics (advanced ceramics, advanced technical ceramics) – Test method for air-purification performance of semiconducting photocatalytic materials – Part1: Removal of nitric oxide [46]" was established in 2007, and follows the same procedures as the JIS standard.

The UNI 11247 was developed in 2010 by the Italian organization for standardization (UNI) for building materials with photocatalytic activity [78]. The test is similar to the JIS/ISO standards, where a constant concentration of test gas flows through a reactor while UV light is irradiated. However, the proposed testing gas is different from the previous two standards. UNI uses a mixed gas with 0.55 ppm of total NO_x, containing a mixture of 0.15 ppm of NO_2 and 0.40 ppm of NO. The UV light irradiance is doubled

from the JIS/ISO standards to 20 W/m^2 and the total duration of UV exposure is counted 1 hour after gas stabilization. The other parameters are similar to the JIS/ISO standards. The use of mixed gas ($NO+NO_2$) in the UNI standard could simulate a real-world environmental condition. However, due to the interconversion between NO and NO_2 during photocatalytic reactions, the setup of mixed gas could make analytical work inaccurate, especially for studying the NO_x binding mechanism.

Therefore, the NO_x degradation test used in this research is based on the JIS and the ISO standards. Since different types of samples are tested in this research for different characterization purposes and research objectives, some modifications are applied in the actual test methods used in this research. Therefore, the detailed descriptions for the experimental methods for each test should be referred to the corresponding chapter. Moreover, this research proposes a novel experimental approach that combines wet-chemical extraction, ultraviolet-visible spectrophotometry, and ion chromatography measurements to accurately measure the nitrite and nitrate ions. Although, these methods have been used to in determine nitrite and nitrate concentration in other systems [79,80], this is first time it has been used in cement-based materials. The total N mass of NO_x photodegradation is compared with total N mass from nitrite and nitrate detection to verify the aforementioned experimental approach. The detailed experimental approach is provided in Chapter 6.

2.3.2 Methylene blue (MB) dye photodegradation

To determine the self-cleaning activity of the surface of the TiO_2-modified cementitious materials, ISO standard: 10678:2010 – "determination of photocatalytic activity of surface in aqueous medium by degradation of methylene blue", is the most commonly used [81]. Although this standard is based on water remediation, it still provides useful guidance to measure the ability of a photocatalytic coated surface to clean the deposited organic species by observing the destruction of a pollutant. To demonstrate this effect, a dye, specifically MB dye, is used as a test pollutant since only a small amount of material is needed to show a striking color change as the dye is photo-oxidized. The complete photo decomposition of MB dye ($C_{16}H_{18}N_3SCl$) by titania films follows the following reaction [82].

$$C_{16}H_{18}N_3SCl + 25\frac{1}{2}O_2 \xrightarrow{TiO_2, hv \geq 3.2\ eV} HCl + H_2SO_4 + HNO_3 + 16CO_2 + 6H_2O \quad (2.14)$$

The common chemical structure of MB is shown in Figure 2-2 [83], together with its colorless and reduced form of leuco-MB or LMB. The popularity of using MB dye for the test is due to its large molar absorptivity, non-toxic nature, high solubility in water, stability in an aqueous solution, and its ongoing applications and availability for textile, leather, and paper dye [83].

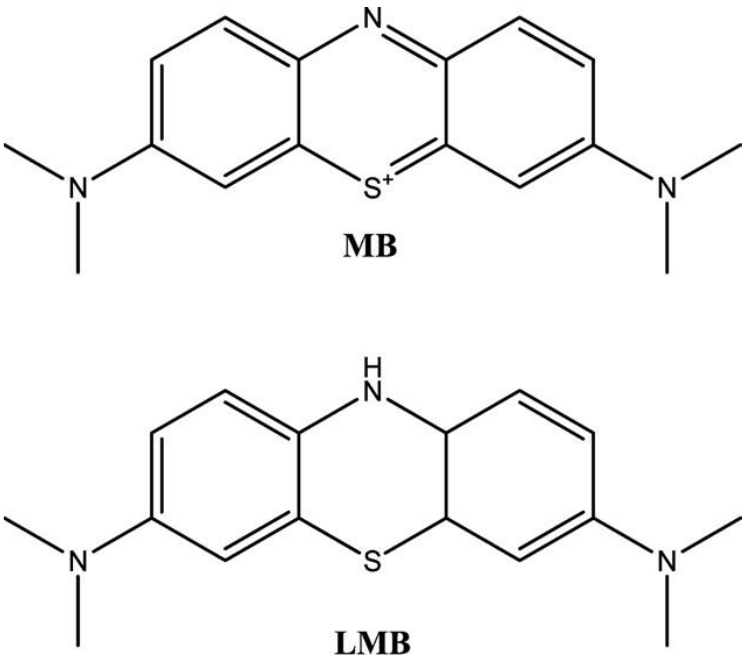

Figure 2-2: Structure of methylene blue (MB) dye and its colorless leuco-MB [83].

The standardized test [81] uses a plate sample of 10 cm^2 with an active coating and a glass cylinder with a diameter of about 4 cm is fixed on top of the sample. An MB solution containing 2×10^{-5} mmol of MB is prepared and stored in the dark for 12 hours prior to the test, during which if the concentration of MB reaches lower than 10^{-5} mmol during this period, preparation must be repeated using a fresh conditioning solution. Otherwise, the 35 mL of solution is placed in the cylinder, which is then covered with a UV transparent glass pane, such as borosilicate. The system is then under the radiation of a UV light with a wavelength of 1.0 mW/m^2 and a narrow-band emitter such as a blacklight blue (BLB) lamp should be used. The concentration of the MB solution is measured by a spectrophotometer at a wavelength of 664 nm as a function of irradiation time. The irradiation process is carried out for 3 hours, or until whenever the solution is decolorized, whichever happens first. The reaction temperature should be 23 ± 2 ˚C. A blank control group should also be

tested under a dark environment. The photocatalytic efficiency of the system can be calculated based on the relationship between the MB concentration and irradiation time. For testing the self-cleaning properties of photocatalytic cementitious materials, previous studies have applied MB dye drops on the coated surfaces and a similar measurement of discoloration is followed as previously mentioned [84].

The biggest advantage of this method is simplicity. However, this simplicity is based on several underlying assumptions, which could cause potential errors and increase uncertainties. The main assumptions that could be problematic have been identified by Mills [83], who also provided suggestions for improving such concerns. The ones that are the most relevant to this study are listed here: (i) the purity of MB dye: studies have shown significant variations in an impure MB source [85] and Mill [83] suggested to use a known source of MB dye and self-validate its purity before using it; (ii) pH: a pH, whose value is below the zero charge of the semiconductor, would be ideal for this test. In the case of TiO_2, the pH value of the zero charger should be 6.6 [86], therefore, Mill [83] suggested the initial pH of the MB dye should be in the range of 5.5–6.0 for the test; (iii) light source: the standard recommends a narrow-band light source in the range of 320-400 nm. Mill [83] argued that such a loosely defined light source could cause significant variations and suggested that the BLB UVA light with a europium-doped strontium fluoroborate or borate phosphor should be used. Despite these concerns, previous studies [84] have demonstrated that the application of such tests in photocatalytic cementitious materials can still provide useful insights, in particular the correlation between MB photo-degradation and photocatalytic self-cleaning behavior.

2.4 Effect of nano-TiO_2 on cement hydration

Two types of cements are studied in this research: (1) ordinary portland cement (OPC), which is currently the most commonly used cement in the world [87], and (2) calcium aluminate cement (CAC), which is an alumina rich cement and its aluminum-bearing hydration phases can be used to enhance the potential of inhibiting chloride-induced corrosion as described in Section 2.3.3. Since the NO_x uptake capability of cementitious materials depends on their microstructural properties and surface features, which also depend on their hydrated cementitious phases, this section reviews the existing studies regarding the effects of TiO_2 additions on the hydration of these two cements.

2.4.1 Ordinary portland cement (OPC)

The effects of TiO_2 additions on early age hydration of OPC have been studied previously by Lee [40], where she also investigated various dosages of TiO_2 nanoparticles within a range of 0% to 10%. She found that the addition of TiO_2 accelerates early hydration of OPC and suggested that the acceleration was likely due to the nucleation and growth effects. In her study, she also found that the final setting time of TiO_2-modified OPC is shorter than plain OPC, while the initial setting could vary based on the dispersibility and particle size of TiO_2 nanoparticles. In terms of compressive strength, she concluded that the addition of TiO_2 nanoparticles does not compromise the compressive strength even up to a 10% addition. In addition to OPC, Lee [88] also carried out similar studies on alite and belite, two of the main ingredients of OPC. Again, the early age

hydration of alite and belite are accelerated by a TiO_2 addition due to the nucleation and growth effects.

However, despite the effort of early age hydration of TiO_2 additions, several key properties remain elusive, in particular the late age hydration behavior, hydration products, and microstructural features, and dispersion of TiO_2 nanoparticles in TiO_2-modified OPC, especially after 28 days of curing. These properties are particularly important because they are more likely related to the photocatalytic activity of cementitious materials once they are placed in the field. Therefore, this study provides a comprehensive study on the hydration and microstructural properties of TiO_2-modified OPC in Chapter 3.

2.4.2 Calcium aluminate cement (CAC)

CAC has very different chemical compositions and hydration reactions from OPC. The main difference is that CAC has a high alumina content, which is in the form of monocalcium aluminate (CA). The hydration products of CA are calcium aluminate decahydrate (CAH_{10}), gibbsite (AH_3), dicalcium aluminate octahydrate (C_2AH_8), and katoite (C_3AH_6), and can be summarized in the following equations [89,90].

$$CA+10H \rightarrow CAH_{10} \quad (2.15)$$

$$2CA+11H \rightarrow C_2AH_8 + AH_3 \quad (2.16)$$

$$3CA+12H \rightarrow C_3AH_6 + 2AH_3 \quad (2.17)$$

CAH_{10} and C_2AH_8 are known to be metastable and will gradually convert to more stable phases, C_3AH_6 and AH_3, through following Equations. After conversion, the porosity of the material increases and the strength decreases [90,91]. This conversion can be accelerated by temperature and moisture available for the dissolution and re-precipitation [90,92].

$$3CAH_{10} \rightarrow C_3AH_6 + 2AH_3 + 18H \qquad (2.18)$$

$$3C_2AH_8 \rightarrow 2C_3AH_6 + AH_3 + 9H \qquad (2.19)$$

Compared to OPC, the hydration of CAC has larger heat release during early age [93]. Due to these unique features of CAC, Studies have used various techniques to characterize the early hydration of CAC [92–94], however, only limited studies have been carried out to examine the effects of TiO_2 nanoparticles on CAC hydration.

Nicolas, et al. [39] have studied the effects of adding TiO_2 nanoparticles in calcium aluminate cement on the setting time, compressive strength, conversion behavior, and the interaction of TiO_2 and hydrated phases. They found that the addition of TiO_2 results only in a slight delay in setting time but increases the compressive strength to the compressive strength above 20 MPa that all TiO_2-modified CAC samples achieve [39]. In terms of conversion behavior, they found that the conversion of CAC does not affect the photocatalytic performance and suggested the existence of long terms photocatalytic activity in CAC systems. In addition, they found that the ferrite phase in iron-rich CAC may interact with TiO_2 nanoparticles and form iron titania, mainly as pseudobrookite [39]. Although this information is useful for CAC to be used in construction applications, little information is provided on the hydration process, hydration products, and microstructural

features of TiO_2-modified CAC, as well as the dispersion of TiO_2 particles in hydrated cement, all of which are closely related to its photocatalytic performance. Therefore, Chapter 3 will provide a more comprehensive study of the effects of an addition of TiO_2 on the CAC cementitious system to address the above concerns.

CHAPTER 3. EFFECT OF TIO_2 NANOPARTICLES ON CEMENT HYDRATION AND HYDRATION PRODUCTS

3.1 Introduction

As discussed in Chapters 1 and 2, the NO_x sequestration capacity and pathways of TiO_2-modified cementitious material could be closely related to the material's hydration and hydration products. Therefore, the effects of TiO_2 additions on hydration reactions are examined in this chapter with the goal of improving our understanding of the material's hydration products and microstructural properties to facilitate more efficient design of photocatalytic cements for enhanced NO_x sequestration. Two types of cements, OPC and CAC, are used to prepare the cementitious materials. Two commercially available TiO_2 particles, one anatase and one rutile, are used to prepare the photocatalytic cementitious materials. The effects of the TiO_2 addition at various percentages by weight of cement on early age hydration are examined through isothermal calorimetry. Thermogravimetric analysis (TGA) and X-ray diffraction (XRD) are used to identify the hydration products after 28 days of curing.

3.2 Experimental program

3.2.1 Material

TiO_2-modified cementitious materials were produced by mixing TiO_2 nanoparticles with cements. OPC was obtained from Argos (Atlanta, Georgia, USA) and CAC was

obtained from Kerneos (Chesapeake, Virginia, USA). The particle size distributions (PSD) of both cements were measured in triplicate using laser diffraction in a dilute isopropanol suspension and are shown in Figure 3-1. The chemical composition of the cement was obtained by oxide analysis (ASTM C114 [95]) and is listed in Table 3-1. The X-ray diffraction (XRD) patterns of raw OPC and CAC powders are given in Figure 3-2. The mineral composition of both cements can be determined by quantitative XRD (QXRD). OPC contains 62.9% of C_2S, 7.7% of C_2S, 6.9% C_3A, and 9.2% C_4AF, and CAC contains 57.0% CA, 8.6% CA_2, 16.2% C_2AS, and 1.5% $C_{12}A_7$. Two types of TiO_2 nanoparticles were used: anatase TiO_2 (Kronos Worldwide, Dallas, Texas, USA), which is denoted as TA throughout this chapter, and rutile TiO_2 (Alfa Aesar, Ward Hill, MA, USA), which is denoted as TR. The composition, density and particle size of both TiO_2 sources according to their manufacturers are listed in Table 3-2.

Table 3-1: Chemical Compositions of OPC and CAC Cements

Cements	SiO_2	Al_2O_3	Fe_2O_3	CaO	MgO	SO_3	Na_2O	LOI
OPC	19.2	4.5	3.0	62.8	3.6	3.1	0.5	2.6
CAC	5.5	45.2	6.9	37.7	0.2	0.1	0.3	1.9

Table 3-2: Characteristics of TiO_2 particles (provided by manufacturer)

Material	Phase	TiO_2 content (%)	Specific Density (g cm^{-3})	Particle Size (μm)
TA	Anatase	>85.0	3.9	Approx. 0.015
TR	Rutile	>99.8	4.2	0.9 to1.6

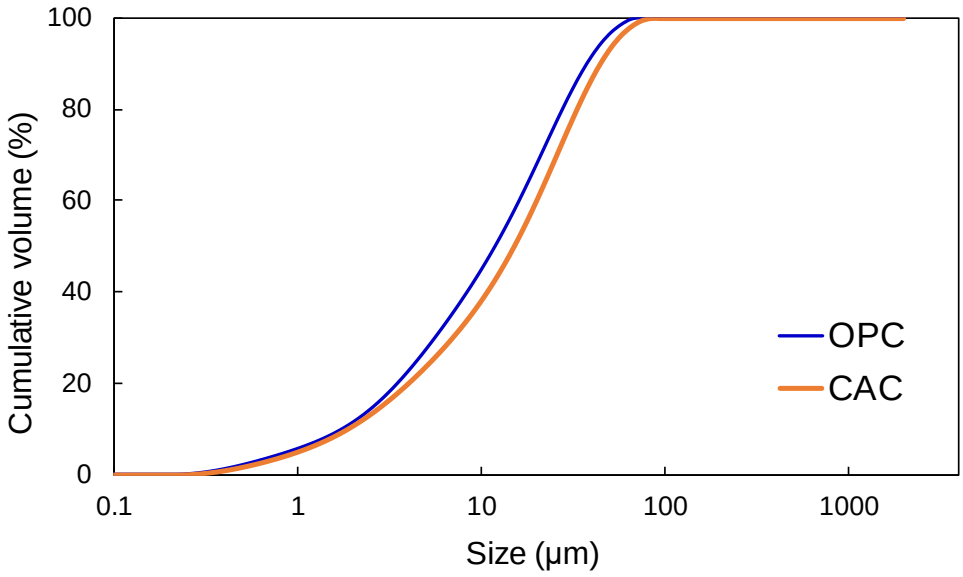

Figure 3-1: Particle size distribution of OPC and CAC with d_{50} of approximately 12 μm and 15 μm, repsectively

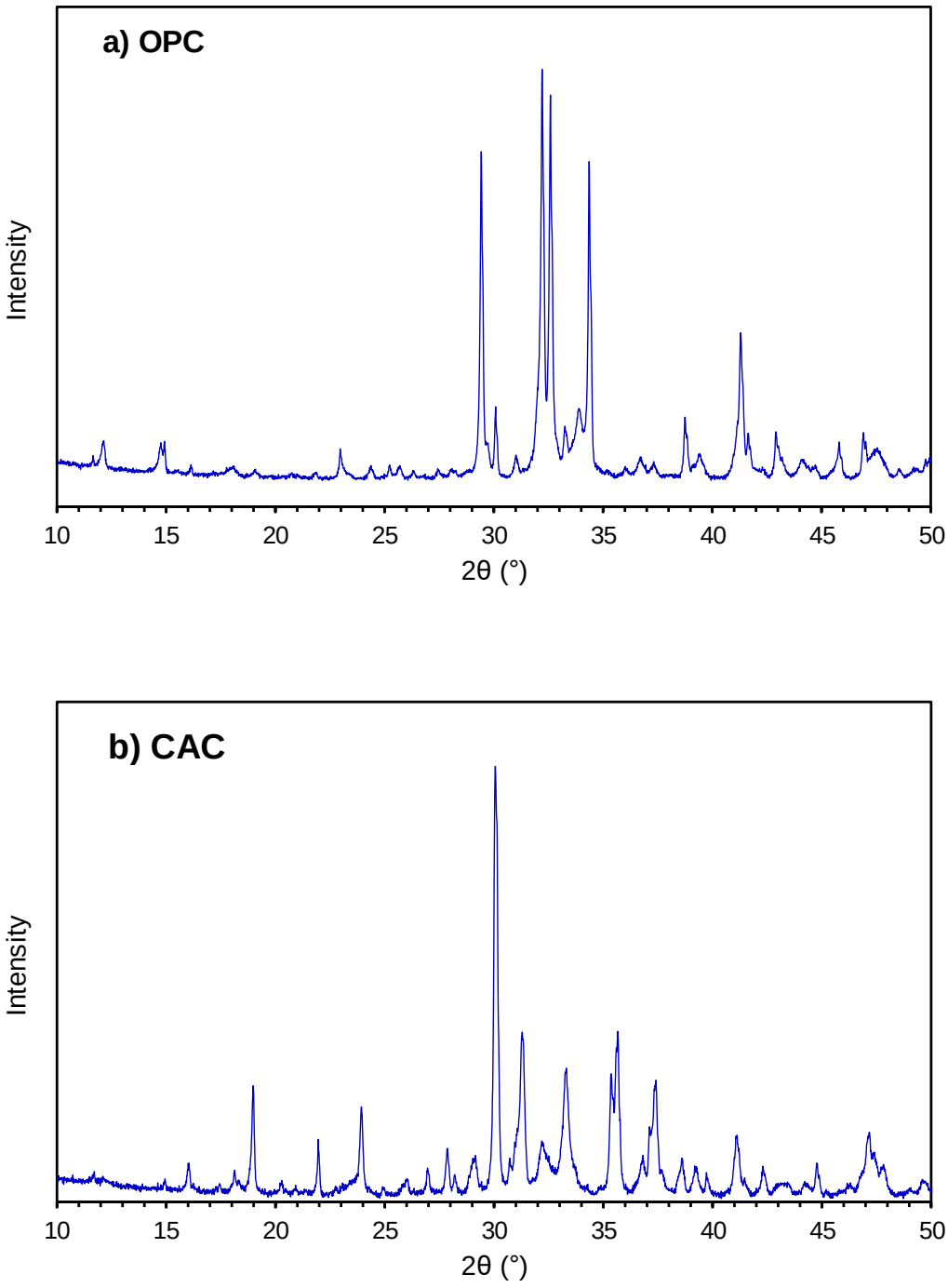

Figure 3-2: XRD patterns of raw OPC and CAC cement powders

The XRD analysis in Figure 3-3 shows TA has an amorphous morphology while TR is crystalline. The amorphous morphology of TA should be attributed to its high impurity, as specified by manufacturer (Table 3-2). Examination of both types of TiO_2 particles by scanning electron microscopy (SEM) reveals that TA consists of agglomerations of nanoparticles with a size of about 1-1.5 μm while TR appears to be crystalline particles of similar size (Figure 3-4). Since the nano-sized TiO_2 particles tend to agglomerate, additional characterization is recommended when including these TiO_2 nanoparticles in cementitious materials.

The amorphous morphology of TA is likely due to impurities, which often result from the surface coating of TiO_2 particles designed for particle dispersion. To detect and quantify the presence of the ions that are coated on the surface of TA nanoparticles, both energy-dispersive X-ray spectroscopy (EDS) and ion chromatography (IC, Dionex) measurements were performed. The IC is equipped with an Ionpac® AS14A column (4×250 mm) combined with an Ionpac® AG14A guard column (4×50 mm) and a Dionex ED40 electrochemical detector. The mobile phase contained 8 mM Na_2CO_3 and 1 mM $NaHCO_3$, and the flow rate was 0.8 mL/min. TiO_2 particles were suspended in deionized water (18MΩ·cm) with four different solid to liquid ratios: 1g, 2g, 4g, and 8g of TA particles to 1 liter of water. The extraction time of 1 minute was selected to mimic sample preparation, the details of which are provided in Section 3.2.2. Triplicate samples were produced for each ratio. The detected results are used to extrapolate the concentration of detected ions in different TiO_2-modified cementitious materials (Section 3.3.1).

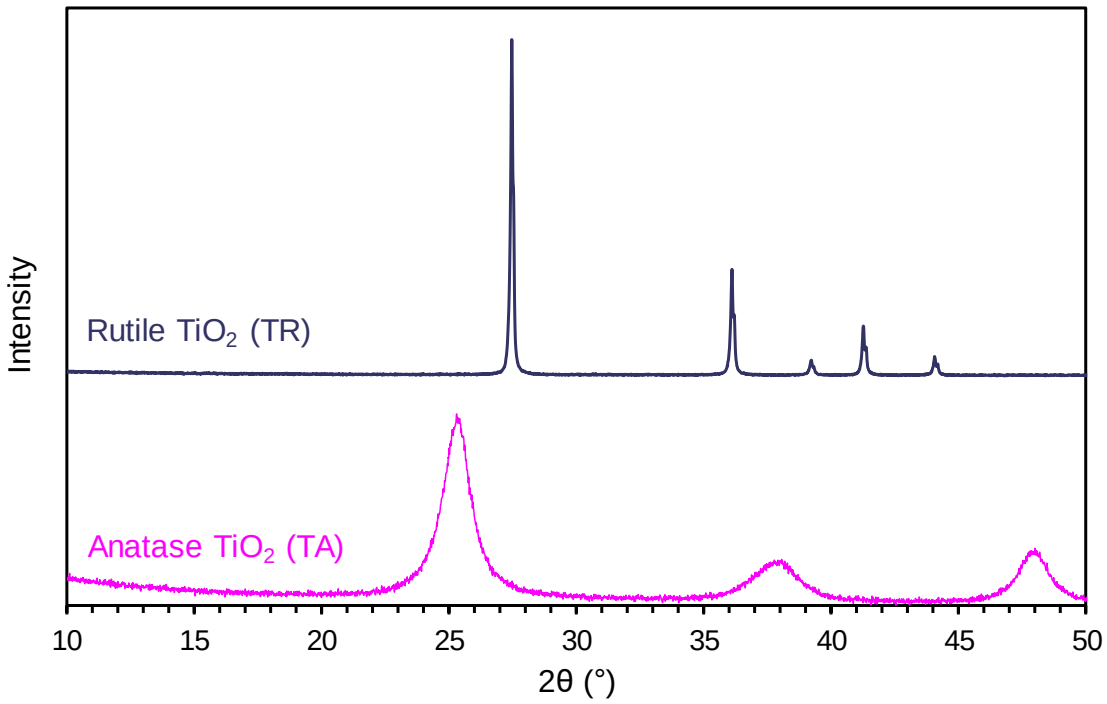

Figure 3-3: XRD showing an amorphous morphology of anatase TiO_2 (TA) and a crystalline morphology of rutile TiO_2 (TR)

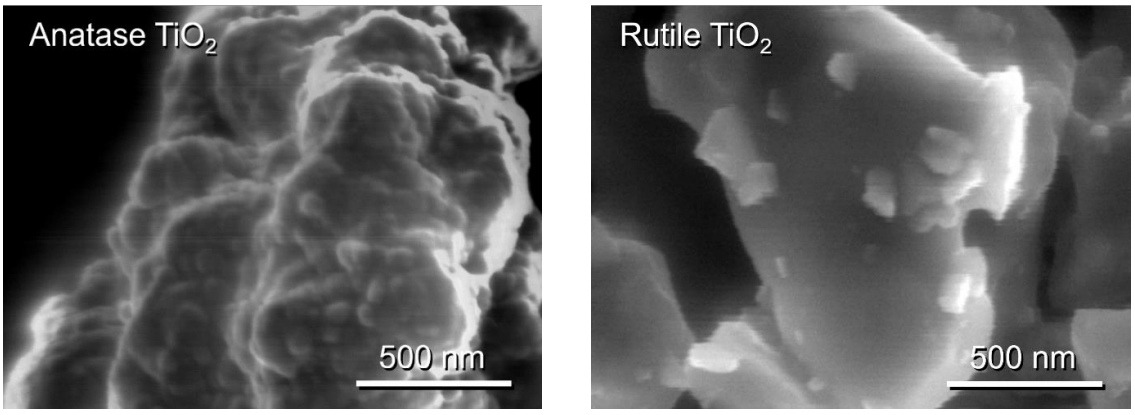

Figure 3-4: Particle features and morphologies of anatase TiO_2 (TA) and rutile TiO_2 (TR)

3.2.2 Sample preparation

For the TiO_2-doped cementitious materials, the water-to-cement (w/c) ratio was kept at 0.40 with TiO_2 additions of 0% (control), 5%, and 10% by the mass of cement content. The selected fractions of TiO_2 have also been adopted in previous studies to examine the effects of TiO_2 on cement hydration [62,88,96]. The TiO_2 particles were first added to deionized water (18.2 MΩ-cm) and mixed for 1 minute using a handheld electric mixer to facilitate dispersion. The CAC was then added to the TiO_2 suspension and mixed for an additional 2 minutes. Five (5.00±0.01) grams of paste was then placed into capsules for isothermal calorimetry to examine the early hydration properties. The rest of the material was stored in double-sealed plastic bags to avoid drying or carbonation. The materials were cured at 23 ± 1°C for 28 days prior to TGA, XRD, and SEM analysis. Detailed descriptions of each characterization method are provided in the following section. Calorimetry, TGA, and XRD were conducted in triplicate.

3.2.3 Characterization studies

Isothermal calorimetry was performed to study the material's early-age hydration kinetics. The test was in accordance with ASTM C1679 [97]. The time at which cement is added to the water (for control samples) or the TiO_2 suspension is considered the starting time of the reaction for each sample. Samples were transferred to capsules and placed inside an eight-channel microcalorimeter (TAM AIR, TA instruments, New Castle, Delaware), which has a precision of ±2 μW and an accuracy greater than 95%, within 5 minutes of the addition of cement. The data from the initial 45 minutes were disregarded

because this period was only used to ensure the thermal equilibrium was reached between the capsule and the calorimeter. The rate of hydration was measured as heat release (mW) every 60 seconds and normalized per gram of cement included in the sample. The rate of heat evolution and the cumulative heat released were measured for the first 7 days of hydration.

For XRD analysis, approximately 2 grams of cement pastes were ground to < 74 um (No.200 sieve) and packed into sample holders. The samples were then placed into a PANalytical Empyrean X-ray diffractometer and excited with Cu-Kα (λ = 1.54 Å) radiation. Scans were performed at 2θ of between 10° and 70°, using a PIXcel3D detector and a sampling time of 30 seconds. Although XRD was able to detect the main hydration products of cements, it may not detect amorphous phases. Therefore, TGA was carried out to identify hydration phases and quantify bound water (Hitachi TG/DTA 7300). Approximately 60 mg of cement pastes were ground to the same particle size of <74 μm and placed in a 70 μL platinum crucible. Samples were dried at 40 ºC for 15 minutes or until reaching constant mass if mass had not stabilized within 15 minutes. The sample was then heated from 40 ºC to 1000 ºC at a rate of 10 ºC min^{-1}. Nitrogen was used to purge with a flow rate of 100 mL min^{-1}.

3.3 Results and discussion

The characterization of anatase TiO_2 (TA), which is examined by EDS and IC, is presented first. The examination of effects of TiO_2 addition on OPC and CAC will be presented separately in this chapter and each section contains the results of following characterization studies. The isothermal calorimetry was used to examine the early age

hydration. TGA and XRD are used to identify the hydration products. SEM are used to make a direct observation of the microstructural features and the dispersion of TiO_2 particles in hydrated cement.

3.3.1 Characterization of TiO_2

Based on the EDS analysis, sulfur ions were detected on the surface of TA. This result was confirmed by IC analysis, which detected sulfate at a concentration of 1.96 ± 0.09 mmol/L. The presence of sulfate is expected because prior studies have shown that sulfates are present on the surface of TiO_2 nanoparticle for facilitating particle dispersion. Sulfates have been used as common inorganic hydration retarding admixtures and they help form protective layers of low soluble calcium salts on the surface of cement grains by adding anions such as sulfate, carbonate, and phosphate, thereby limiting the rate of early dissolution and hydration [98]. In cement hydration, sulfates are known for effectively slowing down the hydration of aluminate phases to avoid the rapid setting behavior that is undesirable in cement-based concrete [98]. Based on the mix design provided in Section 3.2.2, the samples with the 5% and 10% addition of TiO_2 by the mass of cement introduces approximately sulfate ions at an approximate proportion of 1% and 2% of cement mass, respectively.

3.3.2 Characterization of TiO_2-modified OPC

3.3.2.1 *Early age hydration*

Figure 3-5 shows the rate of hydration per gram of cement for TA-modified and TR-modified OPC pastes, respectively, for the first 50 hours after mixing. The corresponding cumulative heat data of OPC samples for the first 50 hours is shown in Figure 3-6. Similar trends were observed in both TA- modified and TR-modified OPCs, which show an increase in the maximum rate of heat (or the greatest power evolved with time) where maximum rate peaks are accelerated by about 1 hour in samples with 5% TiO_2 addition and 2 hours with 10% TiO_2 addition (Figure 3-5). The results also show that more TiO_2 results in a greater increase in the maximum rate of heat. Due to the acceleration, the cumulative energy release also increases in TiO_2-modified OPC, as shown in Figure 3-6. As discussed by Jayapalan et al. [62], the addition of TiO_2 to cement paste could result in two effects on cement hydration: heterogeneous nucleation and growth effect and dilution effect. The nucleation and growth effects promote cement hydration hence the rate of hydration of OPC and the total heat evolved increases with increased dosage of TiO_2. The dilution effect is attributed to the addition of TiO_2; therefore, the hydration heat rate and total heat evolution decrease with increased dosage of TiO_2. The results found in this study indicate that heterogeneous nucleation and growth effects are more dominant than dilution effect, hence increase the hydration heat rate and total heat evolution, which also agree with Jayapalan et al. [62].

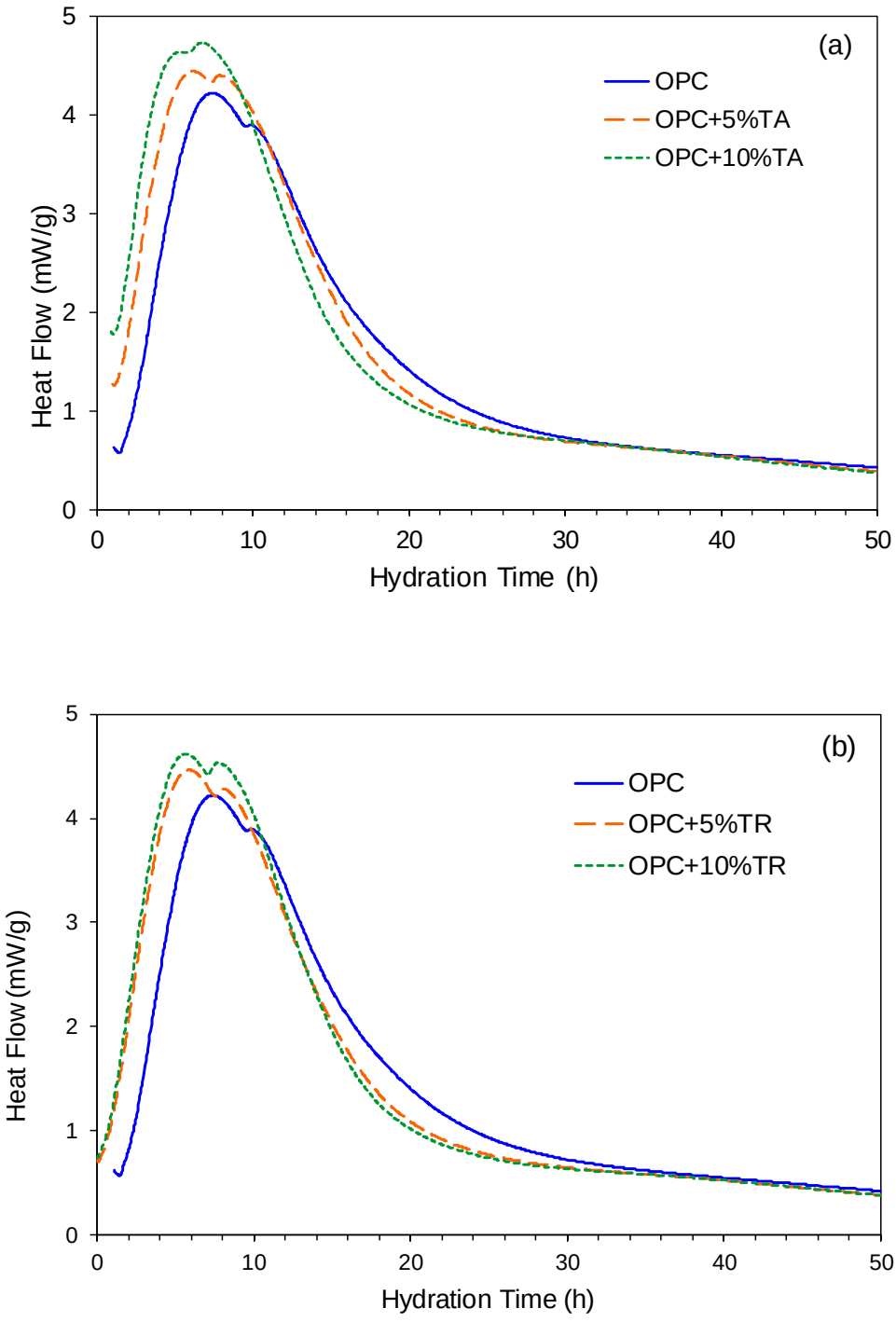

Figure 3-5: Hydration rate of (a) TA-modified and (b) TR-modified OPC pastes. The results are normalized by the amount of cement

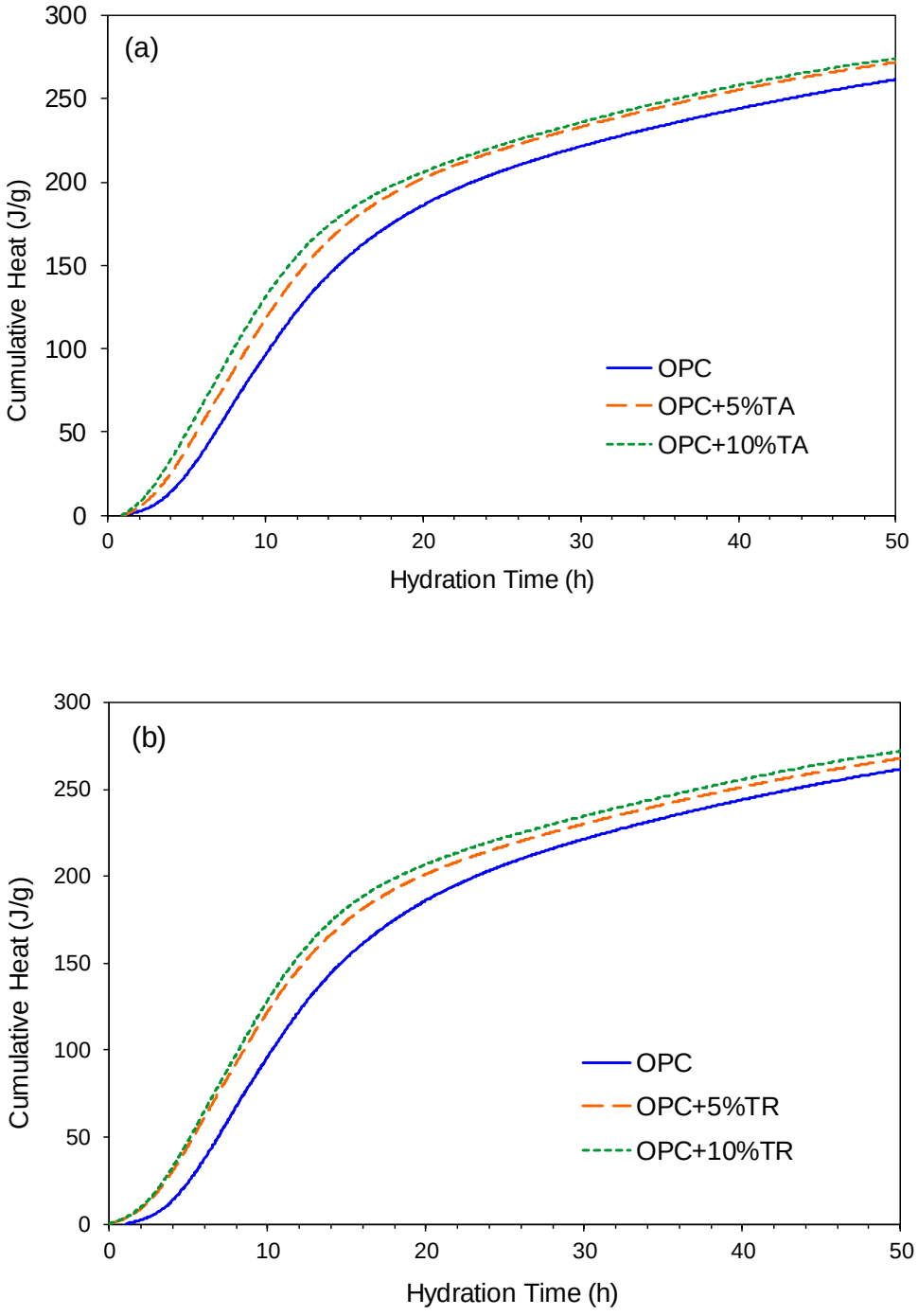

Figure 3-6: Cumulative heat of hydration of (a) TA-modified and (b) TR-modified OPC pastes. The results are normalized by the amount of cement

3.3.2.2 Hydration products after 28-day curing

Figure 3-7 shows the TGA results obtained for ordinary OPC as well as the 5% and 10% TiO_2-modified OPC pastes after 28 days of curing. The phases identified by TGA are C-S-H, ettringite, AFm, portlandite, and calcite. The occurrence of calcite should be attributed to a small portion of limestone that is contained in OPC cement. The TGA results for all samples are all aligned with each other, suggesting similar amounts of hydration products formed after 28 days of curing despite that the acceleration of early age hydration in TiO_2-modified OPC pastes. This result is further supported by XRD analysis (Figure 3-8), showing almost identical XRD patterns for all OPC pastes. The only difference among these XRD patterns is the presence of a TiO_2 peak (Figure 3-8). Therefore, the accelerated early age hydration of OPC associated with the TiO_2 addition does not affect the phase composition or proportionality of the resultant OPC samples after 28 days curing. These results can provide additional information when analyzing the photocatalytic performance of TiO_2-modified OPC samples and the relationship with the phase composition-associated microstructural features.

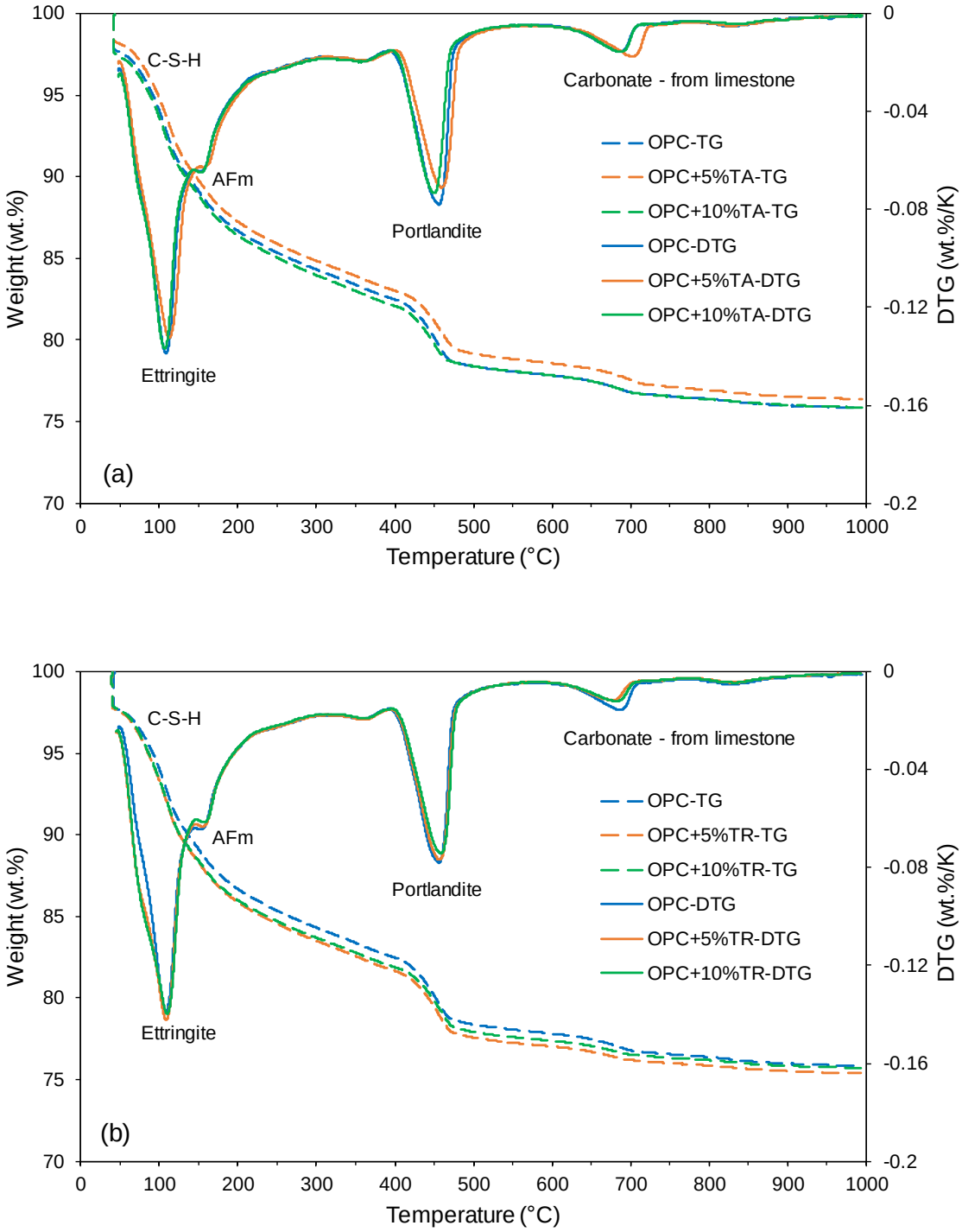

Figure 3-7: TGA results of (a) TA-modified and (b) TR-modified OPC pastes.

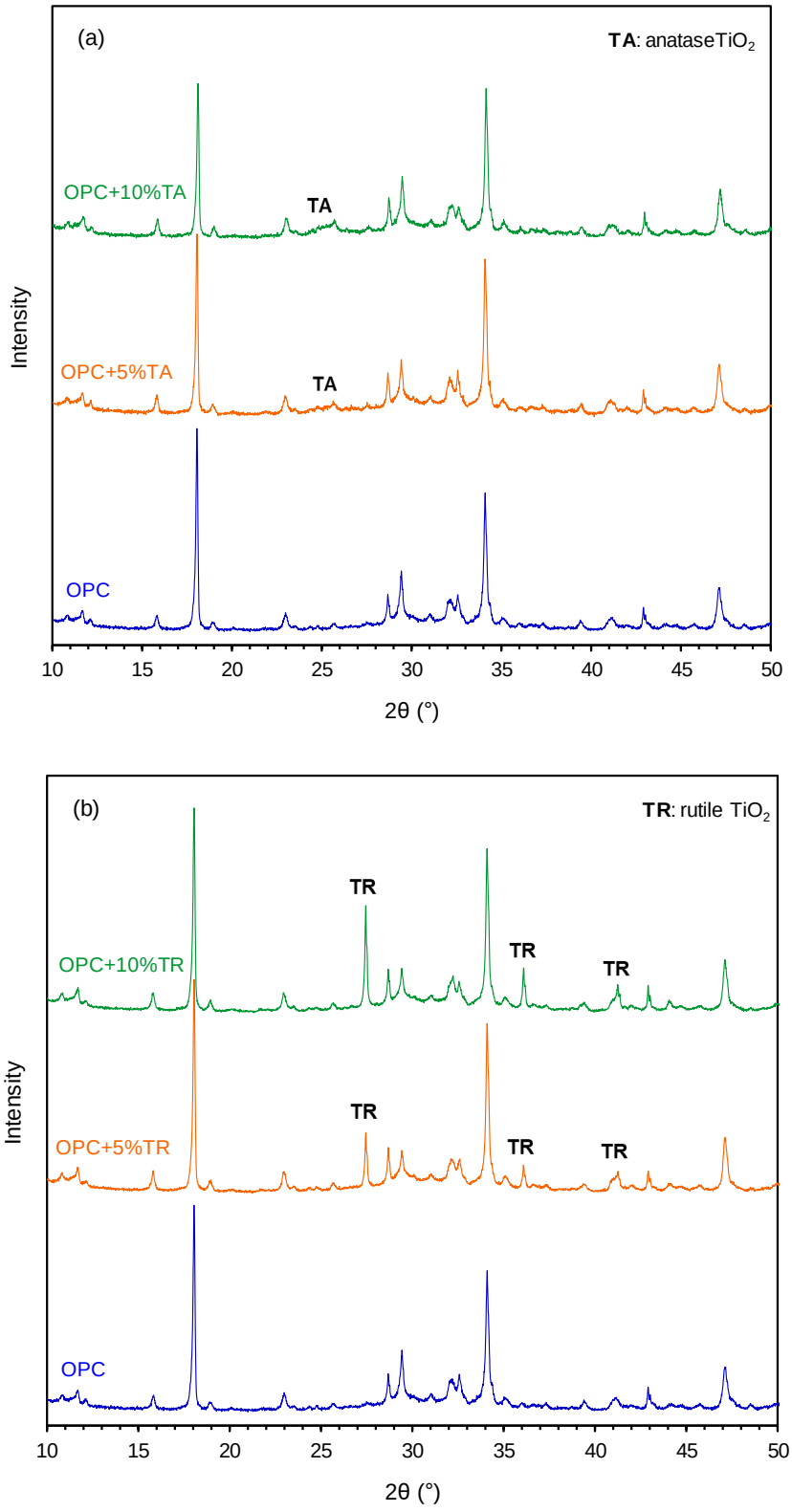

Figure 3-8: XRD patterns of (a) TA-modified and (b) TR-modified OPC pastes after 28 days of hydration

3.3.3 Characterization of TiO_2-modified CAC

3.3.3.1 Early age hydration

Figure 3-9 shows the rate of hydration per gram of cement for TA-modified and TR-modified CAC pastes, respectively, for the first 40 hours after mixing. The corresponding cumulative heat data for the first 50 hours is shown in Figure 3-10. Unlike OPC samples, the maximum rate of heat of TA-modified CAC decreases and the early age hydration is retarded, while the maximum rate of TR-modified CAC heat still decreases but the early age hydration is accelerated.

For TA-modified CAC, the maximum rate of heat decreases with additional TA dosage. Compared to plain CAC, an approximately 15% decrease of the maximum rate is observed with 5% addition of TA by mass and an approximately 30% decrease with 10% addition of TA by mass. These decreases also result in a lower cumulative rate of heat evolution during the first 50 hours, as shown in Fig 3-10(a). Similar results are observed in TR-modified CAC where an approximately 10% decrease of maximum rate is observed for both 5% and 10% addition of TR by mass (Figure 3-10(b)). In terms of cumulative rate of heat evolution (Figure 3-10(b)), a crossover occurs at around 15 hours, when the rate for 10% TR-modified CAC decreases below that of plain and 5% TR-modified CAC samples. This also corresponds to the time when the rate of heat evolution begins to slow, as shown in Figure 3-10(b). Recall that the cement content and water-to-cement ratio remain constant and the TiO_2 are additionally introduced to the system. This action of adding TiO_2 results in a lower the water-to-solid ratio for TiO_2-modified CAC, suggesting the lower maximum rate of heat that are observed in these samples could be due to the limited amounts of water

available for hydration. However, the effect of amount of water on the hydration of TiO_2-doped CAC requires further investigation.

For TA-modified CAC, the early age hydration is retarded. When examining the time at which the maximum rate peak occurs, it is delayed by about 1 hour for 5% TA-modified CAC and 5 hours for 10% TA-modified CAC, as shown in Figure 3-9(a). This delay is also reflected in the cumulative rate of heat evolution, whereby the rate of energy evolution further retards compared to plain CAC (Figure 3-10(a)). In contrast, the opposite behavior is observed in TR-modified CAC, where the early age hydration is accelerated. The maximum rate peak occurs about 1 hour and 2 hour earlier for 5% and 10% TR-modified CAC than plain CAC samples, respectively (Figure 3-9(b)). This acceleration of early age hydration could also be due to nucleation and growth effects introduced by TiO_2 addition, as observed in TiO_2-modified OPC in Section 3.3.2. However, this acceleration increases only the rate of energy evolution during first 15 hours, as reflected in the cumulative heat of hydration (Figure 3-10(b)). After the first 15-hour period, the rate of energy evolution slows down and the cumulative heat of hydration reaches a lower value than plain CAC samples. This phenomenon of early age acceleration and late age deceleration in cumulative heat of hydration has also been observed previously by other researchers [99].

The apparent initial retardation effect of TA on CAC hydration extends the induction period [100], which is contradictory to the effects of the TR-modified CAC in this study or the TA-modified OPC from Section 3.3.2. Therefore, this retardation effect warrants a further investigation to understand its cause.

According to the manufacturer's data in Section 3.2.1, the TA used in this study have about 15% impurity. Based on the EDS and IC analyses (Section 3.3.1), this impurity contains sulfate with a measured concentration of approximately 2 mmol L^{-1}. The mixing procedure used in this study specified that TA was first added to water and mixed for 1 minute before adding CAC cement. In this way, sulfate ions had already been introduced to the TiO_2 suspension prior to contact between CAC and water. Therefore, it is hypothesized that the retardation phenomenon in TA-modified CAC samples is related to the presence of sulfate ions, which overwhelm the nucleation and growth effects induced by TiO_2 additions, resulting a net deceleration of CAC hydration. Future studies are needed to confirm the effects of sulfate ions on retarding CAC hydration, as well as discern the relative importance of these two effects.

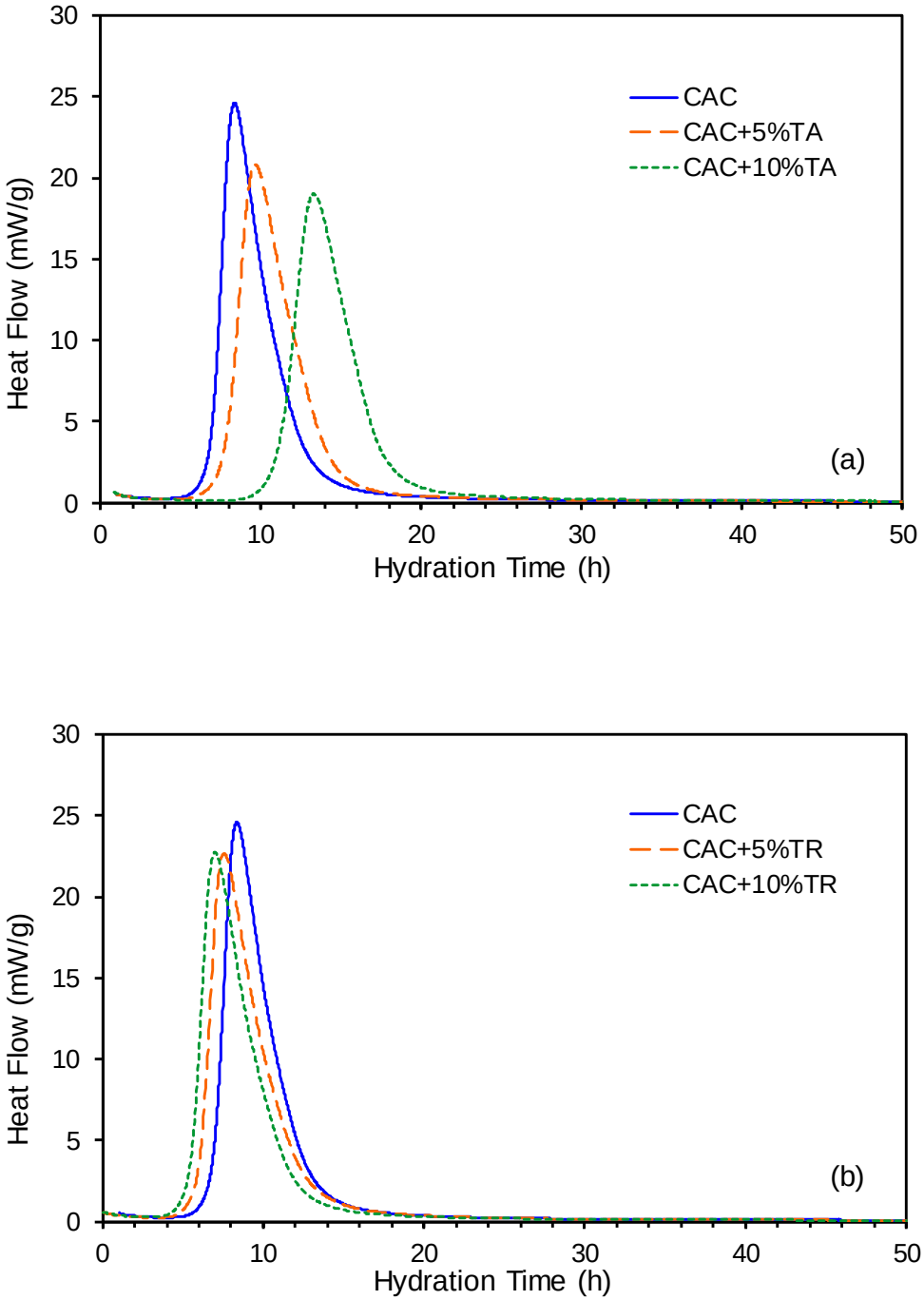

Figure 3-9: Hydration rate of (a) TA-modified and (b) TR-modified CAC pastes. The results are normalized by the amount of cement.

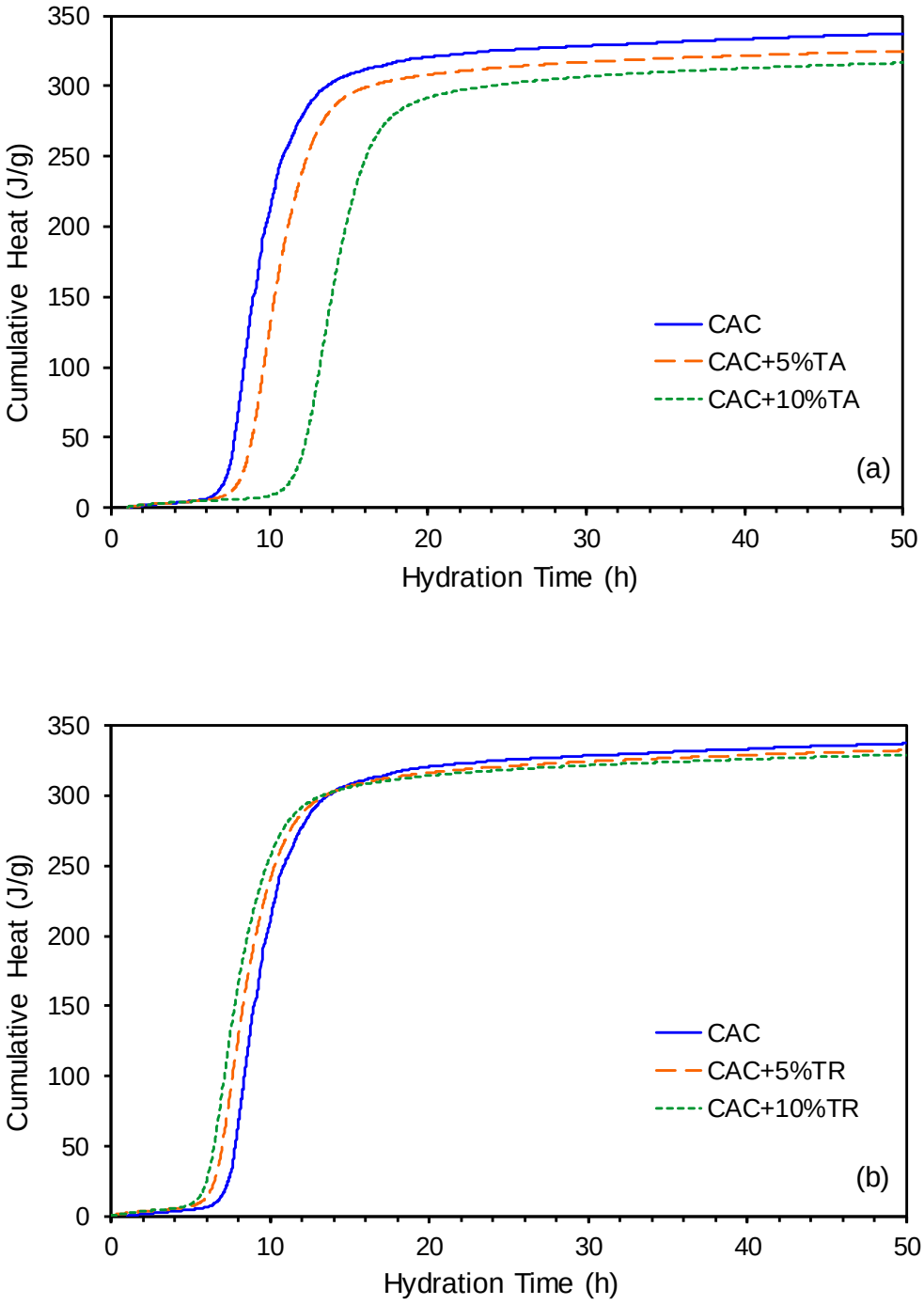

Figure 3-10: Cumulative heat of hydration of (a) TA-modified and (b) TR-modified CAC pastes. The results are normalized by the amount of cement and the crossover point occurs at 15 hour.

3.3.3.2 Hydration products after 28-day curing

Figure 3-11 shows the XRD patterns obtained for plain CAC samples as well as the 5% and 10% TiO_2-modified CAC pastes after 28 days of curing. For the plain CAC pastes, the XRD pattern shows the hydration products of the metastable phases of CAH_{10}[1] and the stable phases of AH_3 and C_3AH_6. Some unreacted CA and CA_2 phases are also detected. The XRD results agree with the TGA analysis (Figure 3-12), where the weight losses indicate decomposition of CAH_{10} phases at 120°C, C_2AH_8 phases at 150°C, AH_3 phases at 270°C, and C_3AH_6 phases at 320°C [101].

For TA-modified CAC, the paste with a 5% TiO_2 addition has a similar phase composition as plain CAC, with a slightly lower intensity in XRD pattern that indicates a slightly low degree of hydration due to the dilution and retardation effects (Section 3.3.3.1). For TR-modified CAC, the pastes with both a 5% and 10% addition of TiO_2 exhibit similar XRD patterns as the plain CAC paste (Figure 3-11(b)) despite the accelerated early age hydration of the cement apparent in Figure 3-10(b). TGA results (Figure 3-12 (b)) also show similar weight losses among these three pastes, indicating a similar formation of hydrated phases. Therefore, the early age hydration of CAC associated with the TiO_2 addition does not affect phase composition or proportionality after 28 days of curing for previously mentioned CAC samples, which are similar to the results observed in OPC samples.

[1] The XRD peak of another metastable phase, C_2AH_8, is located at $2\theta < 10$, which is outside the range of the XRD analysis in this study. However, the presence of such phase has been confirmed by the TGA analysis.

However, pastes with a 10% TiO_2 addition show distinctly different phase compositions, where the peak intensity of the stable phases of AH_3 and C_3AH_6 are significantly higher than both the plain and 5% TA-modified CAC pastes (Figure 3-11(a)). This finding is also supported by TGA results (Figure 3-12(a)), where the metastable phases of CAH_{10} and C_2AH_8 significantly decrease while the stable phases of AH_3 and C_3AH_6 significantly increase compared to the other two CAC pastes. The comparison between 5% and 10% TA-modified CAC pastes suggests that the excessive amount of sulfate ions present in the 10% TiO_2-modified CAC pastes could lead to a larger formation of stable phases during the 28 days of hydration than other CAC pastes. Such formation of stable phases could also be related to the pre-existing sulfate ions in TiO_2 suspension. However, to determine the exact period of the formation of these stable phases and understand the underlying mechanism of CAC hydration in the presence of sulfate, future studies should prepare and analyze CAC pastes with different ages of hydration.

In addition, sulfates are known to participate in reactions that promote the formation of AFm or AFt phases in CAC [92]. However, these sulfate-bearing phases did not form in this study according to TGA and XRD results. That could be due to the low concentration of sulfate ions introduced to the system. Even though such low dosage of sulfate ions could be enough to affect the early age hydration and formation of hydration products in CAC systems, they might not be able to form significant amounts of sulfate-bearing hydrated phases that can be detected by XRD or TGA. Again, it is necessary to examine the effects of pre-existing sulfate on CAC hydration in a future study.

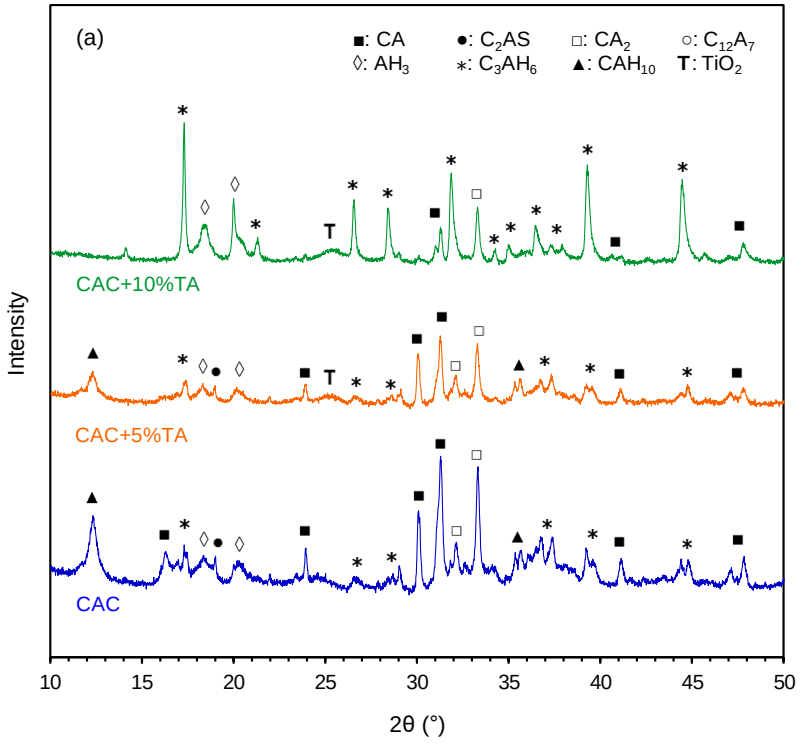
(a)
■: CA
●: C2AS
□: CA2
○: C12A7
◊: AH3
∗: C3AH6
▲: CAH10
T: TiO2
CAC+10%TA
CAC+5%TA
CAC
Intensity
10
15
20
25
30
35
40
45
50
2θ (°)

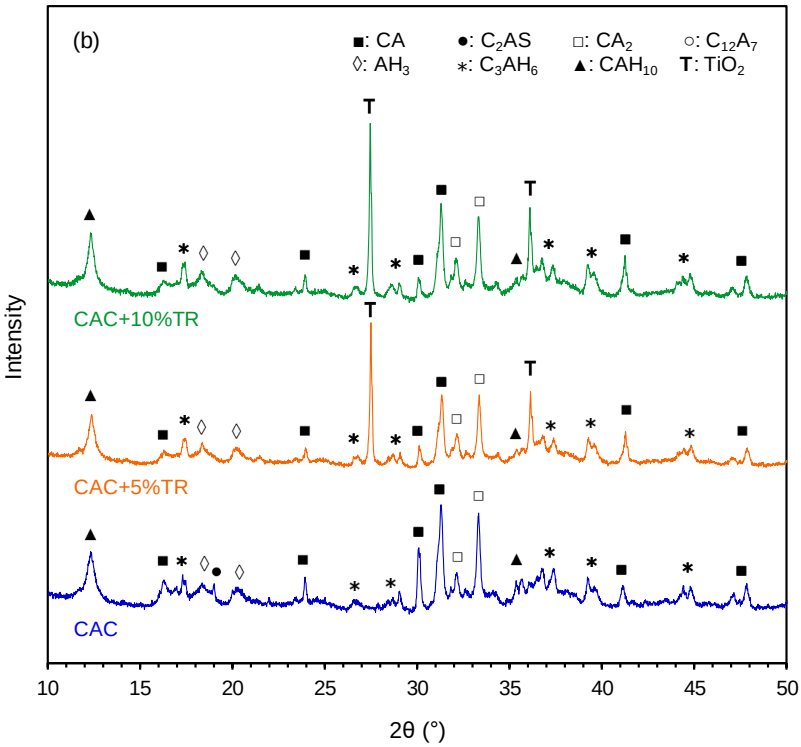
(b)
■: CA
●: C2AS
□: CA2
○: C12A7
◊: AH3
∗: C3AH6
▲: CAH10
T: TiO2
CAC+10%TR
CAC+5%TR
CAC
Intensity
10
15
20
25
30
35
40
45
50
2θ (°)

Figure 3-11: XRD patterns of (a) TA-modified CAC pastes and (b) TR-modified CAC pastes after 28 days of hydration.

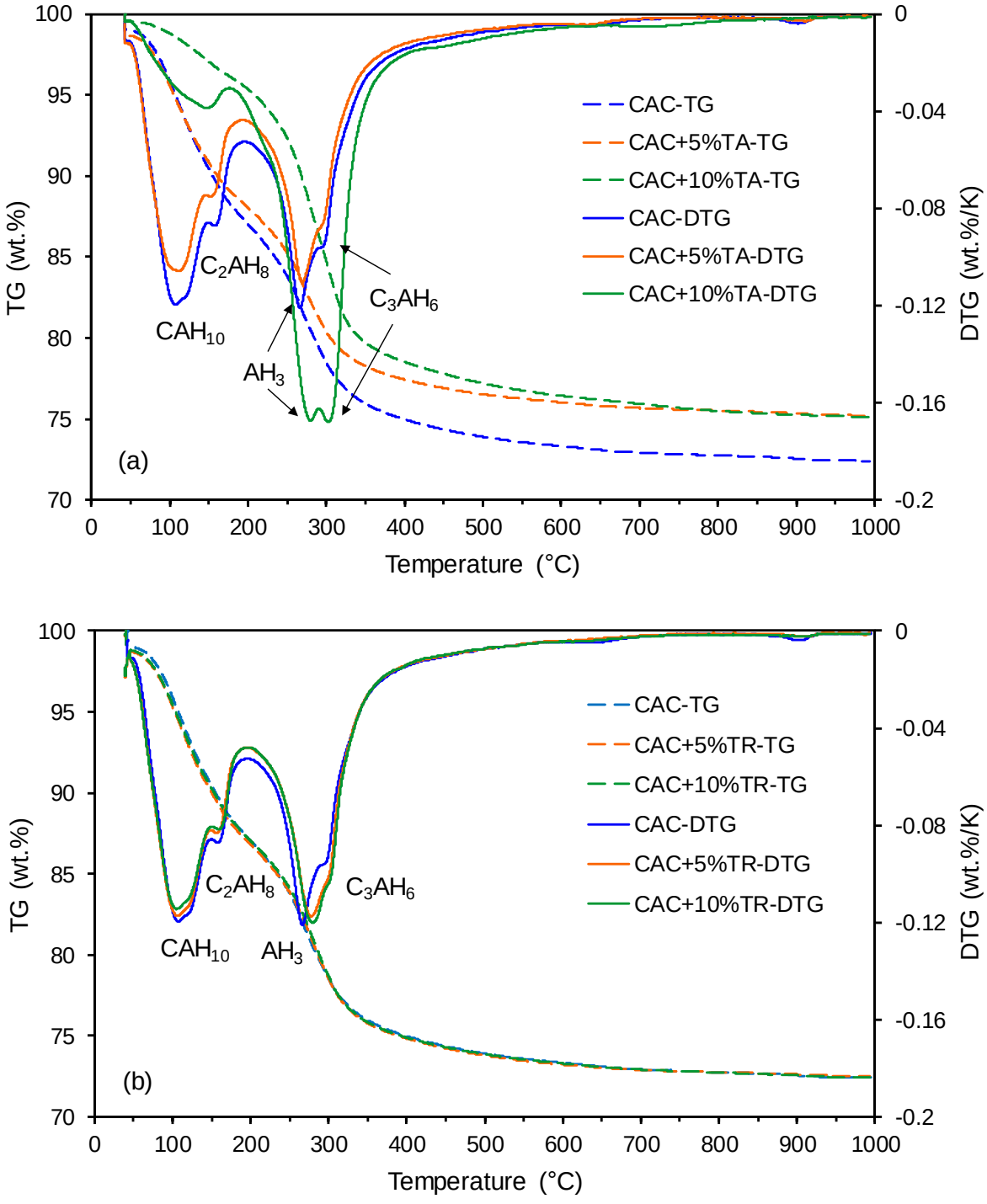

Figure 3-12: TGA results of (a) TA-modified CAC pastes and (b) TR-modified CAC pastes after 28 days of hydration. Conversion has occurred in 10% TA-modified CAC.

3.4 Conclusions

This chapter demonstrated that the TiO_2 additions have different effects on the hydration of OPC and CAC products. The results of TiO_2-modified OPC samples are in accordance with expectations from previous work. The results of TiO_2-modified CAC samples are different from OPC samples. Two commercially available TiO_2 materials, anatase (TA) and rutile (TR), were used to prepare the TiO_2-modified cementitious materials. The characterization of these properties allows for a better understanding of the photocatalytic performances of these materials (Chapter 4). A combination of isothermal calorimetry, TGA, and XRD analyses were used to examine the early age hydration rate and to identify the hydration products after curing for 28 days.

For OPC samples, the inclusion of TiO_2 provided additional nucleation sites for the formation of hydration products, resulting in an accelerated hydration reaction. This phenomenon has been previously observed by other researchers [40]. However, after 28 days of curing, both TGA and XRD analyses show a similar hydration pattern among plain, 5% TiO_2-modified, and 10% TiO_2-modified OPC samples, indicating the accelerated early age hydration does not affect the ultimate hydrated cementitious phase composition or proportionality in these materials. This information provides insight into characterization and quantification of these materials' photocatalytic performances, which is explored in Chapter 4 and Chapter 6.

For CAC samples, the inclusion of TiO_2 reduces the maximum rate of heat evolution compared to OPC samples, suggesting lesser amount of water are available for CAC hydration since TiO_2 addition decreases the water:solid ratio. An accelerated hydration

reaction was observed in TR-modified CAC samples. This acceleration should be due to the nucleation and growth effects that are also demonstrated in OPC samples. The reduction of maximum heat rate and the acceleration of the hydration in TR-modified CAC results in a phenomenon, which higher cumulative heat of hydration was observed in TR-modified CAC than plain CAC before 15 hours and lower value was observed aftewards. In contrast, a retardation in hydration was observed in TA-modified CAC samples. As a result, the cumulative heat of hydration was delayed compared to plain CAC samples. This phenomenon could be due to the presence of sulfate ions on the surface of TA particles, whose retardation effects overwhelm the nucleation and growth effects induced by the TiO_2 additions, resulting in a net deceleration of CAC hydration.

Both 5% and 10% TR-modified CAC samples and 5% TA-modified samples show similar XRD patterns and TGA results as plain CAC samples, suggesting that the early age hydration associated with the TiO_2 addition has insignificant effects on cementitious phase composition or proportionality. However, the 10% TA-modified samples show many distinctive XRD patterns and TGA results, where a larger formation of stable hydrated phases of AH_3 and C_3AH_6 were observed. It is hypothesized that such phenomenon are related to the excessive amount of sulfate ions introduced by a 10% TA addition, but the underlying mechanism of such phenomenon and its correlation with a retardation effect are worthy of a future study.

CHAPTER 4. PHOTOCATALYTIC PERFORMANCE OF TiO_2-DOPED CEMENTITIOUS MATERIALS

4.1 Introduction

As discussed in Chapter 2, NO_x causes a wide variety of health and environmental problems, such as the impairment of the human respiratory and visual systems and the formation of tropospheric ozone and urban smog. This chapter aims to examine the photocatalytic performance of TiO_2-doped cementitious materials in terms of NO_x photodegradation. The dispersion of TiO_2 nanoparticles and their association with cementitious phases are also examined in this chapter because such information is important to evaluate the consistency of the material's photocatalytic performance. The anatase TiO_2 (denoted as TA in Chapter 3) is selected to make the photocatalytic cementitious material since its photocatalytic properties can be activated under UV light. In addition, previous studies have demonstrated that adding TiO_2 nanoparticles at more than 5% by weight does not significantly increase the photocatalytic efficiency [39,52,102] but substantially increases the material's embodied energy [63]. Therefore, the anatase TiO_2 nanoparticles are added at a level of 5% in samples used in this chapter and the rest of the dissertation, which examine photocatalytic performance.

Both TiO_2-doped OPC and CAC cementitious materials are examined in this chapter. The NO_x photodegradation is performed using the standardized test methods described in Chapter 2. Long-term photocatalytic performance is evaluated by carrying out multi-cycle NO_x photodegradation tests, the details of which will be elaborated in the following section.

The photocatalytic efficiency and capacity are determined based on the results of long-term NO_x photodegradation. The dispersion of TiO_2 nanoparticles and their association with cementitious phases are examined by Scanning Electron Microscope (SEM) coupled with energy-dispersive X-ray spectroscopy (EDS).

4.2 Experimental program

4.2.1 Materials

The TiO_2-doped OPC and CAC cementitious materials were prepared from ASTM C150 Type I/II OPC (Argos, Atlanta, Georgia, USA) and CAC (Kerneos, Chesapeake, VA, USA), respectively, combined with 5 wt% replacement of TiO_2 photocatalysts that are optimized under UV irradiance of 10 Wm^{-2} (KRONOClean® 7050, Kronos Worldwide). The water-to-solid ratio was kept constant at 0.40. The chemical compositions of both cements, obtained from the methods described in Chapter 3, are listed in Table 4-1 and the characteristics of the anatase TiO_2 are listed in Table 4-2. The mineral phase composition can be found in Section 3.2.1.

Table 4-1: Chemical Compositions of OPC and CAC Cements

Cements	SiO_2	Al_2O_3	Fe_2O_3	CaO	MgO	SO_3	Na_2O	LOI
OPC	19.2	4.5	3	62.8	3.6	3.1	0.5	2.6
CAC	5.5	45.2	6.9	37.7	0.2	0.07	0.26	1.9

Table 4-2: Characteristics of TiO_2 photocatalyst (provided by manufacturer).

TiO_2 content	Phase	Density	Bulk Density	Specific Surface Area
>85%	Anatase	3.9 g cm^{-3}	300 g L^{-1}	>225 m^2 g^{-1}

4.2.2 Sample preparation

The sample preparation technique was adopted from Chapter 3. TiO_2 photocatalysts were first added to deionized water (18.2 MΩ-cm) and the suspension was mixed for 1 minute using a handheld electric mixer to facilitate particle dispersion. Cement was then added to the TiO_2 suspension and mixed for 2 minutes. Plate samples with dimensions of 50.8 × 50.8 × 9.5 mm^3 (width × length × height) were cast in plastic molds against a smooth surface. They were then stored at 23 ± 2 ℃ in a double sealed bag to maintain a high humidity and avoid potential carbonation. After 24 hours, the plates were removed from the molds and subsequently cured in limewater at 23 ± 2 ℃ for 28 days in a sealed condition. After curing, the plate samples were conditioned at 23 ± 2 °C and 50 ± 5% relative humidity until reaching constant mass (less than 0.5 wt% change over a 6-hour period). All samples were then stored in double sealed plastic bags prior to NO_x photodegradation tests and SEM analysis to avoid carbonation or drying.

4.2.3 NO_x photodegradation test setup

Figure 4-1 shows the test setup of the NO_x photodegradation. The test procedure follows ISO 22197 [46] and JIS R 1701 Standards [47]. Three identical plate samples together with a total area of 7500 mm^2 were placed in a reaction chamber with a borosilicate cover. As recommended by the aforementioned standards, the NO_x gas used in this study was 1000 ppb nitric oxide in ultrapure dry air and at a constant flow rate of 1 L min^{-1}. The reaction was conducted at 23 ± 2 °C and 50 ± 5 % relative humidity. The sample-loaded chamber was placed under two UV fluorescent lamps of 40 W with peak emission of 365 nm (Damar Worldwide, Aurora, MO, USA). To achieve an optimal photocatalytic performance, the UV intensity at the sample surface was maintained at 10 Wm^{-2} by adjusting the distance between the UV light source and the samples, as shown in Figure 4-1. The initial gas concentration was kept at 1000 ppb before turning on the UV light. After approximately 1 hour, the gas concentration stabilized, and the sample was kept under NOx exposure at concentration level of 1000 ppb and was also exposed to UV light for the next 5 hours. The gas concentration was allowed to re-stabilize for another hour after the UV light was turned off. As a result, one cycle of such NO_x photodegradation test was approximately 7 hours. The plates were subjected to a consecutive three-cycle test to investigate the long-term performance of NO_x photodegradation, with each cycle using the same test condition and procedure as described above. Between each cycle, the samples were not tested for 12 hours. A chemiluminescent $NO/NO_2/NO_x$ analyzer (Model 200A, Teledyne API, San Diego, CA, USA) was used to measure the gas concentration throughout the entire experimental period. All test setups were covered by a black light-blocking canvas to prevent ambient light from affecting the reaction.

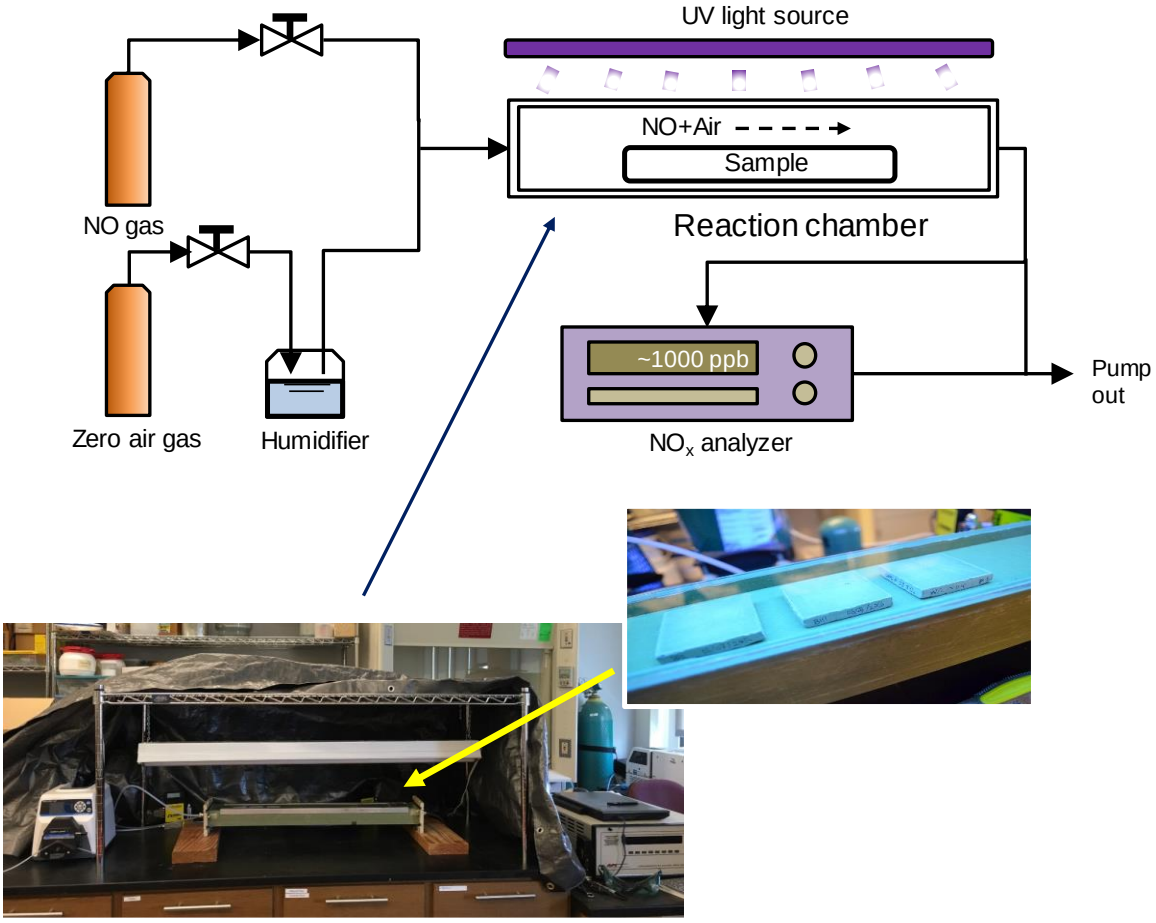

Figure 4-1: Experimental setup of NO_x photocatalytic degradation test for TiO_2-doped cementitious materials

4.2.4 NO_x photodegradation efficiency and capacity

The instantaneous NO_x photodegradation efficiency (η_{NO_x}) and capacity (Q_{NO_x}) were calculated based on the following equations:

$$\eta_{NO_x} = \frac{C_{[NO_x]uptake}}{C_{[NO_x]_{in}}} \times 100\% \quad (4.1)$$

$$Q_{NO_x} = \frac{f}{V}\int_0^T (C_{[NO_x]uptake})\, dt \quad (4.2)$$

$$C_{[NO_x]uptake} = C_{[NO_x]_{in}} - C_{[NO_x]_{out}} \quad (4.3)$$

$$S_{NO_x} = \frac{Q_{NO_x}}{A} \quad (4.4)$$

where η_{NO_x} is the NO_x photodegradation efficiency (%), Q_{NO_x} is the NO_x uptake per cycle (mmol), $C_{[NO_x]uptake}$ is the concentration of NO_x uptake (ppb), $C_{[NO_x]_{in}}$ and $C_{[NO_x]_{out}}$ are the inlet and outlet concentration of NO_x that are measured by NO_x analyzer (ppb), S_{NO_x} is the NO_x photocatalytic capacity (mmol m^{-2}), A is the total area of tested plate samples (75 mm^2), t is the time of NO_x absorption (min), T is the duration of the photocatalytic process per cycle (300 minutes), f is the flow rate of NO_x at 23 °C and 1.01 kPa ($Lmin^{-1}$), and V is the volume of 1 mole ideal gas at 23 °C and 1.01 kPa (24.3 L).

4.2.5 SEM analysis

SEM was performed using JSM-7600F Schottky Field Emission Scanning Electron Microscope (JEOL, Tokyo, Japan) and was coupled with an energy-dispersive X-ray spectroscopy (EDS). After 28 days of curing, a thin piece of slice was obtained by crushing one of the plate samples with hammer and impregnated with low-viscosity epoxy resin, polished, and coated with carbon prior to imaging.

4.3 Results and discussion

The long-term NO_x photodegradation efficiency and capacity for both TiO_2-doped OPC and CAC plate samples were evaluated by standardized NO_x photodegradation test and calculated. The SEM analysis provides the information about the dispersion of TiO_2 nanoparticles and their association with cementitious phases

4.3.1 TiO_2-doped OPC

4.3.1.1 NO_x photodegradation efficiency and capacity

Figure 4-2 shows the NO_x photodegradation of the TiO_2-doped OPC plate samples that are exposed to NO_x and UV for three consecutive cycles. The results are similar for each cycle. An instantaneous drop of NO_x concentration occurred upon initial UV illumination, and then the photodegradation continued throughout the 5-hour test period with η_{NO_x} decreasing. For example, the η_{NO_x} decreases from 59% to 54% during the first cycle. When a new cycle began after the 12-hour break, approximately 1% of the photodegradation efficiency was restored compared to that at the end of the previous cycle. This phenomenon occurs repeatedly in the second and third cycles. When the UV light was off, the NO_x concentration could recover to its initial level.

The recovery of photocatalytic efficiency could be due to several reasons. First, this phenomenon could be because some of the NO_x molecules were physically adsorbed onto

the surface of the plate samples and were released back to the atmosphere during the 12-hour break, restoring certain amount of photodegradation efficiency. Such phenomenon has also been reported previously [31,103,104]. It is also hypothesized that the converted NO_2^- and NO_3^- species could migrate to a deeper level inside the cementitious materials through the interconnected porous microstructure, resulting in some recovery of the photodegradation efficiency on the surface. However, to verify the second hypothesis, the fundamental pathways of NO_x sequestration is needed, and Chapter 7 will provide such information. Nevertheless, the overall trend was that the NO_x photodegradation efficiency decreases, indicating that there must be a limited NO_x sequestration capacity if the environmental and exposure conditions remain the same.

The total NO_x uptake is denoted by the shaded area in Figure 4-2. The average NO_x uptake per cycle is Q_{NO_x} = 6.9±0.2 mmol. Because the total area of the tested plates (A) is 7500 mm^2, the NO_x photodegradation capacity of the TiO_2-doped OPC plate sample is S_{NO_x} = 916.3±20.7 mmol m^{-2}. This result is based on a 5-hour exposure; the daily photodegradation capacity with a longer exposure time could result in a higher NO_x photodegradation. By confirming the photodegradation capacity of TiO_2-doped OPC, policy makers and researchers can develop new strategies of using this photocatalytic material in the current OPC-based concrete infrastructure to remediate atmospheric NO_x. However, this photodegradation capacity slowly decreases. Therefore, evaluations of performance in degrading NO_x should take this effect into consideration.

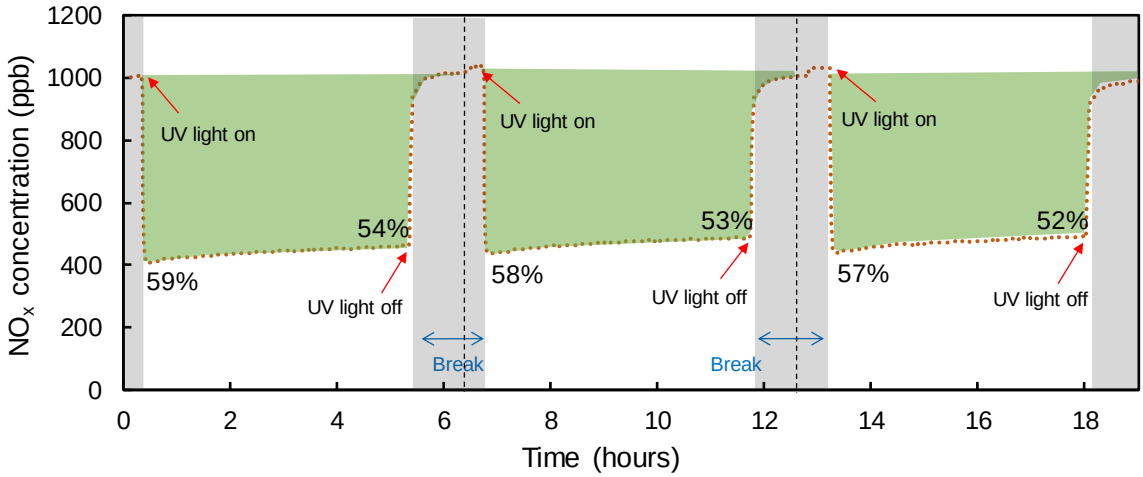

Figure 4-2: Photocatalytic performance of plate TiO_2-doped OPC samples that are exposed to NO_x and UV light for three consecutive test cycles. The photodegradation efficiencies (in %) at the beginning and the end of each cycle are provided. The green shaded area presents the total NOx photodegradation capacity and the grey shaded area means the break between each cycle of the test.

4.3.1.2 Dispersion of TiO_2 particle

The results of SEM analysis for OPC samples are provided in Figure 4-3. The distribution of TiO_2 nanoparticles is highlighted in pink, indicating uniformly distributed TiO_2 nanoparticles within the cementitious hydrates. This uniform distribution ensures a well-distributed and consistent photocatalytic performance of the TiO_2-doped OPC samples. The hydrated phases can also be identified by SEM. The light grey color represents portlandite (CH) and the dark grey color represent C-S-H. Voids and anhydrate cement particles can also been seen in the image. All of these phases have also been identified by TGA and XRD analyses from Chapter 3. As a result, TiO_2 nanoparticles

exhibit no preference to bind with any particular hydrated phases in OPC samples, which is expected since the TiO_2 is considered inert in the OPC hydration reactions relevant to this study.

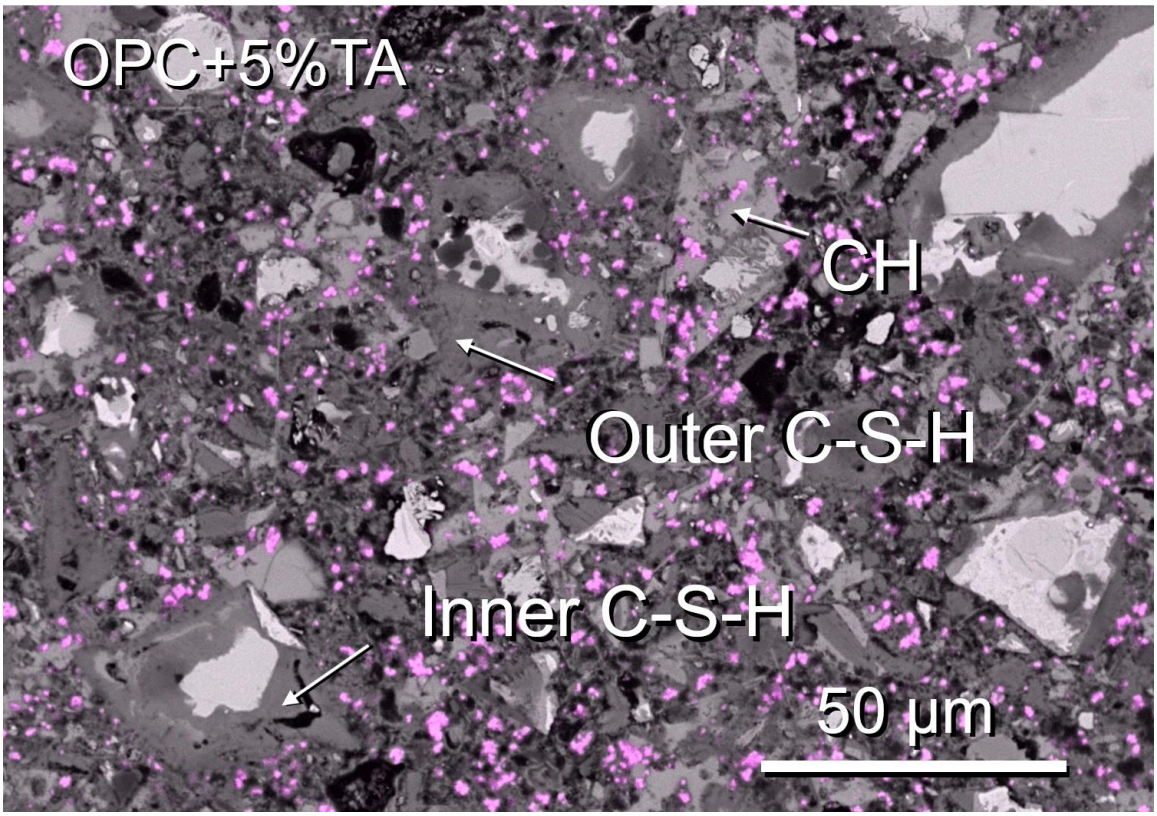

Figure 4-3:. SEM analysis of TiO_2-doped OPC samples, with TiO_2 highlighted.

4.3.2 TiO_2-doped CAC

4.3.2.1 NO_x photodegradation efficiency and capacity

Figure 4-4 shows the NO_x photodegradation of the TiO_2-doped CAC plate samples that are exposed to NO_x and UV for three consecutive cycles. Compared to OPC samples, CAC exhibit a lower photodegradation efficiency at a higher deceleration rate. For

example, the η_{NO_x} at the beginning is 53% and decreased to 46% during the 5-hour exposure period of the first cycle. This decrease could be due to the differences in chemical composition and microstructural properties between OPC and CAC samples. Previous studies have suggested that the higher NO_x photodegradation efficiency found in OPC samples could be related to the presence of calcium silicate hydrates (C-S-H) with a very high surface area in the range of 10's to 100's of m^2/g [105]. This phase is a product of alite (C_3S) and belite (C_2S) hydration, which is the major compositions in OPC cement according to material characterization in Section 4.1.1, and its complex structure is believed to participate in the adsorption of NO_x converted products [41]. As a result, the average NO_x uptake, denoted by the shaded area in Figure 4-4, is lower than OPC and Q_{NO_x} = 5.6±0.3 mmol per cycle. The corresponding NO_x photodegradation capacity of the CAC plate sample is S_{NO_x} = 753.1±43.4 mmol m^{-2}. The recovery of photodegradation efficiency is also observed in CAC samples. When a new cycle began after the 12-hour break, approximately 3% NO_x photodegradation efficiency was restored compared to that at the end of the previous cycle. Again, the difference in the recovery fraction could also be due to the different chemical composition and microstructural properties between OPC and CAC samples.

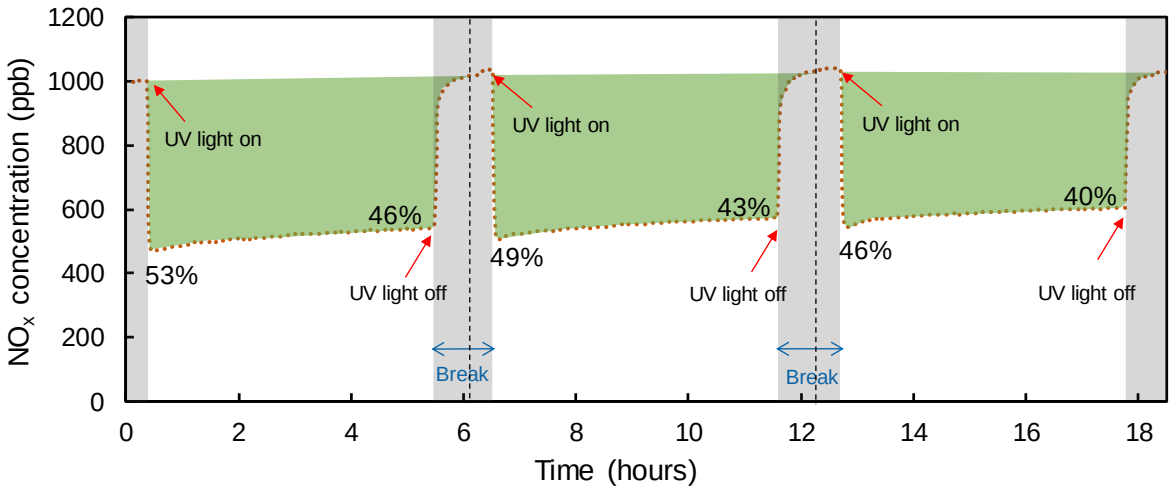

Figure 4-4: Photocatalytic performance of plate TiO_2-modified CAC samples that are exposed to NO_x and UV light for three consecutive test cycles. The photodegradation efficiencies (in %) at the beginning and the end of each cycle are provided. The green shaded area presents the total NOx photodegradation capacity and the grey shaded area means the break between each cycle of the test.

4.3.2.2 Dispersion of TiO_2 particle

The results of SEM analysis are provided in Figure 4-5. The distribution of TiO_2 nanoparticles is highlighted in pink, indicating uniformly distributed TiO_2 nanoparticles within the cementitious hydrates. This uniform distribution ensures a well-distributed and consistent photocatalytic performance of the TiO_2-doped CAC samples. The hydrated phases can also be identified by SEM coupled with EDS analysis. The C_2AH_8 phase can be identified by the gray area surrounded by cracks, which were caused by drying and shrinkage during the sample preparation as well as in the microscope chamber [106]. The

presence of this phase is also reflected in the XRD and TGA result in Chapter 3. The dark gray areas represent the amorphous AH_3 phase; these areas are often intermixed with the CAH_{10} phase and can be hard to distinguish merely by direct observation [106]. Therefore, EDS was carried out to examine the element ratios to identify the correct phases. The result of the pastes shows a Ca:Al ratio of approximately 1:2, indicating the presence of the CAH_{10} phase in these dark gray areas. These findings are also supported by the XRD patterns and TGA analysis from Chapter 3. The lighter gray areas represent the crystalline C_3AH_6 phase, which is also detected in both the XRD and TGA analyses. In addition, this phase is also observed near the cement grains and has also been identified by other research [90,106]. These results indicate TiO_2 nanoparticles do not preferentially bind with any particular hydrated phases in CAC or OPC samples.

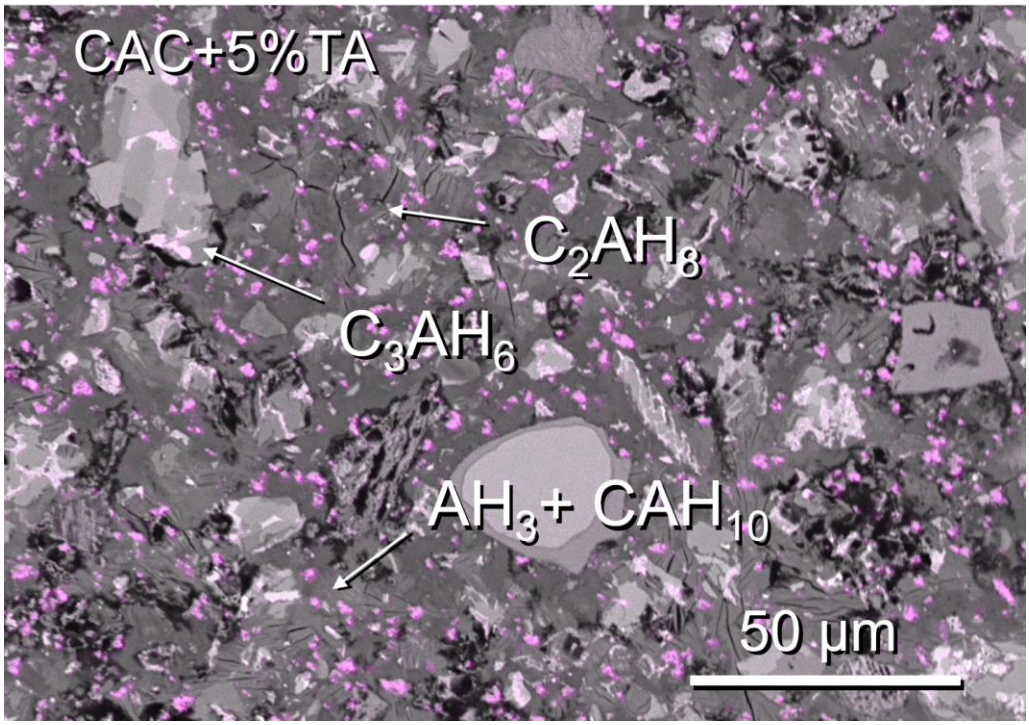

Figure 4-5:. SEM analysis of TiO_2-doped CAC samples, with TiO_2 highlighted.

4.4 Conclusions

The long-term photocatalytic performance of both TiO_2-doped OPC and CAC materials are studied in this chapter using a multi-cycle test. The results show that the NO_x photodegradation efficiency decreases with exposure time, with CAC samples showing a higher deceleration rate than OPC samples. Compare to than CAC samples, OPC samples exhibit higher NO_x photodegradation efficiency, which results in a NO_x photodegradation capacity of approximately 916 mmol m^{-2} for OPC samples and 753 mmol m^{-2} for CAC samples. When conducting a life cycle assessment to evaluate the environmental performance of TiO_2-doped cementitious materials, the effect of decreasing the rate of NO_x photodegradation efficiency should be taken into consideration.

During the multi-cycle test, approximately 1% of the photodegradation efficiency was restored at the beginning of each cycle (after a 12-hour break) in OPC samples compared to that at the end of the previous cycle. For CAC samples, approximately 3% of the photodegradation efficiency was restored. This phenomenon occurs repeatedly in the second and third cycles. The differences in the photodegradation efficiency and percentage of recovery could also be due to the different chemical compositions and microstructural properties between OPC and CAC samples. Further investigation into the fundamental understanding of the pathways of NO_x sequestration is provided in Chapter 7.

The SEM/EDS analyses show that the TiO_2 nanoparticles are uniformly distributed within the cementitious hydrates without preference to bind to any particular hydrated phases, ensuring a well-distributed and consistent photocatalytic performance of the TiO_2-doped cementitious materials.

CHAPTER 5. PHOTOCATALYTIC PERFORMANCE OF TIO_2-COATED CEMENTITIOUS MATERIALS

5.1 Introduction

Chapter 4 has examined the photocatalytic performance of TiO_2-doped cementitious materials. Because the photocatalytic reactions are surface phenomenon [30,34,37,52], it would be more effective and economically efficient to apply TiO_2-modified coatings to the surface of cementitious material. This chapter focus on examining the photocatalytic performance of TiO_2-coated cementitious materials, in terms of air-purification and self-cleaning properties.

To improve the durability and reduce the cost of the TiO_2-modified coatings, researchers have proposed to include silica (SiO_2) in the TiO_2-modified coatings since the production of SiO_2 is less expensive than TiO_2 and SiO_2 has a higher mechanical and thermal stability than TiO_2 [65,84,107]. In addition to lower cost and higher durability, the introduction of SiO_2 will also alter the hydrophilic effects of coated surfaces [67]. A coated hydrophobic surface can be achieved through the application of hydrophobic SiO_2. However, concerns about bond strength between the TiO_2-SiO_2 coating and cementitious substrates have been raised [84], and thus the bonding of the coating to the surface is also of interest.

While the photocatalytic performances of TiO_2-SiO_2 coated cementitious materials depend on the durability and composition of the coating, recent studies have shown that the microstructure of cementitious materials also plays an important role in the

photocatalytic performance [39,103]. OPC and CAC are selected to understand the correlation between the microstructure of different cementitious materials and their photocatalytic performances since their different chemical composition and hydration lead to different microstructures. The details of different TiO_2- and SiO_2-modified coatings will be described and their photocatalytic performances (i.e. air-purification and self-cleaning) are evaluated by NO_x degradation and Methylene Blue (MB) methods, respectively. The interaction between the different coatings and these cementitious substrates will also be investigated. Finally, a recommendation for selecting coating design will be provided.

5.2 Experimental program

5.2.1 Preparation and characterization of cementitious substrates

The cementitious substrates were prepared from two types of cements: ASTM C150 Type I/II Portland cement (OPC) (Argos, Atlanta, Georgia, USA) and calcium aluminate cement (CAC) (Kerneos, Chesapeake, Virginia, USA). The chemical compositions of the cements are provided in Table 5-1.

To produce cementitious substrates, deionized water (18.2 MΩ-cm) was added to the cement and mixed for two minutes using a handheld electric mixer. The water-to-cement ratio was kept constant, for all mixtures, at 0.40. Plate samples, 50.8 × 50.8 × 9.5 mm (width × length × height), were cast against a smooth surface without any use of a release agent and stored at 23 ± 2 °C for the first 24 hours under plastic sheeting to maintain high humidity. The plate samples were removed from their molds after 24 hours and subsequently cured in limewater at room temperature (23 ± 2 °C) for 28 days. After curing,

the cement paste surfaces were polished using 600-grit (16 μm particle size) sandpaper. Prior to the application of photocatalytic coatings, all samples were conditioned at 23 ± 2 °C and 50 ± 5% relative humidity until there was no significant mass change (change of less than 0.5% over a 6-hour period). According to X-ray diffraction (XRD) analysis, the conversion of the CAC samples was low. This was expected due to the relatively low curing temperature and low age at the time of testing.

Table 5-1: Chemical Compositions of OPC and CAC Cements

Cements	SiO_2	Al_2O_3	Fe_2O_3	CaO	MgO	SO_3	Na_2O	LOI
OPC	19.2	4.5	3	62.8	3.6	3.1	0.5	2.6
CAC	5.5	45.2	6.9	37.7	0.2	0.07	0.26	1.9

5.2.2 Preparation and characterization of photocatalytic coatings

Different synthesis methods have been proposed to produce TiO_2-SiO_2 composite coatings in past decades, including direct methods [84], a precipitation method [64], and the sol-gel methods [108]. In this chapter, a direct method was used of applying TiO_2 and SiO_2 sol-gel layers on the cementitious substrate. For samples that contain both TiO_2 and SiO_2 layers, the SiO_2 layer was first applied on the surface by uniformly spraying SiO_2 sol-gel suspensions on the cementitious substrate and then dried at 23 °C overnight; then the TiO_2 layer was applied on the top of the coated surface to produce the final composite

coatings. The thickness of the applied layers was estimated by dividing volume of suspension applied on the surface of cementitious substrate by the surface area of the substrate. Since the area of the substrate was the same for each sample and the coating was uniformly applied, the coating thickness was kept the same in this study. A previous study has also demonstrated that as long as the coating is uniformly applied on the surface of the substrate and covers the entire surface, the photocatalytic capability is the same regardless of the coating thickness [84].

Three sol-gel suspensions were used to make coatings: 1) a lab-produced TiO_2 suspension, which was prepared by adding 8.25 mL of titanium isopropoxide hydrolysis (97%) in an acid media, which was obtained by adding 0.71 mL of HNO_3 (65%) to 100 mL of deionized (DI) water. The concentration of the lab-produced TiO_2 suspension is 22±2 g of TiO_2 per liter of suspension (g/L); 2) a commercial hydrophobic SiO_2 sol-gel suspension based on siloxanes and its concentration is 5±1 g/L; and 3) a lab-produced hydrophilic SiO_2 suspension, which was prepared by adding 15 mL of tetraethylorthosilicate hydrolysis (>98%) in the same acid media as found in 1). The concentration of the lab-produced hydrophilic SiO_2 suspension is 26±3 g/L. The pH of both lab-produced TiO_2 and SiO_2 suspensions was 2.5-3.0. The TiO_2 suspension was prepared by the anatase phase, confirmed by XRD analysis, as it is considered more photocatalytically active than rutile phase [60]. According to XRD analysis, both silica suspensions were amorphous. Different cementitious substrates and coating schemes were used to compare the photocatalytic and adhesive performance; their nomenclatures are summarized in Table 5-2.

The characterizations of the photocatalytic coatings are as follows: the porosity of cementitious samples was studied by mercury intrusion porosimetry (MIP) method, assuming a cylindrical non-intersecting pore model, with the values recommended by the IUPAC of 141º and 484 mN/m, for the contact angle and surface tension of mercury, respectively. A cubic sample was carefully cut from the plate substrate with the length of 0.8 cm to ensure the piece could be introduced into the sample holder for MIP analysis. When placing the sample into the sample holder, the coated surface was always facing up. The hydrophilicity and hydrophobicity for all photocatalytic-cements were determined by measuring the contact angle of the water drop over the solid surface using the software www.geogebra.org. The image of the water drop on the sample surface was acquired by a USB microscope. Adhesion tests were performed following ASTM D335930, using a standardized multi-cutter. The scanning electron microscopy (SEM) images of the coated surface after the adhesion tests were obtained by tablet Microscope.

Table 5-2: Matrix, coating scheme and test results of photocatalytic cementitious materials

Sample ID*	OPC	CAC	Coating composition			Test results		
			T	S1	S2	Contact angle (°)	NOx conversion (%)	50% MB dye bleaching $t_{1/2}$ (min)
PB	×					13	0	-
PT	×		×			0	65	260
PS1	×			×		156	0	-
PST1	×		×	×		103	52	1990
PS2	×				×	0	0	-
PST2	×		×		×	6	60	980
C4B		×				11	0	-
C4T		×	×			6	50	230
C4S1		×		×		130	0	-
C4ST1		×	×	×		131	32	295
C4S2		×			×	8	0	-
C4ST2		×	×		×	6	40	3280

* Sample ID: P – OPC, C4 – CAC, B – blank cementitious materials (control), T- lab-produced TiO_2, S1- commercial hydrophobic SiO_2, and S2 – lab-produced hydrophilic SiO_2. For example, PST1 indicates OPC substrate topped by a titanium dioxide layer followed by a layer of the commercial silica suspension.

5.2.3 NO_x photo-degradation test

The nitrogen oxide (NO_x) photo-degradation tests were performed following procedures in the ISO 22197 [46] and JIS R 1701 Standards [47]. The test setup is shown in Figure 5-1. Three identical cement plates with a total exposed area of 7500 mm^2 were placed in the reaction chamber under two 40W UV fluorescent lamps with peak emission at 365 nm. The intensity of UV light at the sample surface was maintained at 10 Wm^{-2} by adjusting the distance between the UV light source and the coated cement samples. A mixture of 1 ppm nitric oxide (NO) gas and ultrapure dry air blew through the reaction chamber at a total flow rate of 1 $L \cdot min^{-1}$. The chamber was held at a constant temperature of 23 ± 2 °C and a relative humidity of 50 ± 5%. The initial gas concentration was kept at ~1000 ppb before turning on the UV light. Once the gas concentration stabilized, the UV light exposure started and continued for 5 hours. After the UV light was turned off, the gas concentration was allowed to stabilize. The gas concentration was continuously measured by chemiluminescent $NO/NO_2/NO_X$ analyzer Model 200A, Teledyne API. To investigate their long-term NO_x performance, PT and C4T were selected for a consecutive two-cycle test. Each cycle had a consecutive 5-hour NO_x and UV light exposure followed by a 12-hour break, using the same testing conditions as the single cycle test. Samples were not treated during the breaks.

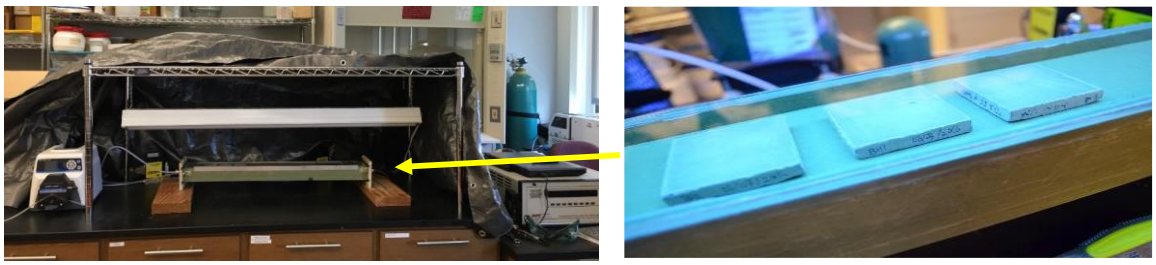

Figure 5-1: NO_x photocatalytic degradation test for TiO_2-coated samples

5.2.4 Methylene blue (MB) dye photo-degradation test

MB dye photo-degradation tests were conducted in a closed and refrigerated chamber at a constant temperature of 25 ± 2 °C, equipped with six 15W Black Blue Light fluorescent lamps which emit UV light with wavelengths centered at 365 nm. The samples' locations were adjusted to receive 20 $W \cdot m^{-2}$ irradiance. The detailed procedure and determination of the amount of MB required to provide enough color contrast can be found in previous research [109]. The spot of MB dye was applied by depositing 0.1 mL of a 3.2 x 10^{-3} M MB solution in water: acetone ratio of 1:1, on the surface of the samples. The MB photo-degradation was quantitatively measured by UV-visible diffuse reflectance spectroscopy (Agilent Cary 5000 with integrating sphere) at irradiation periods from 0 to 3750 mins.

5.3 Results and discussion

The test results are summarized in Table 5-3. The microstructure of both the OPC and CAC cementitious material was obtained by combining data obtained by specific surface area (BET) and MIP methods. The hydrophilicity and hydrophobicity of coated cementitious material surfaces were studied by the wettability test. The bonding between coatings and cementitious substrates were examined by the adhesion test and analyzed by SEM. The photocatalytic NO_x degradation was studied by the NO_x exposure test, and the photocatalytic self-cleaning property of photo-cement was investigated by the MB dye degradation test. The detailed test results and discussions, which relate observations on performance to composition and structure, are provided in the following sections.

5.3.1 Characterization studies

Figure 5-2 shows the pore size distribution of all studied photocatalytic cementitious materials. For OPC samples, the results suggest that coatings did not significantly affect the surface porosity or pore structures. For CAC samples, variations were observed in peaks of 200-300 nm, 2,000 nm, and 20,000 nm. This suggests that the coatings alter the surface porosity and pore structures of CAC samples. Further studies are needed to understand the fundamental mechanism of the coating's effect on surface microstructures. It should be emphasized that important differences were observed between OPC and CAC samples. OPC samples show a greater proportion of pores smaller than 100 nm, with a maximum macropore size of around 45-100 nm, compared to CAC. CAC samples show a pore size distribution with three well-defined macropores of 100, 2,000, and 20,000 nm, significantly coarser than those in the OPC. These differences likely relate to the inherent variations in the hydration product morphology of these two cementitious systems and could affect the photocatalytic performances of OPC and CAC based cementitious materials [98].

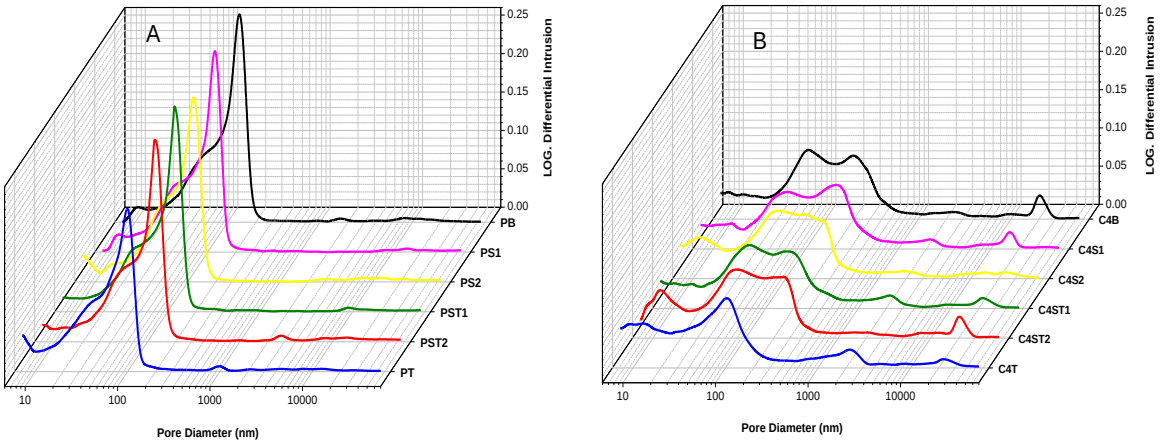

Figure 5-2: Pore size distribution of (a) OPC and (b) CAC

The hydrophilicity and hydrophobicity of the photocatalytic cementitious material surfaces were studied by the wettability test. The results show the interactions between the sample surfaces and water. The contact angles of all coated samples are provided in Table 2. Based on the previous studies [110–112], surfaces of photocatalytic cementitious materials with contact angles smaller than 90º are considered hydrophilic and with contact angles larger than 90º are considered hydrophobic. The uncoated control samples (PB and C4B) were found to have contact angles of 13º and 11º, respectively. This indicates that the surfaces of cementitious substrates are hydrophilic, which is expected. Thus, by applying different coatings to the surfaces of cementitious materials, hydrophilicity could be altered. Samples with only lab-produced TiO_2 coating (PT and C4T) exhibited hydrophilic surfaces. This indicates the TiO_2 coating should also be hydrophilic. Samples with lab-produced SiO_2, with or without the second TiO_2 layer (PS2, PST2, C4S2, and C4ST2), also exhibited hydrophilic surfaces. This is also expected as the lab-produced SiO_2 is made to be hydrophilic. In contrast, the samples with commercial hydrophobic SiO_2 coatings (PS1, PST1, C4S1, and C4ST1) exhibited hydrophobic surfaces and presented contact angles larger than 100º. The results indicate that the hydrophilic coated surfaces can be changed to hydrophobic by including a hydrophobic silica layer in between the TiO_2 layer and cementitious substrate. The ability to achieve surface hydrophobicity lends this TiO_2-SiO_2 nanoparticle-modified coatings to broad applications. For example, in repair applications, hydrophobic coatings are more favorable since it could help prevent water from penetrating into concrete, potentially avoiding future repairs in the same area.

The inclusion of a silica layer also affects the bond strength between coating and cementitious materials. Bonding between coatings and cementitious substrates were

evaluated by micrographs obtained after the adhesion tests (Figure 5-3). Coated cementitious materials with a lab-produced hydrophilic SiO_2 interlayer, with or without a titania layer (PS2, PST2, C4S2, and C4ST2), show the coatings can be easily peeled off during the cut without damaging the surfaces of cementitious substrates. Similar observations are made from samples only coated with TiO_2 layers (PT and C4T). This result indicates a weak bond between these coatings and cementitious substrates. In contrast, the surfaces of samples coated with commercial hydrophobic silica layer (PS1, PST1, C4S1, and C4ST1), are irregular and rough during the cut. This result indicates a strong bonding between coatings and cementitious substrates as the damage occurs in the cementitious substrate when peeling off the coatings. This strong bond performance appears to be related to the hydrophobicity or other characteristics of the commercially produced silica layer, since the cementitious substrate did not bond as well to the lab-produced hydrophobic silica-based coating. Further work, including the characterization of commercial SiO_2 sol-gel suspension, is needed to understand the underlying mechanism for this bonding behavior. It should be noted that for coated concrete infrastructure that is subjected to abrasion, a strong bond between coating and cementitious substrate is preferable.

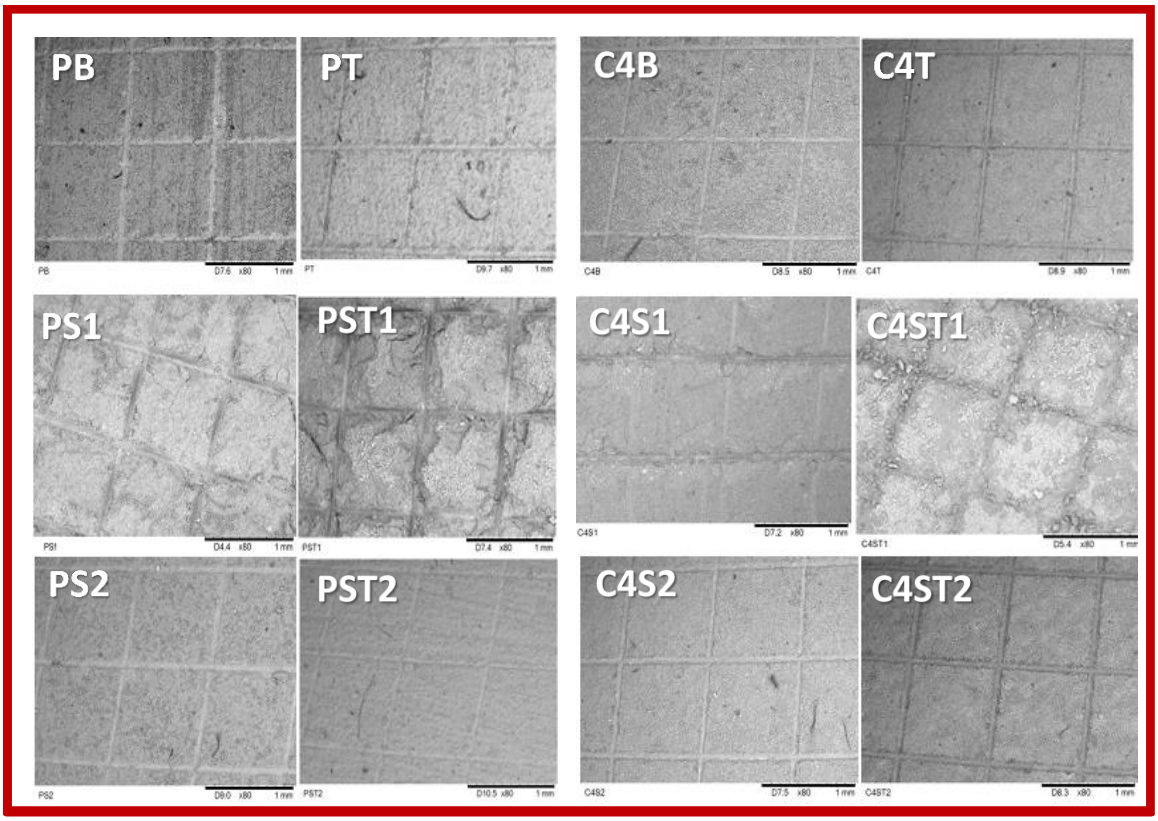

Figure 5-3: Micrograph of Adhesion Tests

5.3.2 NO_x photodegradation

The results of the NO_x photo-degradation test along the radiation period are shown in Figure 5-4 and the photo-degradation efficiencies are summarized in Table 5-2. The photocatalytic cementitious materials that contain a TiO_2 layer, have shown an instantaneous drop of NO_x concentration upon initial UV light illumination. The photo-degradation of NO_x continued throughout the 5-hour test period, and when the UV light was off, NO_x concentration recovered to the initial level, as expected. The NO_x photo-degradation is believed to be a two-step process, where NO_x is first converted to nitrite and nitrate ions and then the ions are bound with cementitious substrate. Therefore, as

mentioned in the introduction, the microstructure of cementitious substrate can affect NO_x photo-degradation through the second step.

In general, the OPC-based photocatalytic cementitious materials (i.e. PT, PST1 and PST2) have NO_x photo-degradation efficiency of 65%, 52% and 60%, respectively, while the CAC-based ones (i.e. C4T, C4ST1 and C4ST2) have 50%, 32% and 40%, respectively. The order of photocatalytic efficiency is: PT>PST2>PST1 for OPC samples and C4T>C4ST2>C4ST1 for CAC samples. The higher NO_x photo-degradation efficiency found in OPC based photocatalytic cementitious materials could be related to the presence of calcium silicate hydrate (C-S-H). C-S-H has a very high surface area (in the range of 10's to 100's of m^2/g [105], has a variable composition, and is structurally amorphous to semi-crystalline. This phase is a product of alite (C_3S) and belite (C_2S) hydration, and its complex structure is believed to participate in the adsorption of NO_x oxidized products[1]. Based on the characterization study, OPC has a higher SiO_2 and CaO content (Table 5-1), compared to CAC and shows a more uniform pore size distribution (Figure 5-2). It is proposed that the presence of C-S-H in hydrated OPC contributes largely in binding the photocatalytic products from NO_x degradation and hence results in a higher NO_x photo-degradation efficiency.

It was also observed that for both OPC and CAC based photocatalytic cementitious materials, the inclusion of SiO_2 layers reduced the NO_x photo-degradation efficiency. Since the SiO_2 layer was applied in between the TiO_2 layer and cementitious substrate, it could interrupt NO_x from participating in the near surface reaction of cementitious substrates and hence reduce the NO_x photo-degradation efficiency. For example, the acidity of a SiO_2 layer with a pH of 2.5-3.0 could interact with the near surface C-S-H and calcium

hydroxides, and as a result affect the NO_x binding and its photo-degradation efficiency. Therefore, the photocatalytic performance of a TiO_2- SiO_2 composite coating could be compromised by the interruption between the coating and cementitious substrate. Comparing S1 and S2, the hydrophobic S2 layer further worsens the NO_x photo-degradation efficiency. This may be due to the hydrophobicity of the S2 layer and the chemicals that were used to create a strong bond between the coating and cementitious substrate have an even stronger impact on the interruption of the NO_x near surface reaction. Therefore, caution should be made when applying the silica layer to alter the hydrophobicity of the coated surface and to enhance the bond strength.

The long-term NO_x photo-degradation was examined by a two-cycle test with each cycle having a consecutive 5-hour NO_x and UV light exposure followed by a 12-hour break. Only TiO_2 coated photocatalytic cementitious materials (PT and C4T) were selected for the tests. The results are shown in Figures 5. Again, the OPC based photocatalytic cementitious material (PT) exhibited a higher NO_x photo-degradation efficiency than the CAC (C4T). A trend in reduced NO_x photo-degradation was observed during the given cycles. It suggests that the photocatalytic cementitious materials have a limited capacity of NO_x photo-degradation if the external environmental conditions keep the same.

The NO_x photo-degradation tests support the hypothesis that the NO_x photo-degradation efficiency not only depends on the photocatalytic activity of the coatings, but also on the characteristics of the cementitious substrates. Therefore, it is critical to understand what characteristics of cementitious materials are responsible for NO_x photo-degradation, such as the hydrated cement phases, to optimize the design of a cementitious substrate for maximizing NO_x photo-degradation efficiency.

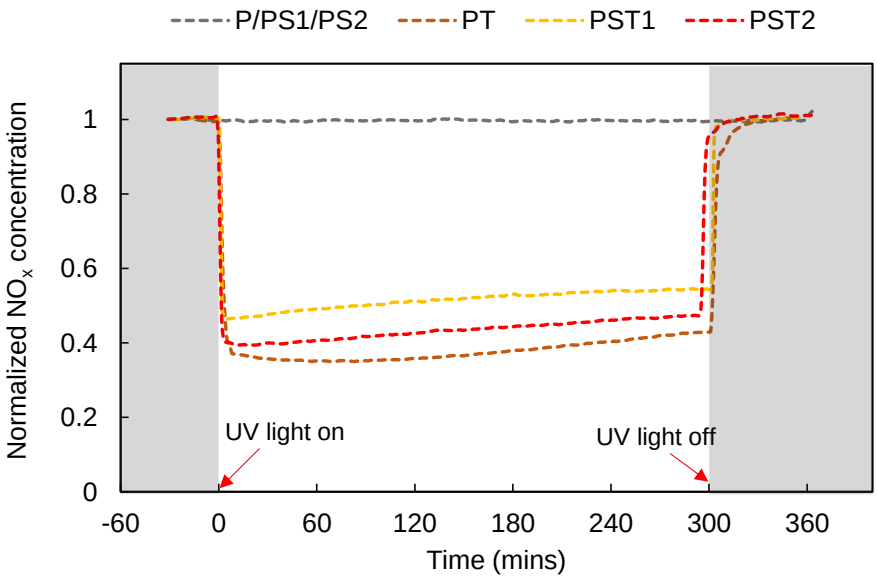

(a)

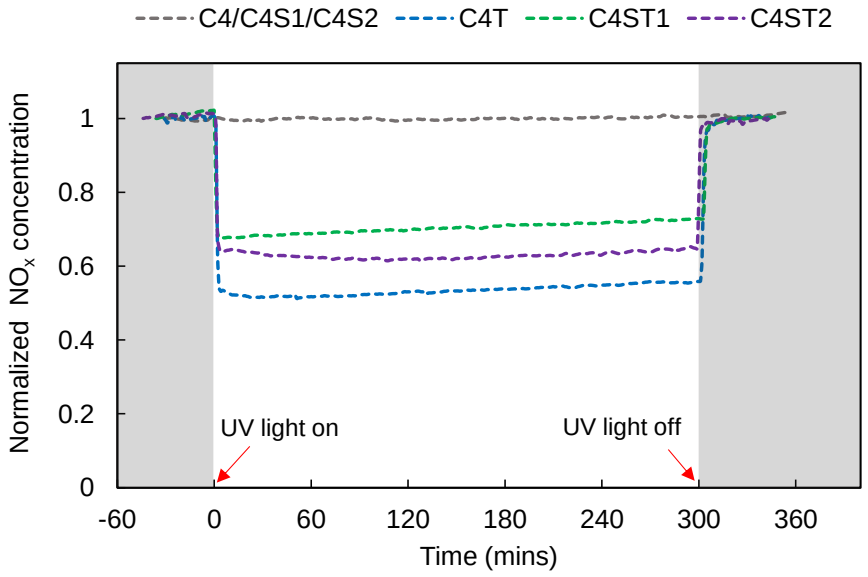

(b)

Figure 5-4: NO_x photo-degradation test (a) OPC samples (b) CAC samples

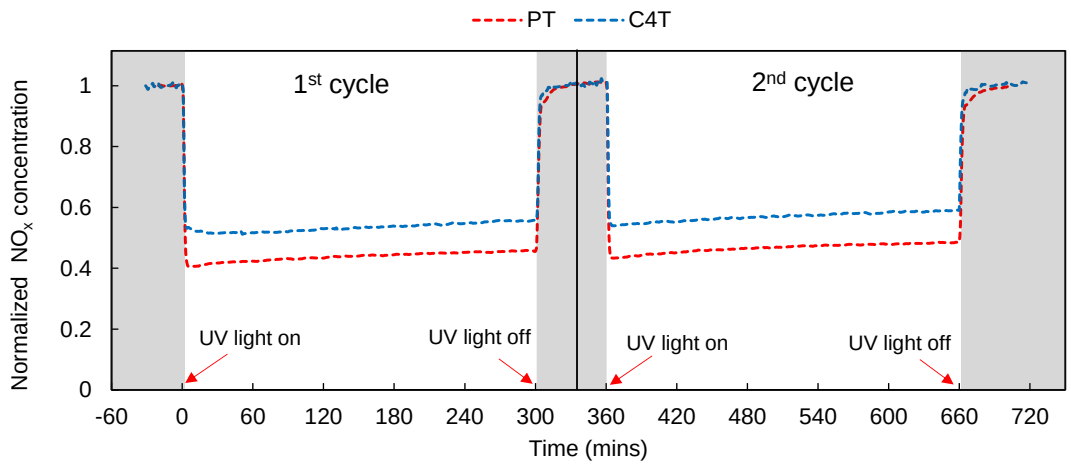

Figure 5-5: NO_x photo-degradation – Two cycle test

5.3.3 Methylene Blue (MB) photo-degradation

Researchers have brought up concerns about the validity of the MB photo-degradation test that is sensitized by TiO_2, especially in the presence of oxygen [113,114]. However, its application in photocatalytic cementitious materials still can provide useful insights [84], in particular the correlation between MB photo-degradation and photocatalytic self-cleaning behavior. In this study, it was observed that cementitious materials with a TiO_2 layer show a significant MB photo-degradation while the ones without TiO_2 show unmeasurable MB photo-degradation. This evidence suggests that the coatings containing TiO_2 promote the photocatalytic activity and hence increase the rate of MB photo-degradation.

The results of the MB photo-degradation for photocatalytic cementitious materials along with the radiation time are shown in Figure 5-6. The time to achieve 50 % MB dye bleaching ($t_{1/2}$) is indicated by the red dashed line in Figure 5-7 and are summarized in

Table 5-2. For both OPC and CAC samples, the samples with only TiO_2 layers exhibit a faster 50% MB dye bleaching (lower value of $t_{1/2}$) than samples with TiO_2-SiO_2 layers. This result coincides with the findings from the NO_x photo-degradation tests and indicates that the inclusion of silica layers may affect the interaction between coatings and cementitious substrates, hence reduceing the MB photo-degradation efficiency. However, the cementitious substrate seems to play a less important role in the MB photo-degradation, which indicates the MB photo-degradation could largely depend on the photocatalytic performance of the coatings. Moreover, caution should be taken when translating this experiment to real world self-cleaning applications since other factors such as a high humidity and pH can also affect the photocatalytic performance [115].

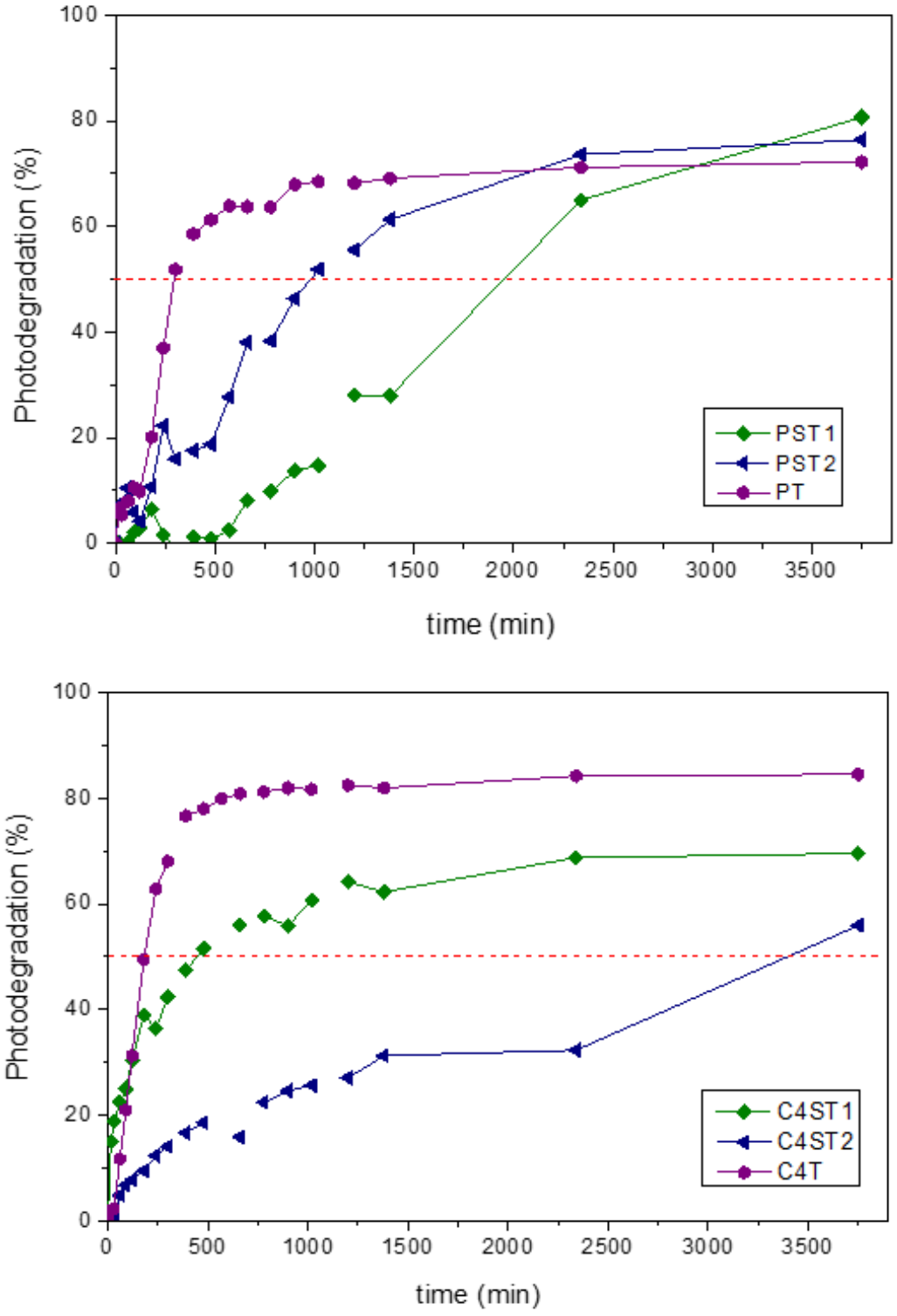

Figure 5-6: MB degradation: above, OPC samples and below CAC samples

5.4 Conclusion

This chapter examines the photocatalytic performance of titania and silica (TiO_2 and SiO_2) nanoparticle-modified coatings for cementitious materials. Portland cement (OPC) and calcium aluminate cement (CAC) were used to prepare the cementitious substrates. The substrates were each coated with a lab-produced TiO_2 (T) layer, a commercial hydrophobic SiO_2 (S1) layer, and a lab-produced hydrophilic SiO_2 (S2) layer. Based on the characterization studies and photocatalytic tests, the following conclusions can be drawn.

Based on the results of the microstructural characterization, the coatings have insignificant effect on the microstructural features of OPC cementitious materials but have notable effect on CAC samples, especially on the pores sized 200-300 nm in diameter. The results of wettability testing show that the composite coatings that contain hydrophobic SiO_2 affect the interactions of coated surfaces with water. The results of adhesion testing indicate that the coated cementitious materials with a commercial hydrophobic SiO_2 layer show the strongest bonding to the substrates.

In examining the NO_x and MB photo-degradation, the cementitious substrates coated by only TiO_2 (samples PT and C4T) exhibit higher efficiencies of both NO_x photo-degradation and MB photo-degradation. The inclusion of SiO_2 layers seem to reduce the photocatalytic performance of coated cementitious materials, especially the ones containing commercial SiO_2 layers. The results of MB photo-degradation tests suggest that the cementitious substrates may have a limited impact on photocatalytic performance. In comparing the two cements OPC-based cementitious materials show higher photocatalytic efficiencies than CAC-based ones. It is proposed that the higher efficiency could be

attributed to the finer and more uniform porosity in OPC-based cementitious materials, as well as the presence of high-surface area calcium silicate hydrates (C-S-H). The results in the two-cycle tests for both OPC and CAC photo-cements exhibit a decreasing rate in NO_x photodegradation over time, indicating the materials may have a limited capacity of NO_x photo-degradation.

For selecting or designing coatings, it is important to consider the following three factors: the bond strength between the coating and the cementitious substrate, the desired coated surface interaction with water (i.e. hydrophilicity and hydrophobicity), and the photocatalytic performance. For example, if the coating is used to repair a pavement surface that is subject to abrasion, a strong bond and hydrophobicity are preferable. Therefore, it is recommended to apply the commercial hydrophobic SiO_2 to the cementitious substrate to improve the bonding performance and to achieve hydrophobicity. If the coating is used to remove atmospheric NO_x and clean its surface, then a higher photocatalytic performance is more desirable. In this case, the SiO_2 layer should be excluded to maximize the material's photocatalytic efficiency.

CHAPTER 6. QUANTIFICATION OF NO_X UPTAKE IN TIO_2-MODIFED CEMENTITIOUS MATERIALS

6.1 Introduction

As discussed in Chapter 2, NO_x photodegradation is generally the result of the oxidation of NO_x by hydroxyl radicals ($OH^{\bullet}$) and superoxide radicals ($O_2^{\bullet-}$). This leads to the formation of nitrite (NO_2^-) and/or nitrate (NO_3^-) through a series of photocatalytic oxidation reactions. Although Chapter 4 and 5 have examined the NO_x photodegradation of TiO_2-doped and TiO_2-coated plate cementitious samples, respectively, the relative abundance of the nitrite and/or nitrate produced has not been clearly quantified, and likely depends on the characteristics of the substrate materials.

Because cementitious materials are structurally and chemically complex hydrated materials, they may influence and participate in these photocatalytic reactions, such as affecting the amount of nitrite and/or nitrate formed and the manner in which NO_x is bound within the material. As discussed in Chapter 1 and 2, such information on N speciation and mass distribution is important for a number of reasons. First, due to the intrinsic chemical differences between nitrite and nitrate, they can interact differently with cementitious phases. For example, these ions could dissolve in the alkaline pore solution [116], adsorb to hydrate surfaces [116], and/or substitute for sulfate ions within aluminum-bearing hydrated phases (AFm and AFt) [117]. Second, nitrite and nitrate, when incorporated into steel-reinforced concrete, can serve as corrosion inhibitors [45]. Therefore, information about the concentration and relative percentages of nitrite and nitrate formation is critical

to understanding their interactions with complex cementitious materials for maximized corrosion resistance.

To quantify the concentration and relative percentages of nitrite and nitrate in TiO_2-doped cementitious materials after NO_x exposure, this chapter develops a novel experimental approach that combines wet chemical extraction, ultraviolet-visible (UV-vis) spectrophotometry, and ion chromatography (IC) measurements. The NO_x sequestration capacities of both ordinary portland cement (OPC)-based and calcium aluminate cement (CAC)-based materials are determined through the measured nitrite and nitrate concentrations. Crushed samples are used in this chapter to increase reaction potential between the sample and NO_x through a higher surface area and ensure detectable concentrations of nitrite and nitrate can be achieved. The mass balance between the NO_x input and NO_x measured at the outlet is compared to measured nitrite and nitrate quantities in the exposed cement paste. Microstructural analysis is also carried out in this study to establish a relationship between microstructural features of cement-based materials with NO_x uptake.

6.2 Materials and Methods

6.2.1 Materials

The samples were prepared from ASTM C150 Type I/II OPC (Argos, Atlanta, Georgia, USA) and CAC (Kerneos, Chesapeake, VA, USA) combined with 5 wt% TiO_2 photocatalysts that are optimized under UV irradiance of 10 Wm^{-2} (KRONOClean® 7050,

Kronos Worldwide). The water-to-solid ratio was kept constant at 0.40. The chemical compositions of both cements, which have been analyzed and obtained from Chapter 3, are listed in Table 6-1. The characteristics of the anatase TiO_2 are listed in Table 6-2. The mineral composition of both cements can be determined by QXRD, and for OPC has a mineral composition of 62.9% of C_2S, 7.7% of C_2S, 6.9% of C_3A, and 9.2% of C_4AF; and CAC contains 57.0% of CA, 8.6% of CA_2, 16.2% of C_2AS, and 1.5% of $C_{12}A_7$.

Table 6-1: Chemical Compositions of OPC and CAC Cements

Cements	SiO_2	Al_2O_3	Fe_2O_3	CaO	MgO	SO_3	Na_2O	LOI
OPC	19.2	4.5	3	62.8	3.6	3.1	0.5	2.6
CAC	5.5	45.2	6.9	37.7	0.2	0.07	0.26	1.9

Table 6-2: Characteristics of TiO_2 photocatalyst (provided by manufacturer).

TiO_2 content	Phase	Density	Bulk Density	Specific Surface Area
>85%	Anatase	3.9 g cm^{-3}	300 g L^{-1}	>225 m^2 g^{-1}

To increase the surface area and the reaction potential between NO_x and the cementitious materials, crushed samples were produced from a cementitious plate. The plate was cast by first adding TiO_2 to deionized water (18.2 MΩ-cm) and mixing for 1 minute using a handheld electric mixer to facilitate dispersion. Then, cement was added to

the TiO_2 suspension and mixed for an additional 2 minutes. Cementitious plates were cast in plastic molds with dimension of 50.8 mm × 50.8 mm × 9.5 mm (width × length × height) and stored at 23 ± 2 °C in a doubly sealed bag to maintain high humidity and avoid carbonation. After 24 hours, the plates were removed from the molds and subsequently cured in sealed limewater at room temperature (23 ± 2 °C) for 28 days. After curing, the plates were conditioned at 23 ± 2 °C and 50 ± 5% relative humidity until reaching constant mass (i.e., less than 0.5 wt% change over a 6-hour period). The crushed samples were obtained by hand crushing the conditioned plate and sieving to obtain particles which passed the No.18 (1 mm) and were retained on the No. 30 (0.6 mm) sieves. Samples were stored in double sealed plastic bags prior to the microstructural analysis and NO_x photodegradation tests to avoid drying or carbonation.

6.2.2 Microstructural analysis

The specific surface area (SSA) and pore size distribution of the crushed samples were measured by N_2 adsorption and desorption prior to NO_x exposure. Approximately two grams of each sample were analyzed in a specific surface area gas analyzer (Micromeritics ASAP 2420). The crushed samples were degassed at 10 μmHg pressure for 12 hours prior to the analysis. The SSA was determined from the Brunauer, Emmett, Teller (BET) theory [118] using N_2 adsorption isotherm performed over a relative pressure range of 0.05 to 0.30. The pore size distribution was determined using the Barrett, Joyner and Halenda (BJH) method [119] on the data obtained from the desorption isotherm [101].

Although it has been noted that surface area measurements vary with technique, adsorbate, and sample preparation [120], the variation due to the sample preparation was minimized in this study by using a consistent experimental method and procedure, as described above, facilitating comparison among samples. In addition, the N_2 adsorption and desorption technique for obtaining SSA and pore size distribution has been commonly used for cementitious materials and can ensure semiquantitative comparisons of different cementitious materials [121].

6.2.3 NO_x photodegradation test setup

A schematic illustration of the NO_x photodegradation test setup is shown in Figure 6-1. The test was performed following procedures in the ISO 22197 [46] and JIS R 1701 Standards [47]. Two grams (2.00 ± 0.01 g) of samples were placed in a borosilicate photoreactor, with both ends sealed with a filter and screw cap. As recommended by the aforementioned standards, the NO_x gas used in this study was prepared by mixing 1000 ppb nitric oxide gas in ultrapure dry air and passed through the chamber at a constant flow rate of 1 L/min. For the purpose of consistency, the NO_x in this study refers to this particular mixed gas. The reaction was conducted at 23 ± 2 °C and 50 ± 5% relative humidity. The sample-loaded reactor was placed under two 40 W UV fluorescent lamps (Damar Worldwide, Aurora, MO, USA) with peak emission at 365 nm. The UV light intensity at the sample surface was maintained at 10 W/m^2 by adjusting the distance between the UV light source and the samples, which reside on the bottom surface of the photoreactor. The initial gas concentration was kept at 1000 ppb before turning on the UV light. Once the gas

concentration stabilized (1-hour stabilization time), the UV light exposure started and continued for 5 hours. After the UV light was turned off, the gas concentration was allowed to re-stabilize for another hour. The gas concentration throughout the experiment was measured by a chemiluminescent $NO/NO_2/NO_x$ analyzer (Model 200A, Teledyne API, San Diego, CA, USA). The entire test setup was covered by a black light-blocking canvas to prevent ambient light from affecting the reaction.

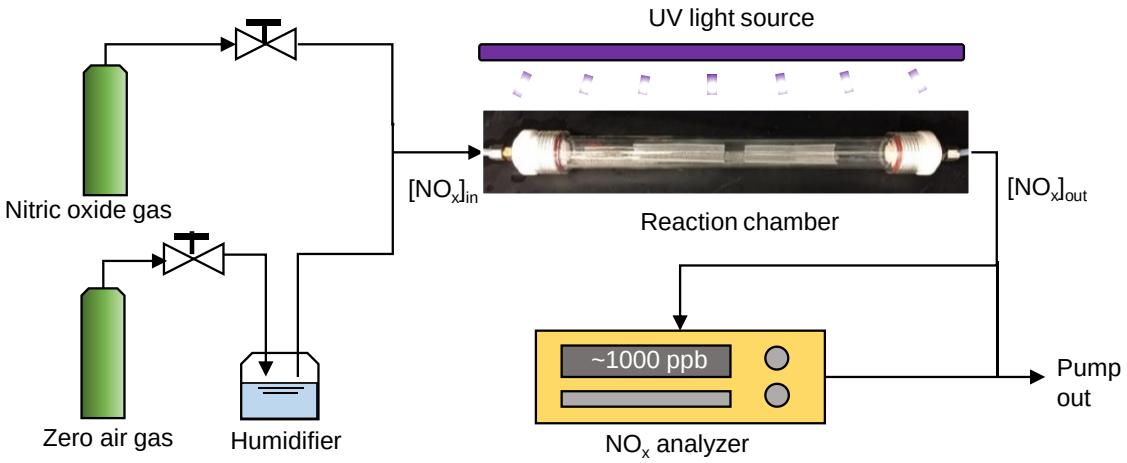

Figure 6-1: Experimental setup for NO_x photocatalytic degradation test.

6.2.4 Sample matrix

For each cement, six groups of experiments were conducted in triplicate, with varied sample composition and reaction conditions. Sample labels, test matrix, material composition, and exposure conditions for OPC and CAC samples are summarized in Table 6-3 and 6-4, respectively. For OPC samples, samples PB, PB-N and PB-V-N were control groups prepared with plain OPC (i.e. no TiO_2 doping), and samples PT, PT-N and PT-V-

N contained 5% TiO_2 by weight of OPC. For CAC samples, samples CB, CB-N and CB-V-N were control groups and samples CT, CT-N and CT-V-N were TiO_2-doped.

As outlined in both Table 6-3 and 6-4, both plain and doped samples were subjected to three exposure conditions: 1) without NO_x or UV exposure; 2) with NO_x but without UV exposure; and 3) with both NO_x and UV exposures. The samples subjected to condition 3 were exposed to NO_x and UV for five hours, plus one hour of stabilization time at the beginning and another hour for re-stabilization time at the end (see Section 2.3 for detailed exposure arrangement). The samples subjected to condition 2 were exposed to NO_x for a seven-hour period without UV (same period of NO_x exposure as condition 3). These exposure conditions and arrangements were selected to examine the individual and combined effects of NO_x exposure, UV exposure, and TiO_2 doping. At the end of each experiment, the samples were removed from the reactor and subjected to chemical extraction and nitrite and nitrate measurements within 24 hours.

6.2.5 Nitrite and Nitrate Measurements

The recovered samples were suspended in anoxic deionized water (purged by N_2 gas) in amber bottles to prevent further photo-induced reactions. Preliminary tests were conducted to determine the appropriate solid:liquid ratio (0.1 g in 10 to 100 mL), extraction time (4 hours to 1 week), and solvent (deionized (DI) water or KCl solution). A solid:liquid ratio of 0.1 gram in 40 mL DI water, and a 48-hour reaction time were selected for all experiments. Varying these parameters to facilitate extraction – such as increasing dilution or, increasing reaction time – produced no measurable increase in nitrite and nitrate

concentration, demonstrating the suitability of this method for full extraction. After the extraction, the suspension was filtered through a 0.45 μm syringe filter. The pH of the filtrate was measured by pH test strips (EMD chemicals) and was found to be around 10 for both OPC and CAC samples. The filtrate was then analyzed for both nitrite and nitrate concentrations.

Nitrite concentration was determined using a colorimetric assay kit (Roche, Sigma Aldrich) and measured at 540 nm on a UV-vis spectrometer (Cary 60, Agilent). Nitrate concentration was determined using ion chromatography (IC, Dionex). The IC is equipped with an Ionpac® AS14A column (4×250 mm) combined with an Ionpac® AG14A guard column (4×50 mm), and a Dionex ED40 electrochemical detector. The mobile phase contained 8 mM Na_2CO_3 and 1 mM $NaHCO_3$, and the flow rate was 0.8 mL/min.

6.2.6 Quantification of NO_x uptake and nitrite/nitrate formation

The nitrogen (N) mass of NO_x uptake (m_N) from the photodegradation test was compared with the total N mass from the nitrite (m_N') and nitrate (m_N'') measurements. The total amount of NO_x uptake throughout the photocatalytic process can be determined by Equation. 6.1-6.3. For the purpose of comparison, the specific NO_x uptake (normalized by sample mass) is used in this study, with a unit of mg N per kg solid (denoted as mg/kg for simplicity).

$$Q_N = \frac{f}{V}\int_0^T (C_{[NO_x]_{uptake}})\, dt \qquad (6.1)$$

$$C_{[NO_x]_{uptake}} = C_{[NO_x]_{in}} - C_{[NO_x]_{out}} \quad (6.2)$$

$$m_N = Q_N \times M_N \quad (6.3)$$

where Q_N = the amount of N uptake that is measured by the NO_x analyzer (mol), $C_{[NO_x]_{uptake}}$ = uptake concentration of NO_x (ppb), $C_{[NO_x]_{in}}$ = inlet concentration of NO_x (ppb), $C_{[NO_x]_{out}}$ = outlet concentration of NO_x (ppb), t = time of NO_x absorption (min), T = the duration of the photocatalytic process (300 min), f = flow rate of NO_x at 23 °C and 1.01 kPa (L min^{-1}),V= 24.3 L (the volume of 1 mole ideal gas at 23 °C and 1.01 kPa),m_N = the mass of N uptake(mg/kg), and M_N = the molar mass of N = 14 g/mol.

The N mass from nitrite and nitrate measurements is determined by Eq 6.4-6.7:

$$m_{NO_2^-} = C_{NO_2^-} \times DF \quad (6.4)$$

$$m_{NO_3^-} = C_{NO_3^-} \times DF \quad (6.5)$$

$$m'_N = m_{NO_2^-} \times \frac{M_N}{M_{NO_2^-}} \quad (6.6)$$

$$m''_N = m_{NO_3^-} \times \frac{M_N}{M_{NO_3^-}} \quad (6.7)$$

where $m_{NO_2^-}$ = the mass of nitrite (mg/kg), $m_{NO_3^-}$ = the mass of nitrate (mg/kg), $C_{NO_2^-}$ = the concentration of nitrite measured by UV-vis (ppm), $C_{NO_2^-}$ = the concentration of nitrate measured by IC (ppm), DF = dilution factor used for wet chemical extraction (400 for all samples), m'_N = the mass of nitrogen from nitrite (mg/kg), m''_N = the mass of nitrogen from

nitrate (mg/kg), $M_{NO_2^-}$ =the molar mass of nitrite = 46 g/mol, and $M_{NO_3^-}$ =the molar mass of nitrate = 62 g/mol.

6.3 Results and discussion

Using a variety of characterization methods, the influence of exposure conditions and specific surface area analysis (as influenced by nanoparticle addition) on the photocatalytic performance of controlled and TiO_2-doped samples was assessed in terms of NO_x uptake and transformation. UV-vis spectrophotometry and ion chromatography were used to measure the concentration of nitrite and nitrate ions, respectively. The total nitrogen detected from the independent nitrite and nitrate measurements was compared with the total nitrogen uptake measured from photocatalytic degradation to validate the test methods. NO_x uptake can be examined individually by comparing the TiO_2-doped and control samples while considering that the samples were exposed to three different conditions: the influence of NO_x exposure, UV exposure, and TiO_2 inclusion. Assessed together these data provide new insights into the role of the photocatalyst and the substrate in NO_x binding and quantify the relative formation of nitrite and nitrates formed in these systems. In this section, the OPC and CAC systems will be presented separately in below.

6.3.1 OPC samples

6.3.1.1 Microstructural properties

The measured specific surface area (SSA) was 10.23±0.98 m^2/g for the plain OPC samples (PB) and 16.90±0.06 m^2/g for the TiO_2-doped OPC samples (PT) after 28 days of hydration. The SSA is increased by 65% due to the TiO_2 addition. The pore size distribution profiles of the PB and PT samples (Figure 6-2) show larger amounts of very small pores (<5 nm) in Sample PT. According to Section 3.3.1, the early age hydration of OPC was found to be accelerated due to nucleation and growth effects induced by any TiO_2 addition, but the TGA and XRD results from Section 3.3.2 indicated the formation of the hydration products was found to be the same after 28 days of curing, regardless of TiO_2 addition. Therefore, the higher SSA and greater amount of micropores should only be attributed to the inclusion of TiO_2 nanoparticles, which possess an intrinsically high SSA larger than 225 m^2/g (Table 6-2). The relationship between the microstructural property and NO_x uptake will be further discussed in Section 6.3.1.3.

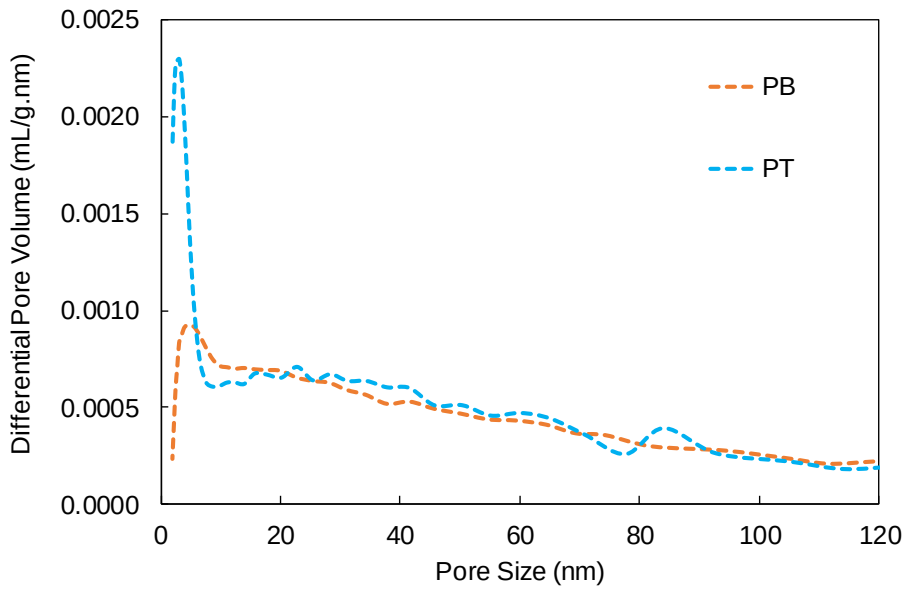

Figure 6-2: Pore size distribution of plain OPC (PB) and 5% TiO_2-doped OPC (PT) samples.

6.3.1.2 NO_x uptake

The result of the NO_x photodegradation test during the UV-irradiation period for Sample PT-N-V (TiO_2-doped OPC exposed to both NO_x and UV) is shown in Figure 6-3, where an instantaneous drop of NO_x concentration occurred upon UV illumination. This photodegradation of NO_x continued throughout the 5-hour test period, but at a decreasing rate. This phenomenon agrees with findings by other researchers [34,37,122]. When the UV light was turned off, NO_x concentration returned to the initial value. The total N mass of NO_x uptake (m_N) is denoted by the shaded region in Figure 6-3 and calculated to be 25.82±0.57 mg/kg.

The NO_x uptake by cement-based materials can be considered to occur via a two-step process: (1) the conversion of NO_x to nitrite and nitrate and (2) the binding of formed N species with cement paste. The difference in NO_x uptake is related to the differences in microstructural features (i.e. SSA and pore size distribution) and the photocatalytic activity induced by TiO_2 addition. These factors can be examined independently by comparing results among sample groups.

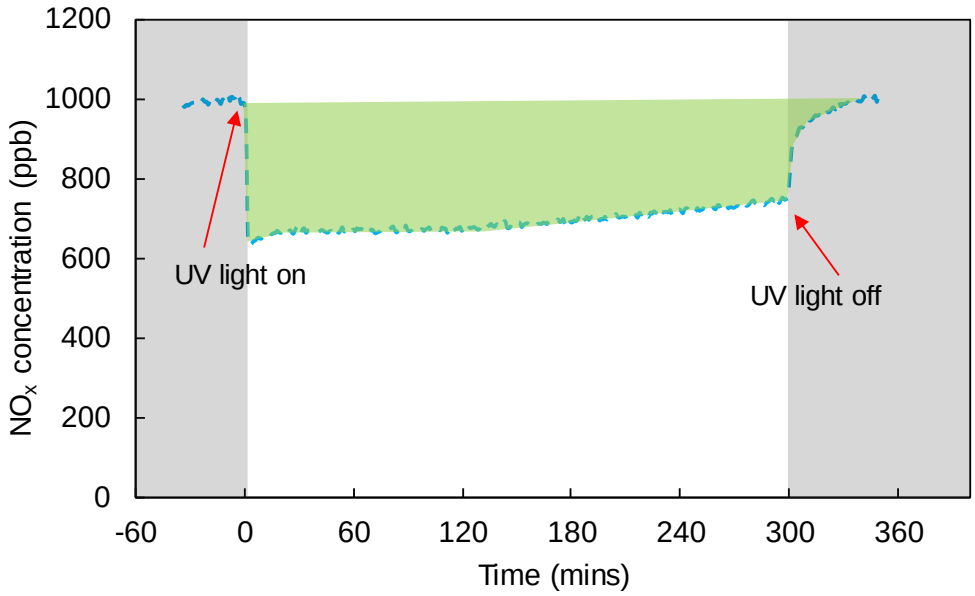

Figure 6-3: Photodegradation of crushed TiO_2-modified OPC samples that are exposed to NO_x and UV light (PT-N-V). The green shaded area represents the total NO_x uptake.

6.3.1.3 Nitrite and nitrate formation

The N masses from nitrite and nitrate measurements are listed in Table 3. The N mass of nitrite and nitrate formation due to photocatalytic reactions can be estimated by the difference between Sample PT-N and PT-N-V. The N mass present in nitrite form (m'_N) is 11.20±0.42 mg/kg and in nitrate form (m''_N) is 14.18±3.70 mg/kg. The total N mass in nitrite and nitrate combined ($m'_N + m''_N$) is 25.38±3.73 mg/kg. Therefore, a mass balance is achieved with total N mass in NO_x uptake during the photocatalytic process falling within the margin of error for the total N mass presented in nitrite and nitrate ($m_N \cong m'_N + m''_N$).

Table 6-3: Summary on the test matrix, material composition, exposure conditions, and measured concentration of nitrogen in the forms of nitrite and nitrate for OPC samples.

Group ID*	OPC	5% TiO_2	Exposure Condition		Mass of Nitrogen (mg/kg)	
			NO_x	UV	Nitrite Detection	Nitrate Detection
PB	×				BDL	BDL
PB-N	×		×		2.77 ± 0.09	5.83 ± 0.55
PB-N-V	×		×	×	2.78 ± 0.02	5.66 ± 0.45
PT	×	×			BDL	BDL
PT-N	×	×	×		5.80 ± 0.22	8.08 ± 1.77
PT-N-V	×	×	×	×	16.99 ± 0.35	22.26 ± 3.25

* Sample ID: P – OPC, B – plain cement pastes without TiO_2, T- 5% TiO_2 inclusion, N – samples under NO_x exposure, and V – samples under UV radiation. For example, PT-V-N indicates TiO_2-doped OPC samples that are exposed to both NO gas and UV light; BDL: below detection limit, which is 1.20 mg/kg for NO_2^- and for 4.50 mg/kg for NO_3^-.

For the plain OPC samples that are exposed to NO_x (PB-N and PB-N-V), both nitrite and nitrate are detected after exposure. As shown in Table 6-3, similar amounts of nitrite and nitrate are measured regardless of the presence of UV light. Therefore, the mechanism of converting NO_x to nitrite and nitrate by plain OPC is unlikely to be photocatalytic.

The mechanism of NO_x conversion to nitrite and nitrate should be related to heterogeneous catalytic reactions on the surface of hydrated cements. Researchers have demonstrated these reactions of NO_x on many different hydrated mineral surfaces [123–125]. For example, Grassian [123] showed that NO_x reacts on the surface of hydrated SiO_2 particles (particles exposed to water overnight) but not on dehydrated SiO_2 particles (particles evacuated overnight). The detection of nitrite and nitrate in this study suggests that the complex surfaces of hydrated cementitious materials with their monolayers of water and pore-solution containing nanopores can also facilitate these heterogeneous catalytic reactions.

$$NO + NO_2 + H_2O \rightarrow 2\,HNO_2 \qquad (6.8)$$

$$2\,NO_2 + H_2O \rightarrow HNO_2 + HNO_3 \qquad (6.9)$$

Due to the presence of alkaline pore solution in cementitious environment, the formed nitrous and nitric acids are transformed to nitrite and nitrate through the following reaction:

$$HNO_2 + OH^- \rightarrow NO_2^- + H_2O \qquad (6.10)$$

$$HNO_3 + OH^- \rightarrow NO_3^- + H_2O \qquad (6.11)$$

Horgnies et al. [126] also observed decreased NO_x levels in the presence of conventional plain concrete and suggested that the high alkalinity in the cementitious environment also played an important role in NO_x conversion to nitrite and nitrate. Their proposed reactions with hydroxyls are as below, which is essentially the same as the combined Equations. 6.8-6.10:

$$NO + NO_2 + 2\,OH^- \rightarrow 2\,NO_2^- + H_2O \qquad (6.12)$$

$$2\,NO_2 + 2\,OH^- \rightarrow NO_2^- + NO_3^- + H_2O \qquad (6.13)$$

The previous studies also suggested that the heterogeneous surface catalytic reactions could be accelerated by a high surface area, which relates to surface roughness, amount of micropores, and particle size [123–125]. This is also evidenced in this study by examining samples that are only exposed to NO_x (PB-N and PT-N), but with different SSA and amount of micropores. For Sample PT-N, the increase in NO_x uptake can be associated with the effect of the TiO_2 addition on increased SSA and the amount of micropores with a size of less than 5 nm (Figure6-2). Lee et al [116] have also observed similar results indicating that a greater degree of NO_x degradation was achieved in TiO_2-doped cement pastes with a larger SSA. They have also suggested that the greater amount of micropores could also help hold more alkaline pore solution, which in turn could accommodate more nitrite and nitrate. Therefore, the NO_x uptake can be directly related to the microstructural features of cementitious materials.

Although the above studies have demonstrated the heterogeneous surface catalytic reactions in Sample PB-N and PT-N, none of them quantified the NO_x uptake. This information is critical to understand the intrinsic NO_x sequestration capability of cementitious materials and can be used to remediate NO_x emissions resulting from their own production. This study quantifies the amount of NO_x uptake by measuring the concentration of nitrite and nitrate. The results are listed in Table 6-3. The concentration of both nitrite and nitrate in Sample PT-N increases compared to PB-N. The total N mass of NO_x uptake of PT-N is increased by 65% compared to PB-N. This increase coincides with the increase of SSA measured in Section 3.1. The increase in the nitrite is about 110% while the increase in nitrate is about 30%. This difference leads to a change of the

nitrite:nitrate concentration ratio from 1:2 in Sample PB-N to 1:1.3 in Sample PT-N. As discussed in Section 6.3.1.1, the higher SSA and greater amount of micropores in Sample PT-N induced by TiO_2 addition indicates higher surface area and porosity intrinsic to the TiO_2 nanoparticles. Therefore, the increase of total NO_x uptake and larger increase of nitrite could be related to the increased amount of and more dispersed C-S-H and its different interaction with nitrite and nitrate. Again, the microstructural features, including SSA and pore size distribution, could be used as indicators to design cementitious materials for optimized NO_x uptake.

The total amount of NO_x uptake is increased by 360% in TiO_2-doped OPC that is exposed to NO_x and UV light (PT-N-V) compare to the plain OPC samples (PB-N-V). The increased NO_x uptake is related to both the microstructural differences and activation of photocatalytic activity induced by TiO_2 addition. The effects of microstructural features of cementitious materials on NO_x uptake have been discussed in the previous section.

The highest increase in NO_x uptake found in Sample PT-N-V is mainly due to the photocatalytic activities, which increase the conversion of NO_x to nitrite and nitrate ions and subsequently NO_x uptake. The relative amounts of nitrite and nitrate from the photocatalytic process alone (i.e., neglecting binding by the cementitious material itself) can also be determined by comparing Samples PT-N and PT-N-V. The results are provided in Table 6-3. Approximately half of the NO_x uptake is converted into nitrite during photocatalytic reactions, and the other half into nitrate. The higher NO_x uptake found in Sample PT-N-V (360%) compared to Sample PT-N (65%) also indicates that the photocatalytic activity has a greater effect on NO_x uptake than the microstructural differences associated with TiO_2 introduction.

6.3.2 CAC samples

6.3.2.1 Microstructural properties

The measured SSA was 16.68±0.29 m^2/g for the plain CAC samples (CB) and 21.33±0.35 m^2/g for the TiO_2-doped CAC samples (CT) after 28 days of hydration. The SSA is increased in CAC samples by 28% due to the TiO_2 addition. Similar as OPC samples, the pore size distribution profiles of the CB and CT samples (Figure 6-4) show larger number of small pores in Sample PT. Again, the higher SSA and greater amount of micropores should only be attributed to the inclusion of TiO_2 nanoparticles since according to Section 3.3.2, the TGA and XRD results show that the formations of the hydration products are the same for plain and 5% TiO_2-doped CAC after 28 days of curing, regardless of TiO_2 addition.

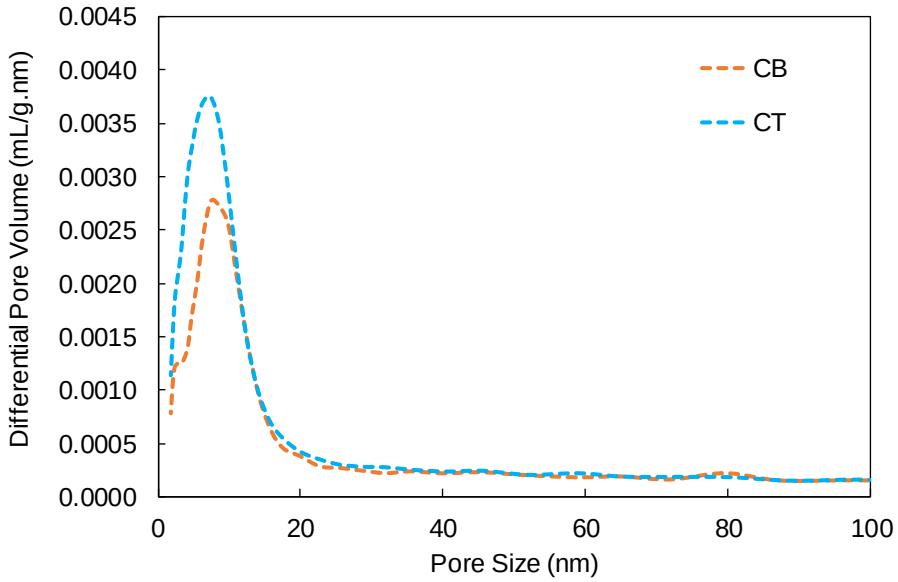

Figure 6-4: Pore size distribution of plain CAC (CB) and 5% TiO_2-doped CAC (CT) samples.

6.3.2.2 NO_x uptake

The NO_x photodegradation of Sample CT-N-V (crushed TiO_2-modified CAC samples that are exposed to NO_x and UV) is illustrated in Figure 6-5. The NO_x concentration was kept constant before the UV light was illuminated. An almost instantaneous drop of NO_x concentration occurred upon initial UV illumination, resulting in the maximal decrease in NO_x concentration. Similar to OPC samples, the photocatalytic reactions continued throughout the 5-hour test period with a photodegradation efficiency also decreasing during the test period. When the UV light was off, the NO_x concentration recovered to the initial level. Based on Equation 6.1-6.3, the N mass of total NO_x uptake (m_N) denoted as shaded area, is 28.4 ± 0.63 mg kg^{-1}.

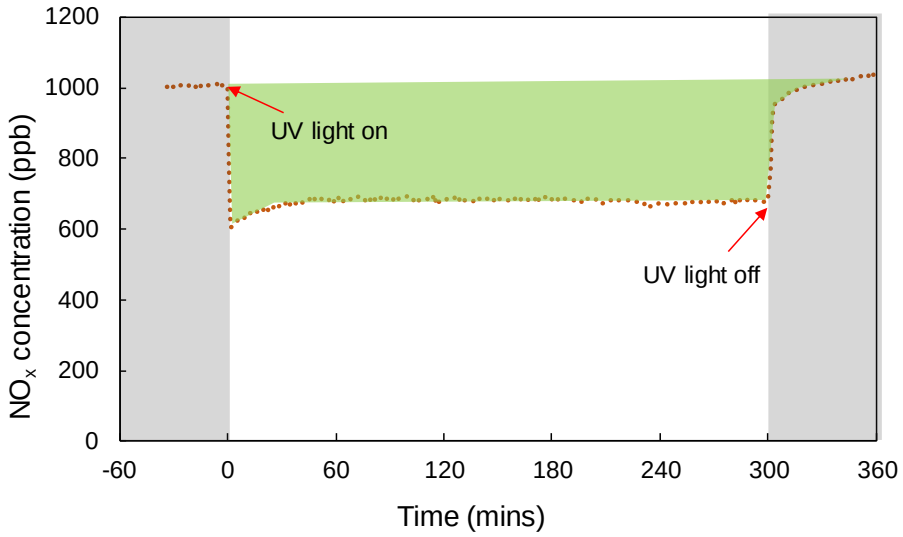

Figure 6-5: Photodegradation of crushed TiO_2-modified CAC samples that are exposed to NO_x and UV light (CT-N-V). The green shaded area represents the total NO_x uptake.

6.3.2.3 Nitrite and nitrate formation

The N masses measured by NO_2^- and NO_3^- detection are listed in Table 6-4. The samples without NO_x or UV exposure (CB and CT) show no measurable formation of NO_2^- or NO_3^-, as expected. Both NO_2^- and NO_3^- are detected in the plain CAC samples (CB-N and CB-N-V) after NO_x exposure. Comparing CB-N with CB-N-V, similar amounts of N mass for both NO_2^- and NO_3^- detections are observed regardless of the presence of UV light. Compared to OPC samples, the detected NO_2^- and NO_3^- in CAC samples are higher and this could be attributed to the higher surface area of CAC samples. The mechanism of the cementitious materials' intrinsic capability of converting NO_x into NO_2^- and NO_3^- without photocatalytic reactions can be found 6.3.1.3. That mechanism can be summarized in three aspects: (i) the surface-related heterogeneous reactions, which promote the conversion of NO_x into NO_2^- and NO_3^- and can be facilitated by the monolayers of water and pore-solution containing pores in the cementitious materials [123]; (ii) the surface area, the higher of which can help accelerate the aforementioned heterogeneous reactions [123–125]; and (iii) the presence of an alkaline environment in cementitious materials, where hydroxyls can react with NO_x and form NO_2^- and NO_3^- ions [126].

Interestingly, similar amounts of N mass of NO_2^- and NO_3^- detections are observed in the TiO_2-modified CAC samples (CT-N and CT-N-V) regardless of the presence of UV light. This suggests that only a certain amount of the converted NO_2^- and NO_3^- are susceptible to water-based wet chemical extraction and can be detected by ultraviolet-visible spectrophotometry and ion chromatography. Among these NO_2^- and NO_3^-, the nitrite-to-nitrate concentration ratio for both the controlled (CB) and TiO_2-modified (CT) samples is approximately 1:1.3, suggesting that the surface-related heterogeneous reactions

converted more NO_x to nitrate than to nitrite in CAC systems. This ratio is similar to that found in OPC systems. Both NO_2^- and NO_3^- concentrations are higher in the CT samples than in the CB samples (Table 6-4). This result is expected since the addition of TiO_2 nanoparticles with specific surface areas of >225 m^2/g helps increase the surface area of the CT samples, which in turn promotes the surface-related heterogeneous reactions. Compared to CB, both the NO_2^- and the NO_3^- concentrations of the CT samples are increased by approximately 28%, which also agrees with the increase in SSA.

The formation of NO_2^- and NO_3^- in Sample CT-N-V should be related to both heterogeneous and photocatalytic reactions since the photocatalytic reactions are activated by the presence of UV light. Therefore, the N mass of measured NO_2^- and NO_3^- through photocatalytic reactions can be estimated by the difference between CT-N and CT-N-V and is found to be zero based on the results in Table 6-4. This finding contradicts the finding that the N mass of total NO_x uptake found in Section 6.3.2.2, which is about 28.4 mg kg^{-1}. The imbalance between the N mass of measured NO_2^- and NO_3^- and that of NO_x uptake suggests that the formed NO_2^- and NO_3^- cannot be detected by the experimental approach using water-based wet chemical extraction. Since this mass balance has been achieved in OPC samples using the exact same experimental design and procedure, the undetectable NO_2^- and NO_3^- in CAC samples suggests that the additional converted NO_2^- and NO_3^- through photocatalytic reactions could be chemically bound with hydrated CAC phases and resistant to releasing NO_2^- and NO_3^- in aqueous solution.

This phenomenon coincides with the novel pathway proposed by Sant et al [76] to sequester NO_2^- and NO_3^- permanently in cements by using an “anion exchange” process. They presented the formation of aluminum-bearing phases (AFm and AFt) in the CAC

systems that possess an exchangeable interlayer anions of sulfate (SO_4^{2-}) and hydroxyl (OH^-) [127]. Thermodynamically, these anions, along with NO_2^- and NO_3^-, have an occupation preference with a ranking of $NO_3^->NO_2^->SO_4^{2-}>OH^-$ [128]. Therefore, the undetected NO_2^- and NO_3^- produced in the photocatalytic process in this study could likely substitute the interlayer SO_4^{2-} or OH^- and be chemically bound with the aluminate-bearing phases in CAC system. This anion exchange process in aluminum-bearing phases have also been experimentally demonstrated by Balonis et al. [129], where NO_2^- and NO_3^- substituted SO_4^{2-} in AFm phases and formed AFm-NO_2/NO_3.

In addition, these sequestrated NO_2^- and NO_3^- ions also helps enhance the sustainability and durability of CAC-based concrete infrastructure. As discussed in Chapter 2, NO_2^- and NO_3^--containing compounds are often used at the steel interface to improve the corrosion resistance of steel-reinforced concrete, where chlorides (Cl^-) can be fixed in these aluminate-bearing phases through the aforementioned anion exchange process [129]. This finding suggests an additional pathway to enhance the inhibition of chloride-induced steel corrosion, which in turn can prolong the service life of CAC-based concrete infrastructure containing TiO_2 photocatalysts.

Table 6-4: Crushed samples: sample matrix, material composition, exposure condition, and measured concentration of nitrogen in the forms of nitrite and nitrate of CAC samples.

Sample ID*	Material		Exposure Condition		Mass of Nitrogen (mg/kg)	
	CAC	5% TiO_2	NO_x	UV	NO_2^- detection	NO_3^- detection
CB	×				BDL	BDL
CB-N	×		×		6.37 ± 0.26	9.13 ± 0.66
CB-N-V	×		×	×	6.60 ± 0.65	9.69 ± 0.38
CT	×	×			BDL	BDL
CT-N	×	×	×		8.63 ± 0.42	11.15 ± 0.36
CT-N-V	×	×	×	×	8.83 ± 0.57	11.67 ± 1.13

* CB: plain CAC samples without TiO_2; CT: CAC samples with 5% TiO_2 inclusion; N: samples only exposed NO_x; NV: samples exposed to both NO_x and UV; and BDL: below detection limit, , which is 1.20 mg/kg for $NO_2^-$and for 4.50 mg/kg for NO_3^-.

6.4 Conclusion

The NO_x uptake for both plain and TiO_2–doped cementitious samples are compared in this study. Both OPC-based and CAC-based samples are examined. Because NO_x is converted to nitrite and nitrate ions on the material surface, a combination of wet chemical extraction, UV-vis spectrophotometry and ion chromatography methods were developed to quantify the concentrations of nitrite and nitrate that are bound within the hydrated cement paste. The effects of microstructural properties and photocatalytic reactions on NO_x uptake are examined. The conclusions are given below.

Similar NO_x uptake is observed in both plain OPC and CAC samples regardless of the presence of UV light, demonstrating that cement-based materials have the intrinsic capability to sequester NO_x even in the absence of photocatalysts. The NO_x sequestration capability of ordinary unmodified cementitious materials can help policy makers develop new strategies of remediating atmospheric NO_x by taking advantage of the NO_x sequestration capability of existing cement-based infrastructure, such as using it to remediate NO_x emissions resulting from the production and construction of cementitious materials themselves.

The mechanism of NO_x conversion into nitrite and nitrate in samples that are only exposed to NO_x is related to the surface catalytic reactions in the cementitious environment. The addition of TiO_2 nanoparticles increases SSA and the amount of micropores in both OPC and CAC cementitious systems, and, in turn, increases the potential for NO_x uptake for both cements. The alkalinity in the cementitious environment also plays an important role in NO_x conversion. With the TiO_2 addition, the concentration ratio between nitrite and

nitrate changes from 1:2 to 1:1.3 in TiO_2-doped OPC samples but the concentration ratio maintains 1:1.3 in CAC samples. The different nitrite:nitrate ratio in different cementitious materials should be related to the differences in their chemical composition and microstructural properties. Nevertheless, this chapter has demonstrated that the microstructural features, including SSA and pore size distribution, can be used as indicators for designing cementitious materials for optimized NO_x uptake.

For TiO_2-doped OPC samples that are exposed to both NO_x and UV, the total NO_x uptake increases by 360%, compared to the plain OPC sample under the same exposure conditions. The increase is attributed to the microstructure differences and activation of photocatalytic reactions induced by TiO_2 nanoparticles. By comparing the TiO_2-doped OPC samples with and without UV light exposure, a mass balance is achieved between the total NO_x uptake and nitrite and nitrate formation. In addition, this comparison also provides the evidence that the NO_x uptake is more greatly influenced by the photocatalytic activity than the microstructural changes associated with TiO_2 introduction.

For TiO_2-doped CAC samples that are exposed to both NO_x and UV, the N mass of NOx uptake through photocatalytic reactions cannot be balanced with N mass from nitrite and nitrate detection. The results indicate that the produced nitrite and nitrate in CAC system could be potentially less susceptible to water-based chemical extraction and hence they cannot be detected by either UV-vis spectrophotometry or ion chromatography. Since OPC and CAC have different chemical compositions and hydration phases, as described in Chapter 2, this finding warrants a more comprehensive study on NO_x sequestration in pure cementitious phases, which will be included in the next chapter.

CHAPTER 7. EXAMINATION OF NO_X UPTAKE IN PURE CEMENTITIOUS PHASES

7.1 Introduction

Chapter 6 has quantified the NO_x sequestration capacities of plain and TiO_2-modified cementitious materials, demonstrating that the cement-based materials when designed properly can serve as a potential nitrogen sink. The NO_x uptake in these cement pastes is a two-step process: (1) the conversion of NO_x to nitrite (NO_2^-) and nitrate (NO_3^-), and (2) the binding of NO_2^- and NO_3^- within their cementitious phases. As discussed in Chapter 6, the NO_x conversion mechanism (Step 1) can be summarized in three aspects:

(i) Photocatalytic reactions, which are activated by TiO_2 photocatalysts exposed to NO_x and UV light, and convert NO_x into NO_2^- and NO_3^-.

(ii) Surface-related catalyzed heterogeneous reactions, which promote the conversion of NO_x into NO_2^- and NO_3^- and can be facilitated by the monolayers of water on the material's surface and the pore-solution-containing pores in the cementitious materials. These reactions can be accelerated by increased surface area resulting from the addition of TiO_2 nanoparticles.

(iii) Reaction with hydroxyls, due to the alkaline environment in cementitious materials. NO_x can react with the hydroxyls present in the pore solution in the cementitious environment and transform to nitrite and nitrate.

However, the binding mechanisms (Step 2), which are essential pathways for NO_x sequestration, remain elusive. For example, it is unclear whether NO_x is chemically bound within the cementitious material as one or multiple N-containing cementitious species, or whether it is physically bound within the cementitious matrix, such as adsorbing onto the surface of cementitious hydrates or dissolving in pore solution. A better understanding on the roles of different hydrated cement phases and related reactions in the overall NO_x uptake/transformation process is necessary for the design and selection of cementitious materials with the desired properties and chemical compositions for optimal NO_x sequestration.

This chapter investigates the NO_x uptake of individual phases found in hydrated cement in order to understand the mechanisms and pathways for NO_x sequestration in cement-based materials. Three pure cementitious phases are synthesized, including calcium silicate hydrates (C-S-H), portlandite ($Ca(OH)_2$), and monosulfoaluminate (AFm-SO_4), and each are exposed to NO_x gas in an instrumented and closed plug-flow reactor. When cement-based materials are placed into service, they are exposed to the environment, and as a result of long-term interactions with CO_2, the hydrated cementitious phases could become carbonated. Researchers have raised some concerns in NO_x sequestration when the materials are carbonated, especially for TiO_2-modified photocatalytic cements [52]. Therefore, to investigate the effect of carbonation on the pathway of NO_x sequestration, two carbonated phases are also examined in this chapter. Here, calcite ($CaCO_3$) from the carbonation of $Ca(OH)_2$ and monocarboaluminate carbonates (AFm-CO_3) from the carbonation of AFm phases are examined. To quantify the NO_x sequestration capacity and understand the NO_x binding mechanism for each cementitious phase, the same

characterization method that is developed in Chapter 6 is employed, combining wet chemical extraction, ultraviolet-visible spectrophotometry, and ion chromatography. In addition, X-ray diffraction (XRD) is also used to further examine the reaction mechanism and identify changes in chemical composition during NO_x exposure.

7.2 Experimental methods

7.2.1 Materials

C-S-H was synthesized from 5 grams of triclinic alite (C_3S) and 1.53 grams of silica fume. C_3S was obtained from Mineral Research Processing (Meyzieu, France) and its purity was determined by quantitative XRD using the Rietveld method to be 95±1.5%. The silica fume was obtained from Alfa Aesar (Ward Hill, MA, USA) with stated purity exceeding 95% and surface area of 300-350 m^2/g. The amounts of alite and silica fume were selected based on stoichiometry used in literature with C/S ratio of approximately 1.7 [105]. The overall sample preparation procedure was adopted from previous studies [130,131] and as detailed below. Silica fume was first suspended in 250 grams of degassed deionized water (18 MΩ·cm) and stirred for three minutes to ensure an even distribution. Alite were then added to the silica suspension and stirred at 23±2 °C for a week, during which the entire setup was sealed to avoid carbonation. The water-to-solid ratio is about 50 by weight to ensure a complete reaction of alite and silica fume and to prevent the formation of calcium hydroxide as a reaction byproduct. After mixing, the sample was filtered using Whatman grade 1 filter paper and vacuum dried at 23±2 °C and stored in a

doubly sealed inert high-density polyethylene (HDPE) bottle prior to NO_x exposure tests and XRD analysis.

AFm-SO_4 and AFm-CO_3 were synthesized according to the protocol developed by Matschei [132]. AFm-SO_4 was prepared by mixing C_3A (its preparation is in the next paragraph) and $CaSO_4$ in a 1:1 molar ratio in boiling deionized water with water/solid mass ratio of around 20. The slurry was then stirred at 85 °C for two weeks in a sealed polytetrafluoroethylene (PTFE) bottle prior to filtration with Whatman grade 1 filter paper and vacuum-drying. AFm-CO_3 was prepared by mixing C_3A and $CaCO_3$ in a 1:1 molar ratio at 23±2 °C with water/solid mass ratio of around 20. The mixture was stirred in PTFE-bottles for two weeks prior to filtration and vacuum-drying.

Pure C_3A was prepared by combining analytical-reagent-grade $CaCO_3$ and Al_2O_3 in a 3:1 molar ratio. The powders were dry-mixed, homogenized, and pressed into pellets using a steel die at a pressure of 10 MPa. The pellets were placed in zirconia grain-hardened platinum crucibles and sintered at 1450 °C in a muffle furnace for a 24-hour period. At the end of the sintering routine, the pellets were air-quenched. The pelletized, sintered material was finely ground and pelletized once again, and the sintering routine repeated two more times. After preparation, the C_3A was stored in a doubly sealed HDPE bottle at 23±2 °C until its time of use.

The synthetic $Ca(OH)_2$ was reagent grade and was purchased from Acros, Thermo Fisher Scientific (Pittsburg, PA, USA) with a stated purity exceeding 98%. The synthetic $CaCO_3$ was also reagent grade and purchased from Alfa Aesar (Ward Hill, MA, USA), with a stated purity exceeding 99 %.

7.2.2 NO_x exposure

The test setup of the NO_x exposure test was developed in Chapter 6 and was based on ISO 22197 [46] and JIS R 1701 Standards [47] for air purification performance of photocatalytic ceramic materials, as shown in Figure 6-1. One gram (1.00 ± 0.01 g) of synthetic powder sample was placed in weighing boats, which resided on the bottom surface of a borosilicate photoreactor, with both ends sealed with a filter and screw cap. As recommended by the aforementioned standards, the NO_x gas, comprising 1000 ppb nitric oxide gas with ultrapure dry air, passed through the photoreactor at a constant flow rate of 1 L/min. For $Ca(OH)_2$, the NO_x gas was prepared by comprising 1000 ppb nitric oxide gas with N_2 gas to prevent any potential carbonation during the exposure test. The reaction was conducted at 23 ± 2 °C and 50 ± 2% relative humidity by passing the gas through a humidifier. The samples were continuously exposed to NO_x gas for 5 hours and the gas concentration was kept at 1000 ppb, which was measured by a chemiluminescent $NO/NO_2/NO_x$ analyzer (Model 200A, Teledyne API). The entire test setup was covered by a black light-tight canvas to prevent ambient light from affecting the reaction. After NO_x exposure, samples were stored in double sealed plastic bags prior to nitrite/nitrate detection tests.

7.2.3 Nitrite and nitrate detection

The experimental method for detecting NO_2^- and NO_3^- is adopted from Chapter 6 and combines wet extraction, UV-vis spectrophotometry, and ion chromatography. The wet chemical extraction was performed by suspending NO_x-exposed synthetic powders in

anoxic deionized water, which was purged with N_2 gas for 48 hours, in HDPE bottles. A solid-to-liquid ratio of 0.1 gram in 40 mL deionized water was used. The HDPE bottles were wrapped in aluminum foil to prevent ambient light from affecting the reaction. All bottles were placed on a shaker at 150 rpm for 48 hours. After the extraction, the suspension was filtered through a 0.45 μm syringe filter and the filtrate was then analyzed for both nitrite and nitrate concentrations. Nitrite concentration was determined using a colorimetric assay kit (Roche, Sigma Aldrich, St. Louis, MO, USA) and measured at 540 nm on a UV-vis spectrometer (Cary 60, Agilent, Santa Clara, CA, USA). Nitrate concentration was determined using an ion chromatography unit (Dionex, Sunnyvale, CA), equipped with an Ionpac® AS14A column (4×250 mm) combined with an Ionpac® AG14A guard column (4×50 mm), and a Dionex ED40 electrochemical detector. The mobile phase used of IC contained a mixture of 8 mM Na_2CO_3 and 1 mM $NaHCO_3$, and the flow rate was 0.8 $mLmin^{-1}$.

The nitrogen (N) mass, which was used to represent the measured nitrite and nitrate masses, was determined using the following equations.

$$m_{NO_2^-} = C_{NO_2^-} \times DF \quad (7.1)$$

$$m_{NO_3^-} = C_{NO_3^-} \times DF \quad (7.2)$$

$$m'_N = m_{NO_2^-} \times \frac{M_N}{M_{NO_2^-}} \quad (7.3)$$

$$m''_N = m_{NO_3^-} \times \frac{M_N}{M_{NO_3^-}} \quad (7.4)$$

where $m_{NO_2^-}$ = the mass of nitrite (mg kg^{-1}), $m_{NO_3^-}$ = the mass of nitrate (mg kg^{-1}), $C_{NO_2^-}$ = the concentration of nitrite measured by UV-vis spectrometer (ppm), $C_{NO_2^-}$ = the concentration of nitrate measured by ion chromatography (ppm), DF = dilution factor used for wet chemical extraction (400), m'_N = the mass of nitrogen from nitrite (mg kg^{-1}), m''_N = the mass of nitrogen from nitrate (mg kg^{-1}), $M_{NO_2^-}$ =the molar mass of nitrite = 46 g mol^{-1}, and $M_{NO_3^-}$ =the molar mass of nitrate = 62 g mol^{-1}.

7.2.4 X-ray diffraction

XRD was performed on the synthetic cementitious phases before and after NO_x exposure and its pattern was used to identify changes in chemical composition and crystallinity during the NO_x exposure. For XRD analysis, approximately 0.2 grams of powders were packed into a sample holder, which was then placed into a PANalytical Empyrean X-ray diffractometer (Malvern Panalytical Ltd., Malvern, United Kingdom) with Cu-Kα (λ = 1.54 Å) radiation at 45 kV and 40 mA. Scans were performed at 5–45° 2θ using a PIXcel3D detector and analyzed with PANalytical HighScore Plus software.

7.3 Results and discussion

To understand the pathway of NO_x sequestration, quantify individual NO_x uptake capacity of each cementitious phase, and to investigate the effect of carbonation on the NO_x uptake, five pure phases – C-S-H, $Ca(OH)_2$, AFm-SO_4, $CaCO_3$, and AFm-CO_3 – common in cementitious materials were synthesized. NO_x uptake capacity was measured by a combination of wet chemical extraction, UV-vis spectrophotometry, and ion chromatography. The results are presented in terms of the N masses of measured NO_2^- and NO_3^- detections and listed in Table 7-1. The samples without NO_x exposure were also tested and showed no measurable formation of either NO_2^- or NO_3^-, which is expected. The results of XRD analysis for each phase before and after NO_x exposure are also provided. The binding mechanism for each cementitious phase can be determined with the collective results from NO_2^-/NO_3^- detection and XRD analysis.

Table 7-1: The measured N mass in the form of nitrite and nitrate concentrations for each phase

Materials	NO_x Exposure	N mass (mg/kg)	
		NO_2^- detection, m'_N	NO_3^- detection, m''_N
C-S-H		BDL	BDL
	×	53.32 ± 3.70	148.81 ± 16.28
$Ca(OH)_2$		BDL	BDL
	×	BDL	BDL
AFm-SO_4		BDL	BDL
	×	2.87 ± 0.56	BDL
$CaCO_3$		BDL	BDL
	×	14.36 ± 0.98	536.57 ± 2.55
AFm-CO_3		BDL	BDL
	×	27.36 ± 1.42	24.62 ± 2.80

* BDL: below detection limit, which is 1.20 mg/kg for $NO_2^-$and for 4.50 mg/kg for NO_3^-.

7.3.1 C-S-H

Among all "fresh" cementitious phases (without carbonation), C-S-H shows the highest NO_x uptake capacity with nitrite-N at approximately 50 mg/kg and nitrate-N 150 mg/kg (Table 1). The high level of NO_x uptake was expected because interlayer water molecules resides between the layers of C-S-H [105,133] and promotes heterogeneous catalytic reactions (conversion mechanism (ii)). Second, C-S-H has a high surface area that ranges from 10s to 100s m^2/g [105], which promotes the heterogeneous catalytic reactions (conversion mechanism (ii)). Intrinsic to the C-S-H structure are nanoscale pores containing pore solution [105,133], which suggests the potential for the formation of NO_2^- and NO_3^- ions (conversion mechanism (iii)). Therefore, this study supports the hypothesis put forth in Chapter 6 that C-S-H, with unique microstructural features that are favorable to NO_x conversion, plays a major role in sequestering NO_x in OPC-based cementitious materials. However, the nitrite-to-nitrate ratio is 1:3 for C-S-H in this Chapter while the ratio is 1:2 for plain OPC in Chapter 6 (Table 6-1). The higher ratio could be because isolated C-S-H phases were used in this Chapter.

In terms of the binding mechanism, NO_2^- and NO_3^- in the C-S-H phase likely adsorb on the surface of these cementitious phases [116] or dissolve in the pore solution [116] since the microstructural features of C-S-H provide suitable accommodations for these ions to bind in these two manners. Either way, these ions are susceptible to water-based wet chemical extraction and can be detected and quantified by UV-vis spectrophotometry, and ion chromatography. In addition, no new peaks were observed by XRD as shown in Figure 7-1, suggesting that the formation of new solid phases between C-S-H and NO_2^- and NO_3^-

ions is unlikely, and in turn supporting that the high NO_x uptake by C-S-H is largely a physical phenomenon.

In addition, to discern the relative significance of how these two factors, surface adsorption and dissolution in pore solution, a future study should be carried out to test these two mechanisms separately.

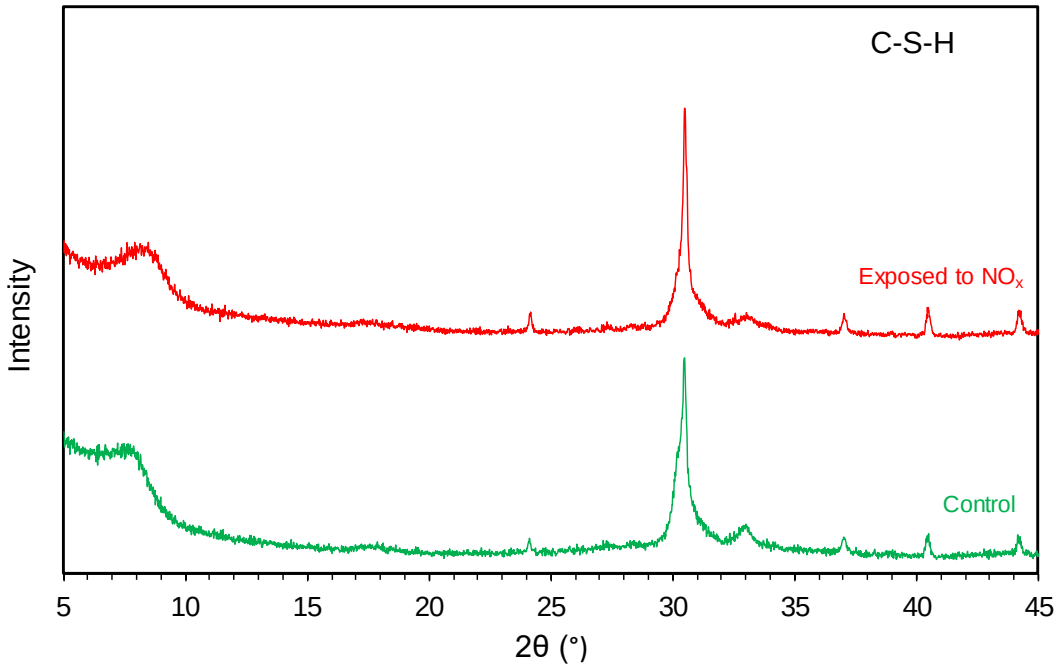

Figure 7-1: XRD patterns of synthetic C-S-H before (control) and after exposed to NO_x

7.3.2 $Ca(OH)_2$

The NO_x uptake capacity of synthetic $Ca(OH)_2$ was undetectable, and formation of new phases was not observed in XRD patterns (Figure 7-2). The result indicates that $Ca(OH)_2$ could be intrinsically resistant to NO_x sequestration based on the current experimental conditions.

Zhang et al [134] have demonstrated NO_x removal/absorption by $Ca(OH)_2$. They suggested that the nitrous and nitric acids could react with $Ca(OH)_2$ to form calcium nitrite and nitrate based on the following reactions:

$$Ca(OH)_2 + 2HNO_2 \rightarrow Ca(NO_2)_2 + 2H_2O \qquad (7.5)$$

$$Ca(OH)_2 + 2HNO_3 \rightarrow Ca(NO_3)_2 + 2H_2O \qquad (7.6)$$

As $Ca(NO_2)_2$ and $Ca(NO_3)_2$ are highly soluble, the resulting NO_2^- and NO_3^- ions should be detected through water-based wet chemical extraction. However, their experiments were performed under a temperature of 70 °C and relative humidity of 60% [134], which, as they described, makes nitrous and nitric acid close to liquid-phase steam. They also suggested that the overall absorption reactions could be affected by the combined effect of relative humidity, volume fraction of water in the gas, and temperature, but did not conduct any experiments at different temperatures [134]. Therefore, the gas-phase nitrous and nitric acids formed through conversion mechanism (ii) in this study may not able to react with $Ca(OH)_2$ under room temperature. Chen et al [135] showed a SO_2 and NO_x removal by $Ca(OH)_2$ and concluded that the presence of SO_2 could enhance the efficiency of NO_x removal. However, their test was also carried out at a high temperature (70 °C) with $Ca(OH)_2$ slurry that was pre-treated with water at H_2O/CaO ratio of 5 [135]. Therefore, the inability of $Ca(OH)_2$ to sequester NO_x in this study likely related to low temperature and humidity, which represent the real field situation for cement-based concrete infrastructure.

When both C-S-H and $Ca(OH)_2$ are present in hydrated OPC, the nitrous and nitric acids formed by photocatalytic reactions when TiO_2-modified cement was used and could still react with $Ca(OH)_2$, resulting in erosion of the OPC-based mortar [136]. In addition,

the fact that NO_2^- and NO_3^- ions in both C-S-H or calcium nitrite/nitrate are susceptible to water-based wet chemical extraction partially explain the results in Chapter 6, where the NO_x-converted NO_2^- and NO_3^- in TiO_2-modified OPC-based cementitious materials can be detected and that the mass balance between NO_x uptake through photocatalytic reactions and nitrite and nitrate formation can be achieved.

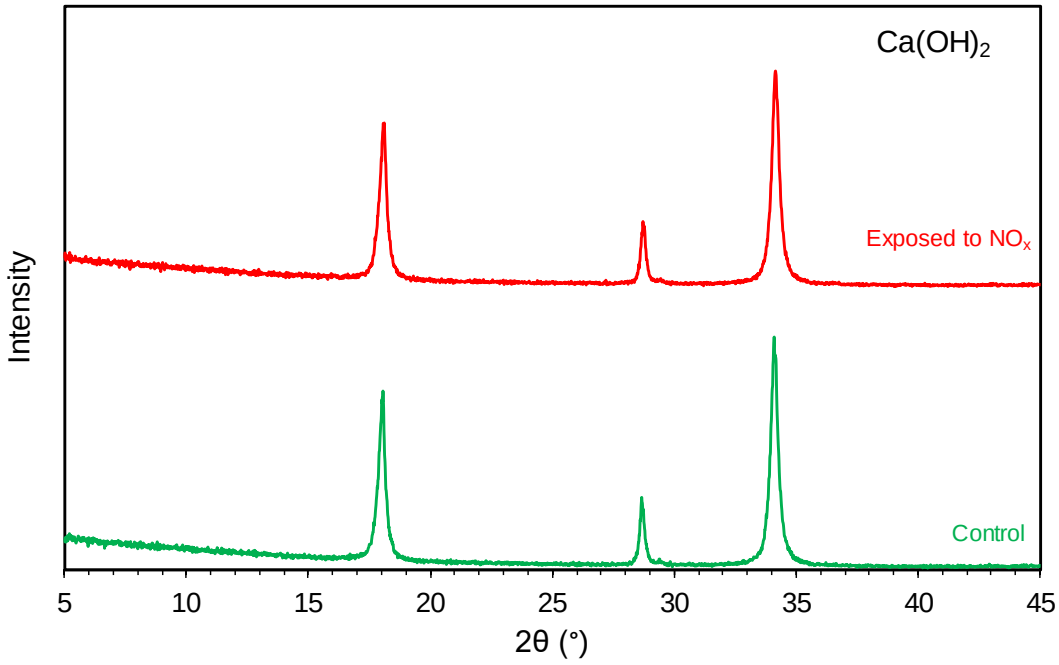

Figure 7-2: XRD patterns of synthetic $Ca(OH)_2$ before (control) and after exposed to NO_x

7.3.3 AFm-SO_4

The synthetic AFm-SO_4 shows significantly lower NO_x uptake compared to C-S-H phases (Table 7.1). This low NO_x uptake could be an indication of the formation of new cementitious phases that are not susceptible to water-based chemical extraction. The XRD

pattern for AFm-SO_4, as shown in Figure 7-3, shows a formation of new peak at 2θ of 9.5° and 15.1°. According to Glasser et al. [137], these two peaks represent the formation of AFm- NO_2/NO_3. As thermodynamically demonstrated by previous researchers [127,128], NO_2^- and NO_3^- ions, along with SO_4^{2-} ion, have an occupation preference with a ranking of NO_3^->NO_2^->SO_4^{2-}. Therefore, the converted NO_2^- and NO_3^- in this study should have substituted the interlayer SO_4^{2-} in the AFm-SO_4 phase and form crystalline AFm-NO_2/NO_3. The detection of nitrite suggests that some nitrite might partially adsorb on the surface of AFm-SO_4 and could still be susceptible to water-based chemical extraction.

This anion exchange process in aluminum-bearing phases have been suggested to be used as an additional pathway to enhance the inhibition of chloride-induced steel corrosion in reinforced concrete infrastructure by Sant et al [76]. To increase the content of NO_2^- and NO_3^- containing aluminum-bearing phases, they have proposed to us aluminate rich calcium aluminate cement (one of the motivations of this dissertation). Moreover, Falzone et al [44] have shown that chloride ions (Cl^-) can substitute the nitrite and nitrate ions and be fixed in AFm phases through the same anion exchange process, and in turn mitigate chloride-induced steel corrosion. The released NO_2^- and NO_3^- ions can either interact with other AFm-SO_4 phases or behave as anodic inhibitors that lead to the formation of a passivated protective film over the anodic sites of the steel interface to improve the corrosion resistance of steel-reinforced concrete. The detailed mechanism has been described in Section 2.3.3 in the Chapter 2 literature review. As a result, the AFm-NO_2/NO_3 phases in cementitious materials could improve the durability of cement-based concrete and in turn prolong the service life of reinforced concrete infrastructure.

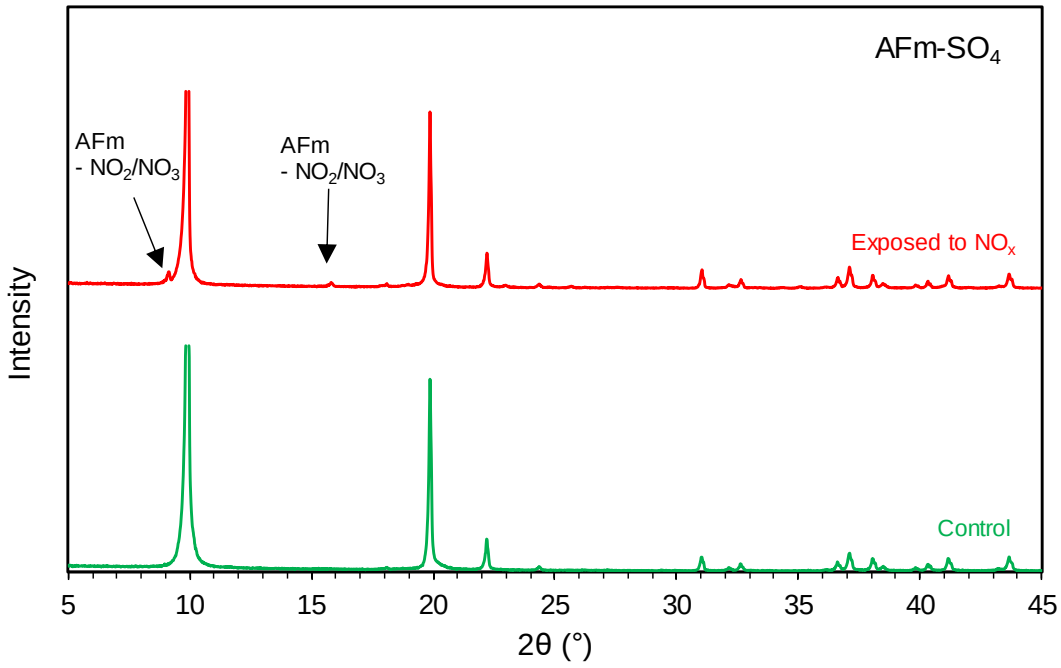

Figure 7-3: XRD patterns of synthetic AFm-SO_4 before (control) and after exposed to NO_x

7.3.4 $CaCO_3$

As discussed previously, carbonation is inevitable in cementitious materials and the main carbonation product of both C-S-H and $Ca(OH)_2$ is $CaCO_3$ [138]. Therefore, this section also examines the effects of carbonation on NO_x sequestration capability. Unlike C-S-H or $Ca(OH)_2$, the synthetic $CaCO_3$ shows much higher NO_x uptake capacity with the N mass of nitrite being approximately 14 mg/kg and nitrate being 540 mg/kg (Table 7-1). The phenomenon of NO_x uptake by calcite minerals has been previously reported by Grassian [123], where calcite was observed to convert NO_x into gas-phase HNO_3 and can further react with the $CaCO_3$ and form $Ca(NO_3)_2$.

$$CaCO_3 + HNO_3 \rightarrow Ca(NO_3)_2 + CO_2 + H_2O \qquad (7.7)$$

Grassian [123] also used Fourier-transform infrared spectroscopy (FTIR) and transmission electron microscopy (TEM) to confirm the formation of $Ca(NO_3)_2$ and found that the water adsorption ability of the reacted calcite particles was enhanced, suggesting an increased formation of water layer on the surface. As a result, the reactivity of the calcite particle could be further improved. Similarly, the gas-phase HNO_2 could also react with the $CaCO_3$ through Equation 7.8 and form $Ca(NO_2)_2$.

$$CaCO_3 + HNO_2 \rightarrow Ca(NO_2)_2 + CO_2 + H_2O \qquad (7.8)$$

However, significant less $Ca(NO_2)_2$ than $Ca(NO_3)_2$ was observed in this study and this result could be due to the high oxidization ability of $CaCO_3$ that favors the formation of $Ca(NO_3)_2$. XRD was also performed to examine the formation of $Ca(NO_2)_2$ and $Ca(NO_3)_2$. Interestingly, no new peaks could be detected by XRD (Figure 7-4). This suggests that the formed $Ca(NO_2)_2$ and $Ca(NO_3)_2$ might not be crystalized or the amounts of crystalline $Ca(NO_2)_2$ and $Ca(NO_3)_2$ were insignificant and overwhelmed by the surrounding $CaCO_3$. Nevertheless, this heterogeneous pathway of $CaCO_3$ provides a large potential chemical sink for NO_x, especially when the reactions are not only on the surface of the $CaCO_3$ particles but also occur in bulk mixtures. Therefore, $CaCO_3$ could significantly increase the intrinsic NO_x sequestration capacity of cement-based materials, especially for NO_2, even with low surface area and lack of interlayer water and pore solution-containing pores, compared to C-S-H.

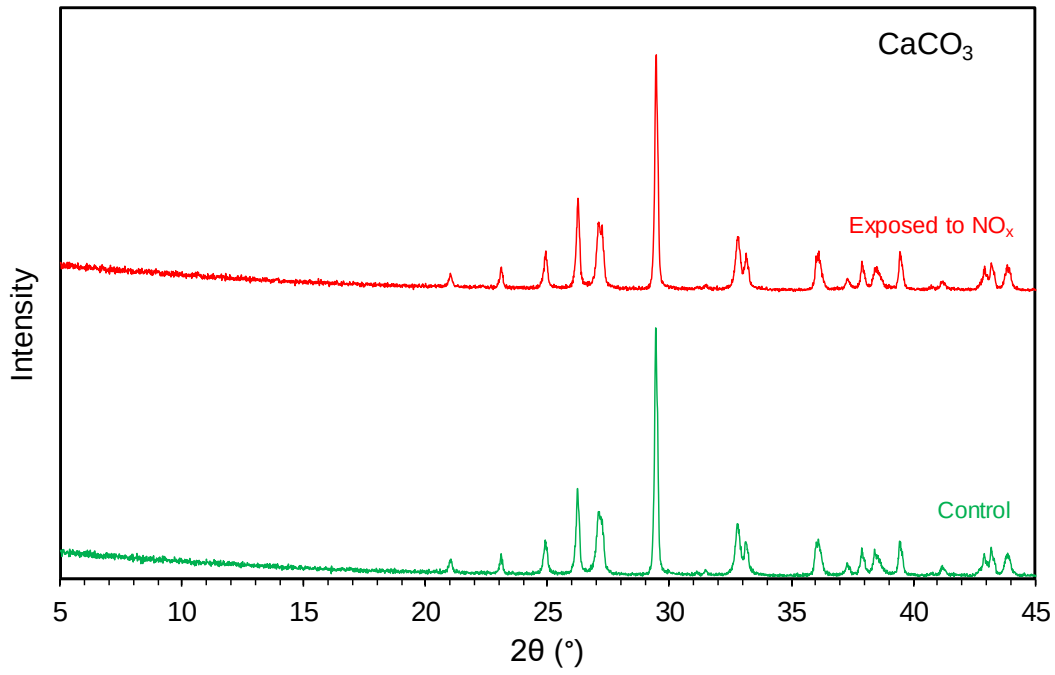

Figure 7-4: XRD patterns of synthetic $CaCO_3$ before (control) and after exposed to NO_x

7.3.5 AFm-CO_3

The effect of carbonation of AFm phases on NO_x uptake was examined using synthetic AFm-CO_3. Compared to AFm-SO_4, significantly larger amounts of NO_2^- and NO_3^- ions can be detected through water-based wet chemical extraction (Table 7-1), and no new peaks are formed in the AFm-CO_3 phase (Figure 7-5). Since both AFm phases have similar morphologies and surface features [139,140], the results from NO_2^- and NO_3^- detection and XRD suggest that the binding mechanism could also be merely physical and the anion exchange process that have been observed in AFm-SO_4 may not occur in the carbonated AFm phases. According to Balonis [127,128], NO_2^- and NO_3^-, have a greater thermodynamic occupation preference than CO_3^{2-}, with a ranking of $NO_3^->NO_2^->CO_3^{2-}$

$>SO_4^{2-}$. However, this conclusion was based on the interaction of ionic solution and solid phases [127,128]. It is hypothesized that the water molecules that are associated with this phase could be critical for such anion exchange process to occur. Nevertheless, as demonstrated in this study, without the presence of water, the difference in the thermodynamic occupation preference between NO_2^- and NO_3^- ions and CO_3^{2-} ions may not be significant, thus preventing the anion exchange. However, a future study is needed to better understand the role of water plays in the anion exchange in AFm phases. In this way, the effects of the carbonation of the AFm phase on reducing chemical substitution of NO_x can be understood and the ability of AFm phases to inhibit corrosion can be optimized.

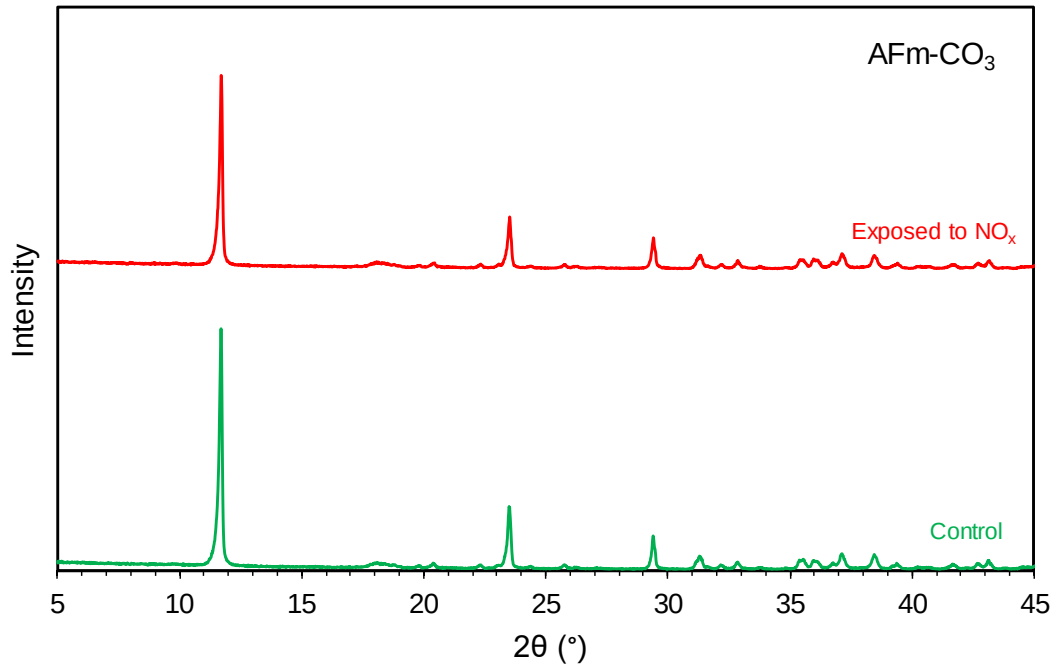

Figure 7-5: XRD patterns of synthetic AFm-CO_3 before (control) and after exposed to NO_x

7.4 Conclusion

In this chapter, five pure cementitious phases, C-S-H, $Ca(OH)_2$, AFm-SO_4, $CaCO_3$, and AFm-CO_3, were synthesized. NO_x uptake capacity for each individual phase was measured. Together with XRD analysis, the NO_x sequestration pathways can be determined and summarized in Figure 7-6.

The produced NO_2^- and NO_3^- as a result of NO_x conversion either adsorb on the surface of the C-S-H phase or dissolve in the pore solution. Either way, these ions are susceptible to water-based wet chemical extraction and can be quantified by UV-vis spectrophotometry and ion chromatography. The NO_x conversion may not occur in $Ca(OH)_2$ phases due to the low temperature and relative humidity used in this study. The converted NO_2^- and NO_3^- ions interact with the AFm-SO_4 phases by substituting for sulfate ions to form AFm-NO_2/NO_3 phases, which are potentially less susceptible to wet chemical extraction. This anion exchange process can be used to enhance chloride-induced corrosion resistance in steel-reinforced cementitious materials.

The effects of carbonation of cementitious phases are also investigated in this study. $CaCO_3$ exhibits an improved NO_x sequestration capacity compared to uncarbonated phases. This high NO_x sequestration capacity could be attributed to the reactions between the produced NO_2^- and NO_3^- and the $CaCO_3$, and can occur on the surface of the $CaCO_3$ particles, as well as in bulk mixtures. The carbonation of AFm-SO_4 phases could potentially prevent the anion exchange process and reduce the ability of AFm-SO_4 phases to inhibit corrosion.

Based on the results, water could play an important role in the NO_x sequestration capacity and pathways in cementitious phases. One of the major sources of water is from the environment's relative humidity provided in the test. Therefore, it is important to examine the effects of different relative humidifies on NO_x sequestration capacities and pathways in cementitious phases.

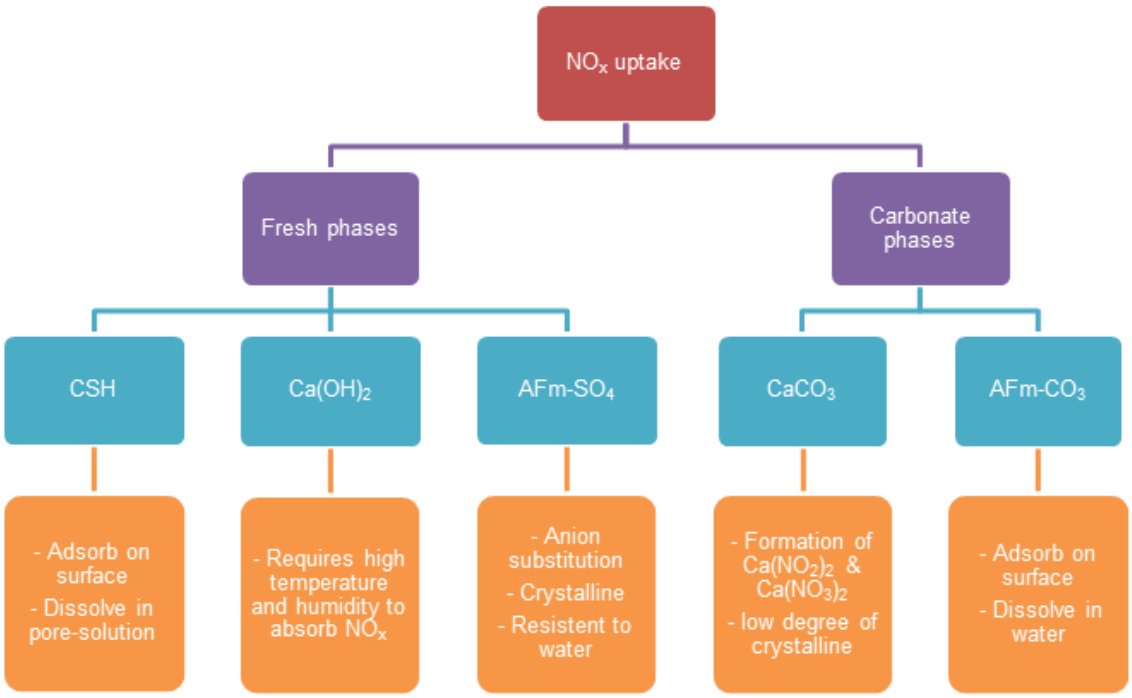

Figure 7-6: The pathways of NO_x sequestration in pure cementitious phases

CHAPTER 8. CONCLUSION AND FUTURE STUDIES

8.1 Conclusion and recommendations

The main objectives of this study were to determine the NO_x sequestration capacities and pathways in cementitious materials that incorporate anatase TiO_2 nanoparticles. These objectives were achieved by characterizing the effects of TiO_2 on cement hydration, evaluating photocatalytic performance of various TiO_2-modified cementitious materials, and quantifying the nitrite and nitrate (NO_x conversion products) in various cementitious materials and pure cementitious phases. In order to see how nitrite and nitrate interact with different cementitious materials, ordinary portland cement (OPC), the most commonly used cement, and calcium aluminate cement (CAC), an aluminum-rich cement, were used to prepare TiO_2-modified cementitious materials. The results found can further optimize the air purification, corrosion inhibition, and self-cleaning properties of nano TiO_2-engineered cementitious materials. Key conclusions and recommendations resulting from this dissertation are summarized below.

8.1.1 Cement hydration

The inclusion of TiO_2 nanoparticles accelerates the early age hydration of TiO_2-modified OPC pastes due to nucleation and growth effects induced by the addition of TiO_2. In contrast, the inclusion of TiO_2 nanoparticles retards the early age hydration of TiO_2-modified CAC pastes, which could be due to the presence of sulfate ions induced by the anatase TiO_2 nanoparticles and limited amounts of water available for CAC hydration due

to the TiO_2 addition. The retardation effects overwhelm the nucleation and growth effects induced by the TiO_2 additions, resulting in a net deceleration of CAC hydration.

TGA and XRD analyses show both 5% and 10% by weight TiO_2-modified OPC pastes produce similar hydration products as the unmodified OPC (without TiO_2) after 28 days of curing, indicating that the accelerated early age hydration does not affect the ultimate hydrated cementitious phase composition or proportionality. The 5% TiO_2-modified CAC pastes show similar XRD patterns and TGA results as unmodified CAC samples, although the 10% TiO_2-modified CAC pastes show distinctive XRD patterns and TGA results, where more stable hydrated phases of AH_3 and C_3AH_6 formed. Such phenomenon could be related the excessive amount of sulfate ions introduced by the 10% anatase TiO_2 addition, but further study is needed to determine the underlying mechanism.

Additionally, previous studies have shown that adding TiO_2 nanoparticles amounting to more than 5% does not significantly increase the photocatalytic efficiency [39,52,102], but substantially increases the material's embodied energy [63]. Therefore, only 5% addition of TiO_2 by cement mass is used in this research for examining the photocatalytic performance.

8.1.2 Photocatalytic performance

The long-term NO_x photodegradation efficiency of TiO_2-doped cementitious materials decreases with exposure time, and CAC samples exhibit a higher deceleration rate than OPC samples. OPC samples also exhibit higher NO_x photodegradation

efficiencies and capacities than CAC samples. These differences should be due to the different chemical composition and microstructural properties between OPC and CAC cements. The SEM/EDS analyses show that the TiO_2 nanoparticles are uniformly distributed within the cementitious hydrates without preference to binding with any particular hydrated phases, ensuring a well-distributed and consistent photocatalytic performance of the TiO_2-doped cementitious materials.

Similar long-term NO_x photodegradation performances were observed in TiO_2-coated cementitious materials, where OPC samples show higher efficiencies than CAC samples. MB photodegradation performance was also examined in TiO_2-coated cementitious materials, and OPC samples also show higher efficiencies than CAC samples. Again, the high efficiency is attributed to the finer and more uniform porosity in OPC-based cementitious materials, as well as the higher presence of calcium silicate hydrates that contain large surface areas. Therefore, OPC is recommended to be used as the base cement in order to enhance the photocatalytic performance of TiO_2-coated cementitious materials.

8.1.3 TiO_2-modified coating

The TiO_2-modified coatings have insignificant effects on the microstructural features of OPC samples but are shown to have significant effects on CAC samples, particularly on the pores with a size from 200-300 nm in diameter. By adding different types of SiO_2 layers (hydrophobic versus hydrophilic) in addition to the TiO_2 layers, the interaction between coated surfaces with water can be altered. The addition of a

commercial hydrophobic SiO_2 layer improves the bonding between the TiO_2-modified coating and the cementitious substrates but compromises the photocatalytic efficiency.

For selecting and designing coatings, it is important to consider the bond strength between the coating and the cementitious substrate, the desired interactions between the coated surface and water (i.e. hydrophilicity and hydrophobicity), and the photocatalytic performance. For example, if the coating is used to repair a pavement surface subject to abrasion, a strong bond and hydrophobicity of the coating properties are preferable. Therefore, it is recommended to use both TiO_2 coating with commercial hydrophobic SiO_2 to achieve the bonding performance and required hydrophobicity, while maintenance certain photocatalytic efficiency. If the coating is used to remove NO_x and clean a surface, then a higher photocatalytic performance is more desirable. In this case, the SiO_2 layer should be excluded to maximize the TiO_2-coated material's photocatalytic efficiency.

8.1.4 NO_x uptake

NO_x uptake in these cement pastes is a two-step process: (1) the conversion of NO_x to nitrite (NO_2^-) and nitrate (NO_3^-), and (2) the binding of NO_2^- and NO_3^- within the cementitious phases. By quantifying the relative abundance of nitrite and nitrate in different cementitious materials, the NO_x conversion mechanism (Step 1) can be determined and summarized in three aspects: (i) photocatalytic reactions, (ii) surface-related catalyzed heterogeneous reactions, and (iii) the alkaline environment in cementitious materials. The NO_x uptake is influenced by the photocatalytic reactions more than the surface-related catalyzed heterogeneous reactions. The NO_x uptake is also correlated with microstructural

features, including specific surface area and pore size distribution, which in turn can be used as indicators for designing cementitious materials for optimized NO_x uptake.

NO_x uptake, in terms of nitrite and nitrate detected in the material, have been quantified in both plain OPC and CAC samples regardless of the presence of UV light, demonstrating the intrinsic capability of cement-based materials to sequester NO_x even in the absence of photocatalysts. For both OPC and CAC samples, higher concentrations of nitrate were observed than nitrite. The NO_x sequestration capability of plain cementitious materials can be used to remediate atmospheric NO_x with existing cement-based infrastructure, such as using it to remediate NO_x emissions resulting from its own production and construction.

For TiO_2-doped OPC samples, a mass balance is observed between the total NO_x uptake through photocatalytic reactions and nitrite/nitrate formation, which cannot be observed in TiO_2-doped CAC samples. The results indicate the produced nitrite and nitrate ions in CAC systems could bind differently than in OPC systems, such as through anion substitution, which could potentially be less susceptible to water-based chemical extraction; hence, these ions cannot be detected by either UV-visible spectrophotometry or ion chromatography.

8.1.5 Single pure cementitious phases

The NO_2^- and NO_3^- produced by NO_x conversion either adsorb on the surface of C-S-H phases or dissolve in the pore solution. NO_x conversion may not occur in $Ca(OH)_2$

phases due to the low temperature and relative humidity used in this study. The carbonation of C-S-H and $Ca(OH)_2$ results in the formation of $CaCO_3$, which is found to be able to enhance NO_x sequestration capacity compared to uncarbonated phases. This high NO_x sequestration capacity of $CaCO_3$ could be attributed to the reactions between the produced NO_2^-/NO_3^- and $CaCO_3$ is not limited to the surface of the $CaCO_3$ particles but can also react with the bulk mixtures. Based on the results, it is recommended to increase the content of calcium carbonate in the cementitious materials to improve the NO_x uptake capacity. However, the carbonation of cementitious material could compromise the material's durability and shorten its service life. Therefore, a detailed life cycle assessment of carbonated cementitious material should be carried out to evaluate its environmental performance on NO_x sequestration.

The converted NO_2^- and NO_3^- ions interact with the AFm-SO_4 phases by substituting for sulfate ions to form AFm-NO_2/NO_3 phases, which are potentially less susceptible to wet chemical extraction. This anion exchange process of AFm-SO_4 phases can be used to enhance chloride-induced corrosion resistance in steel-reinforced cementitious materials, as proposed by Sant, et al. [76]. However, the result of AFm-CO_3 shows that the carbonation of AFm phases could potentially affect the anion exchange process that was described in AFm-SO_4 phases, and in turn might reduce the ability of AFm-SO_4 phases to inhibit corrosion. However, the underlying mechanism requires future studies. Nevertheless, the effect of carbonation on AFm phase-based corrosion inhibition should be taken into consideration for field applications.

8.2 Future studies

The present work has contributed to better understanding of NO_x sequestration capacities and pathways in nano-TiO_2 engineered cementitious materials. Based on these findings, multiple future studies are proposed in this chapter so that the materials can be optimized for the desired functionality.

8.2.1 Visible light activated photocatalysts

This dissertation only examines the photocatalytic performance of UV light-activated photocatalytic cements, which could limit the use of such materials in other infrastructure applications, such as the interior of a building without UV light. Therefore, to expand the application of photocatalytic cementitious materials, the study of using treated TiO_2 that can be activated under visible light should be carried out [141].

8.2.2 Microstructural properties

Chapter 6 has demonstrated a certain correlation between the cementitious materials' microstructural properties and its photocatalytic performance. To establish and quantify such correlation, a more controlled experiment should be carried out by using crushed samples with a narrower size range and measuring the corresponding specific surface area, pore size distribution, and photocatalytic performance.

This study has shown that the inclusion of TiO_2 nanoparticles may not affect the composition and proportionality of the cementitious phases after 28 days of curing. However, the inclusion of TiO_2 nanoparticles could affect the microstructural properties of individual cementitious phases such as C-S-H. Therefore, an examination of the TiO_2 addition on microstructure properties of individual cementitious phases should be carried out in future studies.

8.2.3 NO_x sequestration in other cementitious phases and materials

Chapter 7 investigated three major hydrated cementitious phases in OPC cement and their corresponding carbonated phases. However, different hydrated cementitious phases have been identified in other cements. To obtain comprehensive information regarding the NO_x sequestration capacity and pathways in different cementitious materials, other pure cementitious phases should be synthesized and examined. For example, various aluminate phases could be formed during CAC hydration, as shown in Chapter 3, and these phases could also be synthesized and tested under NO_x exposure. Carbonated phases, such as magnesium carbonate, can also be examined since magnesium-bearing cement has gained significant attention as a potential alternative to OPC [133,142,143].

Chapter 7 has also demonstrated that calcium carbonate ($CaCO_3$) could potentially increase the NO_x uptake capacity of cementitious materials. Limestone is intrinsically rich in $CaCO_3$ and has been widely used in cementitious materials [106,144]. Therefore, it is worthy to examine the performance of NO_x sequestration in limestone-based cementitious materials in the future study. Limestone-calcined clay cement (LC^3) has a low carbon

footprint, low cost, and high availability and could be an ideal supplementary cementitious material for NO_x uptake and mitigation [145,146].

8.2.4 N migration pathways in cementitious materials

Chapter 6 has quantified the intrinsic NO_x uptake capability of cementitious materials. One of the major applications of such capability is to use NO_x-converted nitrite and nitrate as corrosion inhibitors in concrete cover to enhance the resistance of steel corrosion. For such corrosion inhibition to be effective, the nitrite and nitrate are preferably near the embedded steel reinforcement. Chapter 7 has already shown the binding pathways of nitrite and nitrate in different cementitious phases. In future studies, it is critical to investigate the nitrite and nitrate migration pathways once they are bound with cementitious materials.

8.2.5 Relative humidity and NO_x concentration level

The results from Chapter 7 indicate water plays an important role in NO_x sequestration capacities and pathways in different cementitious phases. In concrete infrastructure, a major source of water is the relative humidity natural in the environment. Therefore, it is important to examine the effects of relative humidity on NO_x sequestration of cementitious phases, especially in portlandite and carbonated AFm phases.

It is expected that NO_x sequestration is more significant in a high-NO_x environment [40,52]; therefore, standards [46,47] recommend to use a high concentration level in NO_x exposure tests. In this dissertation, a NO_x concentration level of 1000 ppb was used based on the recommendation of standardized tests. However, the NO_x concentration level in common scenarios is significantly lower [96]. Therefore, it is desirable to examine NO_x sequestration performance under different NO_x concentration levels.

8.2.6 Measurement of NO_x uptake in TiO_2-modified CAC

According to the results in Chapter 6, the experimental approach of water-based wet chemical extraction may not be able to measure the nitrite and nitrate in CAC samples, as a result, unable to quantify the NO_x uptake capacity. Based on the previous studies [127,128], the chloride ions could substitute the nitrite and nitrate in aluminate-rich cementitious materials. Therefore, an experimental approach that uses potassium chloride-based wet chemical extraction could be used in the future study to quantify nitrite and nitrate ions in CAC samples.

8.2.7 Hydration of CAC in the presence of sulfate

As shown in Chapter 3, the anatase TiO_2 nanoparticles could introduce sulfate ions into the cementitious system since sulfates are used on the surface of TiO_2 nanoparticles to facilitate dispersion during mixing, and the hydration of CAC could be affected by these sulfate ions. Therefore, to optimize the use of TiO_2 nanoparticles, a detailed investigation

of CAC hydration in the presence of sulfate ions should be carried out. As mentioned in Chapter 3, various dosages of sulfate ions and the different ages of hydration should be examined.

8.2.8 Field demonstration and life cycle assessment

Chapter 4 and 5 have demonstrated the feasibility of using TiO_2-modified cementitious materials for air-purification. To test the results in larger scale applications, these materials could be transferred to the field, such as low-level parking decks, tunnels, and concrete pavement. To quantitively demonstrate the benefit of using these materials, such as remediating atmospheric NO_x through the existing cement-based infrastructure, a detailed life cycle analysis should be carried out. Also, when completing this life cycle assessment, the effect of the naturally decelerating rate of NO_x photodegradation efficiency should be taken into account.

Reference

[1] World Urbanization Prospects: The 2018 Revision, https://population.un.org/wup/Publications/Files/WUP2018-KeyFacts.pdf.

[2] Mapped: The World's Fastest Growing Cities. http://www.visualcapitalist.com/mapped-the-worlds-fastest-growing-cities/.

[3] U.S. and world cement production 2017 | Statistic. https://www.statista.com/statistics/219343/cement-production-worldwide/.

[4] The concrete conundrum. www.chemistryworld.org (accessed September 20, 2018).

[5] D.D. Parrish, W.R. Stockwell, Urbanization and Air Pollution: Then and Now, Eos (Washington. DC). (2015). doi:10.1029/2015EO021803.

[6] NOx How nitrogen oxides affect the way we live and breathe, Office of Air Quality Planning and Standards Research Triangle Park, NC 27711, 1998.

[7] D. Elsom, Atmospheric Pollution, Basil Blackwell, New York, 1987.

[8] J.H. Seinfeld, S.N. Pandis, Atmospheric Chemistry and Physics: From Air Pollution to Climate Change, 2006.

[9] J.H. Seinfeld, S.N. Pandis, Atmospheric Chemistry and Physics: From Air Pollution to Climate Change, Wiley, New York, 2006.

[10] G.E. Likens, F.H. Bormann, N.M. Johnson, Acid Rain, Environ. Sci. Policy Sustain. Dev. 14 (1972) 33–40. doi:10.1080/00139157.1972.9933001.

[11] G.E. Likens, F.H. Bormann, Acid rain: a serious regional environmental problem., Science. 184 (1974) 1176–9. doi:10.1126/science.184.4142.1176.

[12] D. W. SCHINDLER, Effects of Acid Rain on Freshwater Ecosystems, Science (1988) 149–157. doi:10.1126/science.208.4447.1027.

[13] US EPA, The Problem. https://www.epa.gov/nutrientpollution/problem.

[14] C. Johnson, J. Henshaw, G. Mclnnes, Impact of aircraft and surface emissions of nitrogen oxides on tropospheric ozone and global warming, Nature. 355 (1992) 69–71. doi:10.1038/355069a0.

[15] T.L. Root, J.T. Price, K.R. Hall, S.H. Schneider, C. Rosenzweig, J.A. Pounds, Fingerprints of global warming on wild animals and plants, Nature. 421 (2003) 57–60. doi:10.1038/nature01333.

[16] Nitrogen Dioxide | American Lung Association. http://www.lung.org/our-initiatives/healthy-air/outdoor/air-pollution/nitrogen-dioxide.html.

[17] World Health Organization Regional Office for Europe, 2006. www.euro.who.int.

[18] K. Miyazaki, H.J. Eskes, K. Sudo, Atmospheric Chemistry and Physics Global NOx emission estimates derived from an assimilation of OMI tropospheric NO2 columns, Atmos. Chem. Phys. 12 (2012) 2263–2288. doi:10.5194/acp-12-2263-2012.

[19] B. Zhao, S.X. Wang, H. Liu, J.Y. Xu, K. Fu, Z. Klimont, J.M. Hao, K.B. He, J. Cofala, M. Amann, Atmospheric Chemistry and Physics NO x emissions in China: historical trends and future perspectives, Atmos. Chem. Phys. 13 (2013) 9869–9897. doi:10.5194/acp-13-9869-2013.

[20] Nitrogen oxides (NOx) emissions — European Environment Agency. https://www.eea.europa.eu/data-and-maps/indicators/eea-32-nitrogen-oxides-nox-emissions-1/assessment.2010-08-19.0140149032-3.

[21] S. Paraschiv, D.-E. Constantin, S.-L. Paraschiv, M. Voiculescu, OMI and Ground-Based In-Situ Tropospheric Nitrogen Dioxide Observations over Several Important European Cities during 2005-2014., Int. J. Environ. Res. Public Health. 14 (2017). doi:10.3390/ijerph14111415.

[22] 2014 National Emissions Inventory Report. https://gispub.epa.gov/neireport/2014/.

[23] D.Q. Tong, L. Lamsal, L. Pan, C. Ding, H. Kim, P. Lee, T. Chai, K.E. Pickering, I. Stajner, Long-term NOx trends over large cities in the United States during the great recession: Comparison of satellite retrievals, ground observations, and emission inventories, Atmos. Environ. 107 (2015) 70–84. doi:10.1016/J.ATMOSENV.2015.01.035.

[24] Environmental Protection Agency 40 CFR Parts 50 and 58 Primary National Ambient Air Quality Standards for Nitrogen Dioxide; Final Rule, 2010. http://www.regulations.gov (accessed September 22, 2018).

[25] The US, TOPICAL REPORT NUMBER 14 A report on three projects conducted under separate cooperative agreements between: Reburning Technologies for the Control of Nitrogen Oxides Emissions from Coal-Fired Boilers Cover image: Schematic of reburning technology Reburning Technologies for the Control of Nitrogen Oxides Emissions from Coal-Fired Boilers, 1999. https://www.netl.doe.gov/File/Library/Research/Coal/major demonstrations/cctdp/Round2/topical14.pdf.

[26] EERE: Alternative Fuels Data Center Home Page. https://www.afdc.energy.gov/.

[27] Renewable Energy Sources - Energy Explained, Your Guide To Understanding Energy - Energy Information Administration. https://www.eia.gov/energyexplained/?page=renewable_home.

[28] A. Folli, C. Pade, T.B. Hansen, T. De Marco, D.E. MacPhee, TiO2 photocatalysis in cementitious systems: Insights into self-cleaning and depollution chemistry, Cem. Concr. Res. 42 (2012) cement. doi:10.1016/j.cemconres.2011.12.001.

[29] A. Fujishima, K. Honda, Electrochemical photolysis of water at a semiconductor

electrode., Nature. 238 (1972) cement. doi:10.1038/238037a0.

[30] M.M. Ballari, H.J.H. Brouwers, Full scale demonstration of air-purifying pavement, J. Hazard. Mater. 254–255 (2013) cement. doi:10.1016/j.jhazmat.2013.02.012.

[31] R. Sugrañez, J.I. Álvarez, M. Cruz-yusta, I. Mármol, J. Morales, J. Vila, L. Sánchez, Enhanced photocatalytic degradation of NO x gases by regulating the microstructure of mortar cement modi fi ed with titanium dioxide, Build. Environ. 69 (2013) cement. doi:10.1016/j.buildenv.2013.07.014.

[32] G. Hüsken, M. Hunger, H.J.H. Brouwers, Experimental study of photocatalytic concrete products for air purification, Build. Environ. 44 (2009) cement. doi:10.1016/j.buildenv.2009.04.010.

[33] M. Guo, C. Poon, Photocatalytic NO removal of concrete surface layers intermixed with, Build. Environ. 70 (2013) cement. doi:10.1016/j.buildenv.2013.08.017.

[34] A. Folli, S.B. Campbell, J.A. Anderson, D.E. MacPhee, Role of TiO2 surface hydration on NO oxidation photo-activity, J. Photochem. Photobiol. A Chem. 220 (2011) cement. doi:10.1016/j.jphotochem.2011.03.017.

[35] P. Alina, A. Janina, L. Bogdan, Application of titanium dioxide in cement and concrete technology, 687 (2016) cement. doi:10.4028/www.scientific.net/KEM.687.243.

[36] A.M. Ramirez, K. Demeestere, N. De Belie, T. Mantyla, E. Levanen, Titanium dioxide coated cementitious materials for air purifying purposes : Preparation, characterization and toluene removal potential, Build. Environ. 45 (2010) cement. doi:10.1016/j.buildenv.2009.09.003.

[37] J. Chen, C. Poon, Photocatalytic Cementitious Materials: Influence of the Microstructure of Cement Paste on Photocatalytic Pollution Degradation, Environ. Sci. Technol. 43 (2009) 8948–8952. doi:10.1021/es902359s.

[38] A. Yousefi, A. Allahverdi, P. Hejazi, Effective dispersion of nano-TiO2 powder for enhancement of photocatalytic properties in cement mixes, Constr. Build. Mater. 41 (2013) cement. doi:10.1016/j.conbuildmat.2012.11.057.

[39] M. Pérez-nicolás, J. Balbuena, M. Cruz-yusta, L. Sánchez, I. Navarro-blasco, J.M. Fernández, J.I. Alvarez, Cement and Concrete Research Photocatalytic NOx abatement by calcium aluminate cements modi fi ed with TiO 2 : Improved NO2 conversion, 70 (2015) cement. doi:10.1016/j.cemconres.2015.01.011.

[40] B.Y. Lee, effect of titanium dioxide nanoparticles on early age and long term properties of cementitious materials, 2012.

[41] B.Y. Lee, A.R. Jayapalan, M.H. Bergin, K.E. Kurtis, Photocatalytic cement exposed to nitrogen oxides: Effect of oxidation and binding, Cem. Concr. Res. 60 (2014) cement. doi:10.1016/j.cemconres.2014.03.003.

[42] F.P. Glasser, M. Mędala, M. Balonis, Influence of calcium nitrate and nitrite on the constitution of AFm and AFt cement hydrates, Adv. Cem. Res. 23 (2011) cement. doi:10.1680/adcr.10.00002.

[43] Corrosion inhibiting cementitious compositions, (2013). https://patents.google.com/patent/US9598314B2/en.

[44] G. Falzone, M. Balonis, D. Bentz, S. Jones, G. Sant, Anion capture and exchange by functional coatings: New routes to mitigate steel corrosion in concrete infrastructure, Cem. Concr. Res. 101 (2017) cement. doi:10.1016/j.cemconres.2017.08.021.

[45] H. Justnes, Corrosion inhibitors for reinforced concrete, Corros. Reinf. Concr. Struct. (2005) cement. doi:10.1533/9781845690434.190.

[46] ISO 22197-1:2007 - Fine ceramics (advanced ceramics, advanced technical ceramics) -- Test method for air-purification performance of semiconducting photocatalytic materials -- Part 1: Removal of nitric oxide. https://www.iso.org/standard/40761.html.

[47] JIS R 1701-1, "Fine Ceramics (Advanced Ceramics, Advanced Tech- nical Ceramics)—Test Method for Air Purification Performance of Photo- catalytic Materials—Part 1: Removal of Nitric Oxide," Japanese Standards Association, Tokyo, Japan, 2004, 24 pp.

[48] M.J. Gázquez, J.P. Bolívar, R. Garcia-Tenorio, F. Vaca, A Review of the Production Cycle of Titanium Dioxide Pigment, Mater. Sci. Appl. 05 (2014) 441–458. doi:10.4236/msa.2014.57048.

[49] Invited Review Paper TiO 2 Photocatalysis: A Historical Overview and Future Prospects. https://www.jsap.or.jp/jsapi/Pdf/Number14/04_JJAP-IRP.pdf.

[50] F. Kato, S., Mashio, Autooxidation by TiO2 as a photocatalyst., Annu. Meet Chem. Soc. Japan. 223 (1956).

[51] R. Wang, K. Hashimoto, A. Fujishima, M. Chikuni, E. Kojima, A. Kitamura, M. Shimohigoshi, T. Watanabe, Light-induced amphiphilic surfaces, Nature. 388 (1997) 431–432. doi:10.1038/41233.

[52] J. Chen, C. sun Poon, Photocatalytic construction and building materials: From fundamentals to applications, Build. Environ. 44 (2009) cement. doi:10.1016/j.buildenv.2009.01.002.

[53] S. Wang, V.C. Li, Engineered cementitious composites with high-volume fly ash, ACI Mater. J. 104 (2007) 233–241.

[54] D.J. Giannantonio, J.C. Kurth, K.E. Kurtis, P.A. Sobecky, Effects of concrete properties and nutrients on fungal colonization and fouling, Int. Biodeterior. Biodegradation. 63 (2008) 252–259. doi:10.1016/j.ibiod.2008.10.002.

[55] A. Maury Ramirez, N. De Belie, Evaluation of the algaecide activity of titanium dioxide on autoclaved aerated concrete, [STI, Science & Technology Integration], 2009. https://biblio.ugent.be/publication/878143.

[56] L. Cassar, Photocatalysis of Cementitious Materials: Clean Buildings and Clean Air, MRS Bull. 29 (2004) 328–331. doi:10.1557/mrs2004.99.

[57] J. Chen, C.S. Poon, Photocatalytic activity of titanium dioxide modified concrete materials - Influence of utilizing recycled glass cullets as aggregates, J. Environ. Manage. 90 (2009) cement. doi:10.1016/j.jenvman.2009.05.029.

[58] A. Fujishima, X. Zhang, D.A. Tryk, TiO2 photocatalysis and related surface phenomena, Surf. Sci. Rep. 63 (2008) 515–582. doi:10.1016/J.SURFREP.2008.10.001.

[59] O. CARP, Photoinduced reactivity of titanium dioxide, Prog. Solid State Chem. 32 (2004) 33–177. doi:10.1016/j.progsolidstchem.2004.08.001.

[60] T. Luttrell, S. Halpegamage, J. Tao, A. Kramer, E. Sutter, M. Batzill, Why is anatase a better photocatalyst than rutile? - Model studies on epitaxial TiO2 films, Sci. Rep. 4 (2015) 4043. doi:10.1038/srep04043.

[61] J. Chen, C.S. Poon, Photocatalytic cementitious materials: Influence of the microstructure of cement paste on photocatalytic pollution degradation, Environ. Sci. Technol. 43 (2009) cement. doi:10.1021/es902359s.

[62] A.R. Jayapalan, B.Y. Lee, S.M. Fredrich, K.E. Kurtis, Influence of Additions of Anatase TiO 2 Nanoparticles on Early-Age Properties of Cement-Based Materials, 2 (n.d.) 41–46. doi:10.3141/2141-08.

[63] A.R. Jayapalan, B.Y. Lee, K.E. Kurtis, Can nanotechnology be “green”? Comparing efficacy of nano and microparticles in cementitious materials, Cem. Concr. Compos. 36 (2013) cement. doi:10.1016/j.cemconcomp.2012.11.002.

[64] Y. Hendrix, A. Lazaro, Q. Yu, J. Brouwers, Titania-Silica Composites: A Review on the Photocatalytic Activity and Synthesis Methods, World J. Nano Sci. Eng. 05 (2015) cement. doi:10.4236/wjnse.2015.54018.

[65] M. Montes, F.P. Getton, M.S.W. Vong, P.A. Sermon, Titania on Silica. A Comparison of Sol-Gel Routes and Traditional Methods, J. Sol-Gel Sci. Technol. 8 (1997) 131–137. doi:10.1023/A:1026440213534.

[66] C. Huang, H. Bai, Y. Huang, S. Liu, S. Yen, Y. Tseng, Synthesis of Neutral / Hydrosol and Its Application as Antireflective Self-Cleaning Thin Film, Int. J. Photoenergy. 2012 (2012) 1–8. doi:10.1155/2012/620764.

[67] S. Banerjee, D.D. Dionysiou, S.C. Pillai, Self-cleaning applications of TiO2 by photo-induced hydrophilicity and photocatalysis, Appl. Catal. B Environ. 176–177 (2015) 396–428. doi:10.1016/j.apcatb.2015.03.058.

[68] P. K. Mehta, Building Durable Structures in the 21st Century, Concr. Int. 23 (2001) 57–63. http://citeseerx.ist.psu.edu/viewdoc/download?doi=10.1.1.475.5570&rep=rep1&type=pdf.

[69] D.E. Macphee, A. Folli, Cement and Concrete Research Photocatalytic concretes — The interface between photocatalysis and cement chemistry, Cem. Concr. Res. 85 (2016) cement. doi:10.1016/j.cemconres.2016.03.007.

[70] Q.L. Yu, H.J.H. Brouwers, Applied Catalysis B : Environmental Indoor air purification using heterogeneous photocatalytic oxidation . Part I : Experimental study, 92 (2009) cement. doi:10.1016/j.apcatb.2009.09.004.

[71] J.S. Dalton, P.A. Janes, N.G. Jones, J.A. Nicholson, K.R. Hallam, G.C. Allen, Photocatalytic oxidation of NO x gases using TiO 2 : a surface spectroscopic approach, 120 (2002) 415–422.

[72] T.H. Lim, S.M. Jeong, S.D. Kim, J. Gyenis, Photocatalytic decomposition of NO by TiO2 particles, J. Photochem. Photobiol. A Chem. 134 (2000) 209–217. doi:10.1016/S1010-6030(00)00265-3.

[73] J.Y. Park, Y.N. Lee, Solubility and decomposition kinetics of nitrous acid in aqueous solution, J. Phys. Chem. 92 (1988) 6294–6302. doi:10.1021/j100333a025.

[74] L. Peruchon, E. Puzenat, A. Girard-Egrot, L. Blum, J.M. Herrmann, C. Guillard, Characterization of self-cleaning glasses using Langmuir–Blodgett technique to control thickness of stearic acid multilayers: Importance of spectral emission to define standard test, J. Photochem. Photobiol. A Chem. 197 (2008) 170–176. doi:10.1016/J.JPHOTOCHEM.2007.12.033.

[75] S. Banerjee, D.D. Dionysiou, S.C. Pillai, Applied Catalysis B : Environmental Self-cleaning applications of TiO 2 by photo-induced hydrophilicity and photocatalysis, "Applied Catal. B, Environ. 176–177 (2015) cement. doi:10.1016/j.apcatb.2015.03.058.

[76] G.S.B.-S.E. Kurtis, Corrosion inhibiting cementitious compositions, 2013. http://www.ownersperspective.org/item/75.

[77] A. Mills, J. Wang, Photobleaching of methylene blue sensitised by TiO2: an ambiguous system?, J. Photochem. Photobiol. A Chem. 127 (1999) 123–134. doi:10.1016/S1010-6030(99)00143-4.

[78] UNI11247:2007. http://store.uni.com/catalogo/index.php/catalog/product/view/id/77740/s/uni-11247-2007/category/4172/?josso_back_to=http://store.uni.com/josso-security-check.php&josso_cmd=login_optional&josso_partnerapp_host=store.uni.com.

[79] K.M. Miranda, M.G. Espey, D.A. Wink, A Rapid, Simple Spectrophotometric Method for Simultaneous Detection of Nitrate and Nitrite, Nitric Oxide. 5 (2001)

62–71. doi:10.1006/niox.2000.0319.

[80] Q.-H. Wang, L.-J. Yu, Y. Liu, L. Lin, R. Lu, J. Zhu, L. He, Z.-L. Lu, Methods for the detection and determination of nitrite and nitrate: A review, Talanta. 165 (2017) 709–720. doi:10.1016/J.TALANTA.2016.12.044.

[81] ISO/TC 206 Fine ceramics, ISO 10678:2010 Fine ceramics (advanced ceramics, advanced technical ceramics) — Determination of photocatalytic activity of surfaces in an aqueous medium by degradation of methylene blue, 2010.

[82] R.W. Matthews, Photocatalytic oxidation and adsorption of methylene blue on thin films of near-ultraviolet-illuminated TiO2, J. Chem. Soc. Faraday Trans. 1 Phys. Chem. Condens. Phases. 85 (1989) 1291–1302. doi:10.1039/F19898501291.

[83] A. Mills, An overview of the methylene blue ISO test for assessing the activities of photocatalytic films, Appl. Catal. B Environ. 128 (2012) 144–149. doi:10.1016/J.APCATB.2012.01.019.

[84] C. Mendoza, A. Valle, M. Castellote, A. Bahamonde, M. Faraldos, TiO2 and TiO2-SiO2 coated cement: Comparison of mechanic and photocatalytic properties, Appl. Catal. B Environ. 178 (2015) 155–164. doi:10.1016/j.apcatb.2014.09.079.

[85] S. Mowry, P.J. Ogren, Kinetics of Methylene Blue Reduction by Ascorbic Acid, J. Chem. Educ. 76 (1999) 970. doi:10.1021/ed076p970.

[86] A. Mills, C. O'Rourke, Adsorption and destruction of methylene blue by semiconductor photocatalysis, Green. 1 (2011) 105–113. doi:10.1515/green.2011.001.

[87] CEMENT (Data in thousand metric tons unless otherwise noted), 2013. https://minerals.usgs.gov/minerals/pubs/commodity/cement/mcs-2018-cemen.pdf.

[88] B.Y. Lee, K.E. Kurtis, Influence of TiO2 nanoparticles on early C3S hydration, J. Am. Ceram. Soc. 93 (2010) 3399–3405. doi:10.1111/j.1551-2916.2010.03868.x.

[89] B. Lothenbach, L. Pelletier-chaignat, F. Winnefeld, Cement and Concrete Research Stability in the system CaO – Al 2 O 3 – H 2 O, Cem. Concr. Res. 42 (2012) cement. doi:10.1016/j.cemconres.2012.09.002.

[90] J.H. Ideker, K.L. Scrivener, H. Fryda, B. Touzo, Calcium Aluminate Cements, in: Lea's Chem. Cem. Concr., Elsevier, 2019: pp. 537–584. doi:10.1016/B978-0-08-100773-0.00012-5.

[91] T. Matusinović, J. Šipušić, N. Vrbos, Porosity-strength relation in calcium aluminate cement pastes, Cem. Concr. Res. 33 (2003) 1801–1806. doi:10.1016/S0008-8846(03)00201-1.

[92] K.L. Scrivener, J.L. Cabiron, R. Letourneux, High-performance concretes from calcium aluminate cements, Cem. Concr. Res. 29 (1999) cement. doi:10.1016/S0008-8846(99)00103-9.

[93] T. Chotard, N. Gimet-Breart, A. Smith, D. Fargeot, J.P. Bonnet, C. Gault, Application of ultrasonic testing to describe the hydration of calcium aluminate cement at the early age, Cem. Concr. Res. 31 (2001) 405–412. doi:10.1016/S0008-8846(00)00446-4.

[94] T.J. Chotard, M.P. Boncoeur-Martel, A. Smith, J.P. Dupuy, C. Gault, Application of X-ray computed tomography to characterise the early hydration of calcium aluminate cement, Cem. Concr. Compos. 25 (2003) 145–152. doi:10.1016/S0958-9465(01)00063-4.

[95] ASTM C114 - 18 Standard Test Methods for Chemical Analysis of Hydraulic Cement, West Conshohocken, PA, 2018. https://www.astm.org/Standards/C114 (accessed June 8, 2019).

[96] A.R. Jayapalan, B.Y. Lee, E.M. Land, M.H. Bergin, K.E. Kurtis, Photocatalytic efficiency of cement-based materials: Demonstration of proposed test method, ACI Mater. J. 112 (2015) cement. doi:10.14359/51686985.

[97] Active Standard ASTM C1679 | Developed by Subcommittee: C09.48, ASTM C1679 - 17: Standard Practice for Measuring Hydration Kinetics of Hydraulic Cementitious Mixtures Using Isothermal Calorimetry, 2017.

[98] P. Hewlett, Lea" s Chemistry of Cement and Concrete, 2004. doi:10.1016/B978-0-7506-6256-7.50031-X.

[99] J. Justs, M. Wyrzykowski, F. Winnefeld, D. Bajare, P. Lura, Influence of superabsorbent polymers on hydration of cement pastes with low water-to-binder ratio: A calorimetry study, J. Therm. Anal. Calorim. 115 (2014) 425–432. doi:10.1007/s10973-013-3359-x.

[100] H.F.W. Taylor, Cement chemistry, 2nd ed., ICE Publishing, 1997.

[101] K. Scrivener, R. Snellings, B. Lothenbach, A practical guide to microstructural analysis of cementitious materials, n.d.

[102] J. Chen, S. cong Kou, C. sun Poon, Photocatalytic cement-based materials: Comparison of nitrogen oxides and toluene removal potentials and evaluation of self-cleaning performance, Build. Environ. 46 (2011) cement. doi:10.1016/j.buildenv.2011.03.004.

[103] J. Chen, C.S. Poon, Photocatalytic cementitious materials: Influence of the microstructure of cement paste on photocatalytic pollution degradation, Environ. Sci. Technol. 43 (2009) 8948–8952. doi:10.1021/es902359s.

[104] C. Cárdenas, J.I. Tobón, C. García, J. Vila, Functionalized building materials : Photocatalytic abatement of NO x by cement pastes blended with TiO2 nanoparticles, 36 (2012) cement. doi:10.1016/j.conbuildmat.2012.06.017.

[105] A.J. Allen, J.J. Thomas, H.M. Jennings, Composition and density of nanoscale calcium – silicate – hydrate in cement, (2007) cement. doi:10.1038/nmat1871.

[106] J. Bizzozero, K.L. Scrivener, Limestone reaction in calcium aluminate cement-calcium sulfate systems, Cem. Concr. Res. 76 (2015) 159–169. doi:10.1016/j.cemconres.2015.05.019.

[107] Y. Hendrix, A. Lazaro, Q. Yu, J. Brouwers, Titania-Silica Composites: A Review on the Photocatalytic Activity and Synthesis Methods, World J. Nano Sci. Eng. 05 (2015) 161–177. doi:10.4236/wjnse.2015.54018.

[108] M. Anpo, H. Yamashita, Y. Ichihashi, S. Ehara, Photocatalytic reduction of CO2 with H2O on various titanium oxide catalysts, J. Electroanal. Chem. 396 (1995) 21–26. doi:10.1016/0022-0728(95)04141-A.

[109] M. Faraldos, R. Kropp, M.A. Anderson, K. Sobolev, Photocatalytic hydrophobic concrete coatings to combat air pollution, Catal. Today. 259 (2016) cement. doi:10.1016/j.cattod.2015.07.025.

[110] I. Flores-Vivian, V. Hejazi, M.I. Kozhukhova, M. Nosonovsky, K. Sobolev, Self-Assembling Particle-Siloxane Coatings for Superhydrophobic Concrete, ACS Appl. Mater. Interfaces. 5 (2013) 13284–13294. doi:10.1021/am404272v.

[111] A. Marmur, C. Della Volpe, S. Siboni, A. Amirfazli, J.W. Drelich, Contact angles and wettability: Towards common and accurate terminology, Surf. Innov. 5 (2017) 3–8. doi:10.1680/jsuin.17.00002.

[112] J.T. Simpson, S.R. Hunter, T. Aytug, Superhydrophobic materials and coatings: A review, Reports Prog. Phys. 78 (2015). doi:10.1088/0034-4885/78/8/086501.

[113] A. Mills, S. Le Hunte, An overview of semiconductor photocatalysis, J. Photochem. Photobiol. A Chem. 108 (1997) cement. doi:10.1016/S1010-6030(97)00118-4.

[114] A. Mills, J. Wang, Photobleaching of methylene blue sensitised by TiO2: an ambiguous system?, J. Photochem. Photobiol. A Chem. 127 (1999) cement. doi:10.1016/S1010-6030(99)00143-4.

[115] A. Mills, An overview of the methylene blue ISO test for assessing the activities of photocatalytic films, Appl. Catal. B Environ. 128 (2012) cement. doi:10.1016/j.apcatb.2012.01.019.

[116] B.Y. Lee, A.R. Jayapalan, M.H. Bergin, K.E. Kurtis, Photocatalytic cement exposed to nitrogen oxides: Effect of oxidation and binding, Cem. Concr. Res. 60 (2014) 30–36. doi:10.1016/j.cemconres.2014.03.003.

[117] M. Balonis, M. Mędala, F.P. Glasser, Influence of calcium nitrate and nitrite on the constitution of AFm and AFt cement hydrates, Adv. Cem. Res. 23 (2011) cement. doi:10.1680/adcr.10.00002.

[118] S. Brunauer, P.H. Emmett, E. Teller, Adsorption of Gases in Multimolecular Layers, J. Am. Chem. Soc. 60 (1938) 309–319. doi:10.1021/ja01269a023.

[119] E.P. Barrett, L.G. Joyner, P.P. Halenda, The Determination of Pore Volume and

Area Distributions in Porous Substances. I. Computations from Nitrogen Isotherms, J. Am. Chem. Soc. 73 (1951) 373–380. doi:10.1021/ja01145a126.

[120] I. Odler, The BET-specific surface area of hydrated Portland cement and related materials, Cem. Concr. Res. 33 (2003) 2049–2056. doi:10.1016/S0008-8846(03)00225-4.

[121] M.C. Garci Juenger, H.M. Jennings, The use of nitrogen adsorption to assess the microstructure of cement paste, Cem. Concr. Res. 31 (2001) 883–892. doi:10.1016/S0008-8846(01)00493-8.

[122] M.M. Hassan, H. Dylla, L.N. Mohammad, T. Rupnow, Evaluation of the durability of titanium dioxide photocatalyst coating for concrete pavement, Constr. Build. Mater. 24 (2010) 1456–1461. doi:10.1016/j.conbuildmat.2010.01.009.

[123] V.H. Grassian*, Chemical Reactions of Nitrogen Oxides on the Surface of Oxide, Carbonate, Soot, and Mineral Dust Particles: Implications for the Chemical Balance of the Troposphere, (2002). doi:10.1021/JP012139H.

[124] A. Febo, C. Perrino, Prediction and experimental evidence for high air concentration of nitrous acid in indoor environments, Atmos. Environ. Part A, Gen. Top. 25 (1991) 1055–1061. doi:10.1016/0960-1686(91)90147-Y.

[125] M.E. Jenkin, R.A. Cox, D.J. Williams, Laboratory studies of the kinetics of formation of nitrous acid from the thermal reaction of nitrogen dioxide and water vapour, Atmos. Environ. 22 (1988) 487–498. doi:10.1016/0004-6981(88)90194-1.

[126] M. Horgnies, I. Dubois-Brugger, E.M. Gartner, NOx de-pollution by hardened concrete and the influence of activated charcoal additions, Cem. Concr. Res. 42 (2012) 1348–1355. doi:10.1016/J.CEMCONRES.2012.06.007.

[127] G. Falzone, M. Balonis, G. Sant, X-AFm stabilization as a mechanism of bypassing conversion phenomena in calcium aluminate cements, Cem. Concr. Res. 72 (2015) cement. doi:10.1016/j.cemconres.2015.02.022.

[128] G. Puerta-Falla, M. Balonis, G. Falzone, M. Bauchy, N. Neithalath, G. Sant, Monovalent ion exchange kinetics of hydrated calcium-alumino layered double hydroxides, Ind. Eng. Chem. Res. 56 (2017) cement. doi:10.1021/acs.iecr.6b03474.

[129] M. Balonis, F.P. Glasser, Calcium nitrite corrosion inhibitor in portland cement: Influence of nitrite on chloride binding and mineralogy, J. Am. Ceram. Soc. 94 (2011) cement. doi:10.1111/j.1551-2916.2010.04362.x.

[130] E. L'Hôpital, B. Lothenbach, G. Le Saout, D. Kulik, K. Scrivener, Incorporation of aluminium in calcium-silicate-hydrates, Cem. Concr. Res. 75 (2015) 91–103. doi:10.1016/j.cemconres.2015.04.007.

[131] H. Viallis-Terrisse, A. Nonat, J.C. Petit, Zeta-potential study of calcium silicate hydrates interacting with alkaline cations, J. Colloid Interface Sci. 244 (2001) 58–65. doi:10.1006/jcis.2001.7897.

[132] T. Matschei, B. Lothenbach, F.P. Glasser, The AFm phase in Portland cement, Cem. Concr. Res. 37 (2007) cement. doi:10.1016/j.cemconres.2006.10.010.

[133] P. Hewlett, Lea's Chemistry of Cement and Concrete., Elsevier, 2004.

[134] X. Zhang, H. Tong, H. Zhang, C. Chen, Nitrogen oxides absorption on calcium hydroxide at low temperature, Ind. Eng. Chem. Res. 47 (2008) 3827–3833. doi:10.1021/ie070660d.

[135] G. Chen, J. Gao, J. Gao, Q. Du, X. Fu, Y. Yin, Y. Qin, Simultaneous removal of SO2 and NOx by calcium hydroxide at low temperature: Effect of SO2 absorption on NO 2 removal, Ind. Eng. Chem. Res. 49 (2010) 12140–12147. doi:10.1021/ie101594x.

[136] T. Ibusuki, Cleaning atmospheric environment (photocatalytic activities of TiO2), in: M. Kaneko, I. Okura (Eds.), Photocatal. Sci. Technol. Springer, Berlin Heidelberg, 2010: p. 143.

[137] F.P. Glasser, M. Mędala, M. Balonis, Influence of calcium nitrate and nitrite on the constitution of AFm and AFt cement hydrates, Adv. Cem. Res. 23 (2011). doi:10.1680/adcr.10.00002.

[138] A. Morandeau, M. Thiéry, P. Dangla, Investigation of the carbonation mechanism of CH and C-S-H in terms of kinetics, microstructure changes and moisture properties, Cem. Concr. Res. 56 (2014) 153–170. doi:10.1016/j.cemconres.2013.11.015.

[139] T. Matschei, B. Lothenbach, F.P. Glasser, The AFm phase in Portland cement, Cem. Concr. Res. 37 (2007) 118–130. doi:10.1016/j.cemconres.2006.10.010.

[140] M.U. Okoronkwo, F.P. Glasser, Compatibility of hydrogarnet, Ca3Al2(SiO4)x(OH)4(3 -X),with sulfate and carbonate-bearing cement phases: 5-85 °c, Cem. Concr. Res. 83 (2016) 86–96. doi:10.1016/j.cemconres.2016.01.013.

[141] S. Sato, Photocatalytic activity of NOx-doped TiO2 in the visible light region, Chem. Phys. Lett. 123 (1986) 126–128. doi:10.1016/0009-2614(86)87026-9.

[142] C. Unluer, A. Al-Tabbaa, Impact of hydrated magnesium carbonate additives on the carbonation of reactive MgO cements, Cem. Concr. Res. 54 (2013) 87–97. doi:10.1016/j.cemconres.2013.08.009.

[143] L. Mo, D.K. Panesar, Effects of accelerated carbonation on the microstructure of Portland cement pastes containing reactive MgO, Cem. Concr. Res. 42 (2012) 769–777. doi:10.1016/j.cemconres.2012.02.017.

[144] T. Matschei, B. Lothenbach, F.P. Glasser, The role of calcium carbonate in cement hydration, Cem. Concr. Res. 37 (2007) 551–558. doi:10.1016/j.cemconres.2006.10.013.

[145] K. Scrivener, F. Martirena, S. Bishnoi, S. Maity, Calcined clay limestone cements

(LC3), Cem. Concr. Res. 114 (2018) 49–56. doi:10.1016/j.cemconres.2017.08.017.

[146] Y. Cancio Díaz, S. Sánchez Berriel, U. Heierli, A.R. Favier, I.R. Sánchez Machado, K.L. Scrivener, J.F. Martirena Hernández, G. Habert, Limestone calcined clay cement as a low-carbon solution to meet expanding cement demand in emerging economies, Dev. Eng. 2 (2017) 82–91. doi:10.1016/j.deveng.2017.06.001.